Observing Star Formation in local Active Galactic Nuclei from Swift-BAT survey

MURRAY, SIMON,ANDREW

Observing Star Formation in local Active Galactic Nuclei from *Swift*-BAT survey

Simon A. Murray

Abstract

A hallmark of the co-evolution between a super-massive black hole (SMBH) and its host galaxy is the connection between the growth of a SMBH (AGN activity) and of the galaxy (star formation). I investigate this connection by measuring the mean star formation rates (SFRs) of a sample of 313 galaxies of AGN selected from the *Swift*-BAT ultra-hard (14 – 195 keV) X-ray survey of the local Universe. This is achieved by separating the contribution of the AGN and star formation from the spectral energy distributions (SEDs) of the *Swift*-BAT AGN using infrared photometry from *Herschel* and WISE. I present the mean star formation rates (SFRs) as a function of bolometric AGN luminosity (L_{BOL}) which show a rise towards higher luminosities ($L_{BOL} \geq 10^{44}$ erg s^{-1}). I set out a range of methods (e.g. stellar mass offsets from star-forming galaxy relations) to show that the rise in SFR is most likely a consequence of the high fraction of the higher luminosity subset being starbursts (i.e. an intense period of star formation in a galaxy) and of mass effects (i.e. more massive galaxies hosting more luminous AGN). In support of this main project, I investigate the value of modern *Herschel* photometry compared to legacy IRAS photometry in the estimation of SFRs. In addition I propose a new colour diagnostic for identifying AGN using *Herschel* photometry and assess how reliable our SED fitting procedure is by constraining the AGN template to subarcsecond resolution mid-infrared photometry.

Observing Star Formation in local Active Galactic Nuclei from *Swift*-BAT survey

Simon A. Murray

A thesis presented in accordance with the regulations for admittance to the degree of Master of Science by Research

Centre for Extragalactic Astronomy
Department of Physics
University of Durham
United Kingdom
January 2017

Dedicated to

My Mum, my partner Natalie and our daughter Imogen.

Declaration

The work described in this thesis was undertaken between October 2015 and September 2016 while the author was a research student under the supervision of David M. Alexander and Christopher M. Harrison in the Department of Physics at the University of Durham. No part of this thesis has been submitted for any other degree at the University of Durham or any other University.

Portions of this work have appeared in the following paper:

- *Chapter 1*: F, Stanley, C. M. Harrison, D. M. Alexander, A. M. Swinbank, J. A. Aird, A. Del Moro, R. C. Hickox, J. R. Mullaney, 2015, MNRAS, 453, 591: "**A remarkably flat relationship between star formation rate and AGN luminosity for distant X-ray AGN**"

The work described in Chapters 2 and 3 was performed in collaboration with D.M. Alexander, C. M. Harrison, D. J. Rosario, and F. Stanley. Chapter 2 is based on the procedure led by F. Stanley as presented in the above publication. The spectral energy distribution fits of Chapter 2 and Appendix A were performed by F. Stanley, and C.M. Harrison. All of the text has been written by the author.

Acknowledgements

I would like to thank my supervisors Dave Alexander and Chris Harrison for all their continuous support which have helped improve my research skills over the past year. I have been incredibly lucky to have been given this chance and it has been a tremendous pleasure to be a part of the Extragalactic Astronomy group at Durham. Thanks also go to Flora Stanley and David Rosario who have helped me in this project and let it progress into something incredible.

A very important part of this year was making friends from a range of different academic backgrounds that have helped me develop both as a friend and a researcher. Special thanks go to Weiqu, Orinze, Dominic, Natalie, Stephan, Peter, Vegard, Sophie, Rosa, Kayleigh, and my office companions for making this year an enjoyable one.

Also, my best friends Kevin, Laura and Natalie, who have been there for me since my University days at Aberdeen, have really helped me get to the position I am in now. I am still grateful to have them by my side for their continuous support which has been priceless this year and really helped me get through this work. My gratitude must go to my Mum who has always been supportive, academically and personally! Finally, to my newly born child, Imogen, who has given me that extra determination to complete this work over the year, to which this thesis is dedicated to.

Contents

List of Tables

List of Figures

CHAPTER 1

Introduction to Active Galactic Nuclei

1.1 Overview

Active Galactic Nuclei (AGN) are defined as energetic phenomena producing large amounts of luminosity of non-stellar origin across the entire electromagnetic spectrum (Peterson 1997). Residing in the centre of galaxies, there is sufficient evidence to suggest that all massive ($M_{Bulge} \geq 10^9\ M_\odot$) galaxies have hosted AGN activity at some point during their lifetimes (Kormendy & Ho 2013). AGN activity is produced by the central supermassive black hole (SMBH) "feeding" off the supply of in-falling gas from an accretion disk. Similarly, the rate of growth for a galaxy is determined by measuring the star formation, i.e. the process of collapsing gas from a cold gas supply to form new stars. Theoretical works on the coevolution of the central SMBH and its host galaxy have suggested that there may be a connection between the AGN activity and star formation, i.e. the growth of black hole and of the galaxy. Investigating the effect an AGN has on the star formation of a galaxy is important in understanding how galaxies evolve over time.

This study will investigate the relationship between the AGN luminosity and the star formation rates of local AGN. The adopted method in this study uses infrared photometry to constrain the contribution of AGN and star formation activity to the respective infrared spectral energy distributions (SEDs) of local X-ray selected AGN. The aims of this first chapter are to: (1) provide a brief introduction and history on the field of AGN research; (2) give a summary of the unified and physical model of AGN; (3) give a brief overview of the AGN multi-wavelength emission and how each emission region (relevant to this thesis) can be used to identify AGN and establish

some of the research and results on the connection between AGN activity and star formation.

1.2 Introduction to Active Galactic Nuclei

In 1909, the first AGN to be studied was NGC 1068 (Fath 1909) which showed strong emission lines in its optical spectra (Hubble 1925) suggesting that large clouds of gas and dust were moving at hundreds of kms^{-1} from the galaxies core.[1] In 1943, Carl Seyfert observed the nuclear spectra of 12 different galaxies with half of them having similar observable properties to NGC 1068 such as bright stellar-like nuclei producing strong emission lines. On the basis of these similarities these galaxies were classified as "Seyfert galaxies", and two types of classifications were defined. Seyfert 1 galaxies were observed to have strong broad optical - ultraviolet (UV) emission line widths (typically of 2000 – 10000 km s^{-1}) whereas Seyfert 2 galaxies have much narrower emission line widths (typically 200 km s^{-1}). As the 20^{th} century progressed and further research into galaxies was made the classifications of Seyfert galaxies expanded as astronomers observed different properties and wavelengths (e.g. Seyfert 1.5, 1.8, 1.9; see Osterbrook 1981).

Towards the 1960s, radio astronomers were making observations of bright radio sources, as a result of decent angular resolution, that appeared to look like stars optically. Defined as Quasi-Stellar Radio Sources (hereafter Quasars) these objects are now known to be very distant AGN, observed at a time when the Universe was considerably younger than today. The first Quasar discovered was the radio source 3C 273 ($z = 0.158$) which is over four trillion times brighter than the Sun and outshines its own galaxy (Schmidt 1963). Quasars are amongst some of the most luminous objects in the Universe. Seyfert galaxies and Quasars are both examples of AGN, a central SMBH with an accreting disk of gas which reaches extremely high temperatures of order $\approx 10^5$ K. AGN can produce a colossal amount of energy (up to $\approx 10^{47}$ erg s^{-1} for extremely massive AGN; see Brandt & Alexander 2015) across a broad spectrum of radio waves to X-rays. There are many other classifications of AGN, defined on the

[1] Although first observed in 1909, the phenomena of AGN activity from NGC 1068 was not recognised until several decades later.

basis of their observed characteristics. However, these sub-classifications are typically unified within the physical AGN model (see Section 1.3).

The key aspect all AGN have in common is a massive, compact and powerful energy source. In order to create such a large amount of energy (typically $\approx 10^{42} - 10^{47}$ erg s^{-1}) it became generally accepted that all AGN host a growing SMBH from mass accretion (e.g. Salpeter 1964; Lynden-Bell 1969). At that time only a few hundred of these powerful beasts were known to exist in the Universe, today millions of them have been identified across the Universe. It is now believed that SMBHs reside in all massive galaxies and that most galaxies will have gone through some AGN activity at some time in their lifetimes (see Kormendy & Ho 2013).

1.3 AGN structure and classifications

1.3.1 The unified and physical models of AGN

Following the brief introduction on Seyfert galaxies and Quasars in the previous section, it is useful to know what classifies as an AGN. This thesis will not go into detail about the classifications of AGN nor the differences between each classification; instead I will briefly describe the unified model for AGN, which connects the physical structure of the AGN to the observed properties.

Typical classifications of AGN are based on three characteristics: luminosity, radio loudness and spectral type. For example, radio loudness is split into two subclasses: radio loud and radio quiet. Both radio quiet and loud AGN are otherwise thought to have the same physical component and central engine. The main difference between radio quiet and loud AGN appear to be in the host galaxies and whether or not a powerful radio jet can be produced: radio loud – associated with elliptical galaxies that have undergone mergers and can produce a radio jet; radio quiet – associated with spiral hosts and do not produce a radio jet (Wilson & Colbert 1994). On average radio loud AGN are typically $10^{3\text{-}4}$ times brighter in the radio band than the ten times more common (see Kellerman et al. 1989) radio-quiet AGN (Elvis et al. 1994; Wilson & Colbert 1994).

Of course each AGN may vary in some details, but the typical standard AGN model (see Figure 1) will consist of a central SMBH surrounded by an accretion disk of predominantly hot ionised gases (e.g. Shakura & Sunyaev 1973; see Section 1.3.2). The unified model proposes that all types of AGN are surrounded by a geometrically and optically thick dusty torus region (e.g. Antonucci 1993; see Section 1.3.2) and that the different observable properties of AGN are caused by the angle dependent obscuration of the nucleus (Li 2007).The torus can obscure regions of AGN that produce broad emission lines. This consequently gives root to two different definitions of Seyfert galaxies, namely Seyfert 1 galaxies where broad and narrow emission lines can be detected and Seyfert 2 galaxies where only narrow emission lines can be detected. But it is observed in the unified model of AGN that Seyfert 1 galaxies and Seyfert 2 galaxies are the same class of objects with a difference due to orientation effects (Bianchi et al. 2012).

Additionally, the AGN standard model includes an accretion disk corona, a broad-line region, a narrow-line region and radio jets included in the model, but since they are not explored in this thesis, I shall only note some brief key facts below: (1) the hot corona above and below the accretion disk that produce hard X-ray emissions; (2) the broad-line region that is under the gravitational influence of the black hole; (3) the narrow-line region which is more extended over 10^2 – 10^4 parsec scales; (4) the large-scale radio jet which can reach incredible relativistic speeds (and can have a profound impact on the growth of galaxies; see Section 1.5). However, it is worth noting that while this standard AGN model is widely accepted among the scientific community, some studies suggest that modifications of this model are required (e.g. a clumpy torus structure; see Netzer 2015).

1.3.2 Black Holes, Accretion Disks, and Tori.

Black holes are the densest objects in the Universe.[2] Thought to be more of a

[2] Just a century ago, Albert Einstein proposed his theory of general relativity which was soon used by Karl Schwarzschild to provide a solution for an uncharged spherically symmetric non-rotating system with a point mass. This solution, known as the Schwarzschild metric (see review from Heinicke & Hehl 2015), had caused a wide spread debate about whether or not these “singularities” (a point at which a highly dense object with mass, where the escape velocity is equal to or greater than the speed of light, becomes infinitely dense) could ever exist in nature.

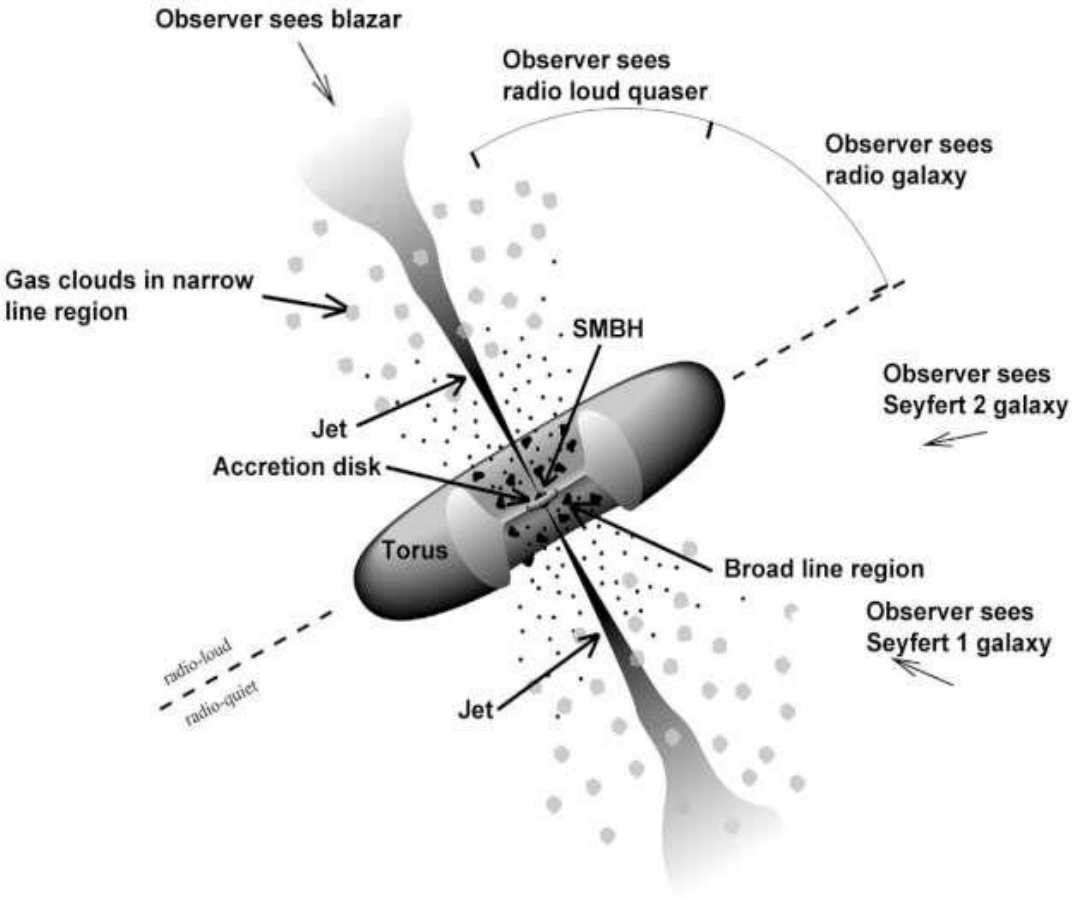

Figure 1.1: A schematic diagram of the unified model of the structure of AGN (adapted from Urry & Padovani 1995). A large compact central black hole surrounded by an accretion disk of tidally disturbed material inside a geometrically and optically thick dusty "Torus" structure. There lies a hot corona above and below the accretion disk which produces the hard X-ray emission. There also exists a broad-line region (BLR) that is under the gravitational influence of the black hole and the narrow-line region (NLR) that is spread over much larger distances. The large-scale radio jets (that can end up being orders of magnitudes larger than the entire galaxy) are launched in the vicinity of the accretion disk. The observed emission and properties from the AGN is dependent on the inclination angle of the torus with respect to the observer. For example, the accretion disk can be hidden behind the torus, while a direct view of the radio jet with respect to the observer will classify this AGN as a Blazar. Image credit: NASA.

mathematical error, Albert Einstein did not believe that infinitely dense "singularities" (now known as black holes) could exist in nature (see Einstein 1939). However, some of the first evidence indicating that black holes do in fact exist is Cygnus X-1. Located in the Milky Way, Cygnus X-1 is an X-ray binary system comprised of a 14.8 $M_{\odot}$ black hole (mass measurement from Orosz et al. 2011) and a 19.2 $M_{\odot}$ supergiant star. At the time of discovery, astronomers detected X-ray emissions coming from this, unknown at the time, black hole as it was thought the supergiant star was being manipulated by its compact and "unseen" companion's unmatched gravitational forces. Later models suggested that a stellar mass black hole was consuming the gases protruded by the supergiant star which resulted in high energy X-rays being emitted from the compact object. Since then, and as a result of hard scientific research, black holes are now widely accepted in the scientific community but remain a challenge to conclusively identify since an object that produces no light is challenging to directly detect. However, astronomers can still measure the effect SMBHs have on other objects. For example, a mass measurement of the SMBH Sagittarius A* residing at the center of the Milky Way is possible since astronomers can observe the trajectory of large stars under the gravitational influence of the SMBH. Astronomers measure this large beast to be around 3.6 – 4.3 x 10^6 $M_{\odot}$ (Ghez et al. 2008; Gillessen et al. 2009; Schödel et al. 2009)

There are three main classifications of black holes based on their mass. These are stellar mass black holes, primordial black holes and super-massive black holes. The consequence of a supernovae collapse can create a stellar mass (3-30 $M_{\odot}$) black hole (e.g. Cygnus X-1 has a black hole mass of 14.8 $M_{\odot}$; see Orosz et al. 2011 for a review), while in the early universe primordial black holes ($\approx 10^{-8}$ kg – 10^5 $M_{\odot}$; see Volonteri 2010 for a review) were thought to have been created by the extreme densities of gas formed at the beginning of the universe.. Even though astronomers search for signs of primordial black holes, there is currently no empirical evidence of their existence although it is possible that these primordial black holes would have grown into the SMBHs (10^6 – 10^9 $M_{\odot}$) seen in the center of massive galaxies today via AGN activity. SMBHs were proposed soon after the discovery of Quasars due to the enormous energy released in these systems (Lynden-Bell 1969). The most well adopted model for the SMBH accretion was first developed by Shakura and Sunyaev

(1973) where it was apparent that the most likely candidate for these energy outputs was accretion onto a SMBH since nothing else came close to replicating these remarkable luminosities. The luminosity from this accretion event is given as the following:

$$L_{acc} = \eta \dot{M} c^2 \tag{1.3.1}$$

where η is the efficiency of the mass-energy conversion (typically ≈ 0.1) and $\dot{M} = dM/dt$ is the mass accretion rate. Equation 1.3.1 gives a useful indication on how much mass is being accreted onto a SMBH. As such a limit on the maximum mass accretion rate can be calculated when it is assumed that the spherical accretion flow of ionised hydrogen gas onto a black holes central mass M_{BH} and when the radiative force of the accretion luminosity is equal to the gravitational force. This upper limit is called the "Eddington" luminosity and is of the form:

$$L_{Edd} = \frac{4\pi G M_{BH} m_p c}{\sigma_t} \tag{1.3.2}$$

$$L_{Edd} = 1.3\ x\ 10^{38}\ \frac{M}{M_{\odot}}\ (\text{erg s}^{-1}) \tag{1.3.3}$$

where G is the gravitational constant, m_p is the proton mass, c is the speed of light and σ_t is the Thompson cross-section for an electron.

This consequently means that for $M_{BH} = 10^6$ -10^9 $M_{\odot}$ the resulting Eddington luminosities range in-between $\approx 10^{44}$ -10^{47} erg s^{-1}. If a black hole is accreting at this Eddington rate then this would mean that these astonishing luminosities from accretion can outshine the host galaxy by more than a thousand times. A good review into the mechanics and structure of the accretion disk can be found by King (2008). It is useful to know that there is a range of AGN accretion emission spanning across the mid-infrared to soft X-ray emissions but peaking in the UV (see Figure 1.2) due to the heating of material via friction. This becomes important later on when talking about re-

emitted infrared emission as a consequence of the UV being absorbed by the dusty region encasing the inner region of the AGN known as the Torus (see Section 1.5).

The torus in the unified model of AGN is described as a geometrically and optically thick dusty region. The surrounding dust encasing the nucleus is an important feature of AGN, since it can cause a large diversity in the observed properties of AGN depending on the viewing angle of the obscuration. The unified model of AGN proposes that type 1 and type 2 Seyfert galaxies are similar AGN observed at different viewing angles. This orientation effect means that the broad and narrow emission lines can be detected in Seyfert 1 galaxies, whereas only the narrow emission line can be detected in Seyfert 2 galaxies. In many cases the torus shrouds the observers view to the central accreting SMBH. Similarly Blazars are actually Quasars, except the difference between the two is that the observer has a direct line of sight to the emitting radio jet, which is the reason why Blazars appear to be much more luminous.

An interesting aspect to the torus is the range of multi-wavelength emissions observed. The emission from the dusty torus is predominantly at infrared wavelengths. The accretion disk of heavily ionised gas releases photons peaking at the UV which interact with the dust in the torus. The dust will be heated up by absorbing the photons and consequently will re-emit thermal radiation at infrared wavelengths typically peaking in the mid-infrared (Polletta et al. 2000) and dropping off at longer wavelengths (Mullaney et al. 2011)[3]. The absorption of UV photons will make the accretion disk weak or absent for obscured lines of sight to the observer. Though the use of hard X-rays (almost all of the x-rays will be emitted from the corona) gives a clear view through the torus to the central source, but in the case of infrared and optical studies the dust obscuration must first be accounted for. It should be noted that the detection of soft X-rays gets much more difficult with more obscured AGN, e.g. Compton-thick AGN (with intrinsic column density, $N_H > 1.5x10^{24}$ cm^{-2}) have soft X-rays which are absorbed. Many studies suggest that the torus is restricted by size to a few parsecs (e.g. Ramos Almeida et al. 2009) and distributed in clumps (e.g. Schartmann et al. 2008) indicating that the unified model of AGN may need to developed further.

[3] Though the infrared emission may actually vary for different AGN, the typical peak resides in the mid-infrared $\lambda = 5 – 40$ μm or temperature at 70-600K.

1.4 Multi-wavelength emission from an AGN

Astronomers observed that AGN emit over a broad range of the electromagnetic spectrum. A schematic representation of an AGN SED is shown in Figure 1.2, below I will give a small overview of the two types of emissions most relevant to this thesis: X-ray and infrared emissions.

1.4.1 X-ray emission and observations

A rather successful way of identifying AGN is by using X-rays (Elvis et al. 1978; Zamorani et al. 1981) since X-rays are very energetic, penetrative[4] and do not suffer from dust attenuation. Furthermore, AGN are strong X-ray emitters which makes observing this waveband important. The majority of the X-ray emission produced from an AGN is due to the hot corona around the accretion disc. It is thought that the UV – optical photons being produced via the accretion disc go through Compton up-scattering to create a power law spectrum of X-rays. Unlike stellar mass black holes (e.g. in an X-ray binary such as Cygnus X-1) where most of the spectral behaviour can be observed by the accretion disk (Gilfanov & Merloni 2014), accretion disks around SMBHs weakly produce X-rays and peak more in the UV as a result of being cooler than stellar mass black hole accretion disks.. In comparison, star formation is much weaker at X-ray energies than AGN (LaMassa et al. 2012; Treister et al 2013) which allows AGN to be relatively easily identified in the X-ray band. Although able to penetrate obscuration X-rays will miss the most heavily obscured sources (Treister et al. 2004) and finding evidence of ultra-obscured SMBH still provides a significant challenge (Comastri et al. 2015)

There has been a number of successful deep X-ray surveys conducted to discover AGN measuring energies at 1 – 10 keV (Brandt & Alexander 2015). The *Swift* Burst Alert Telescope (BAT: Gehrels et al. 2004; Barthelmy et al. 2005) is an all-sky ultra-hard X-ray mission measuring energies between 14 – 195 keV. *Swift*-BAT has the capability to measure large projected gamma-ray burst outflows coming from

[4] X-rays are less sensitive to obscuration than UV, for example.

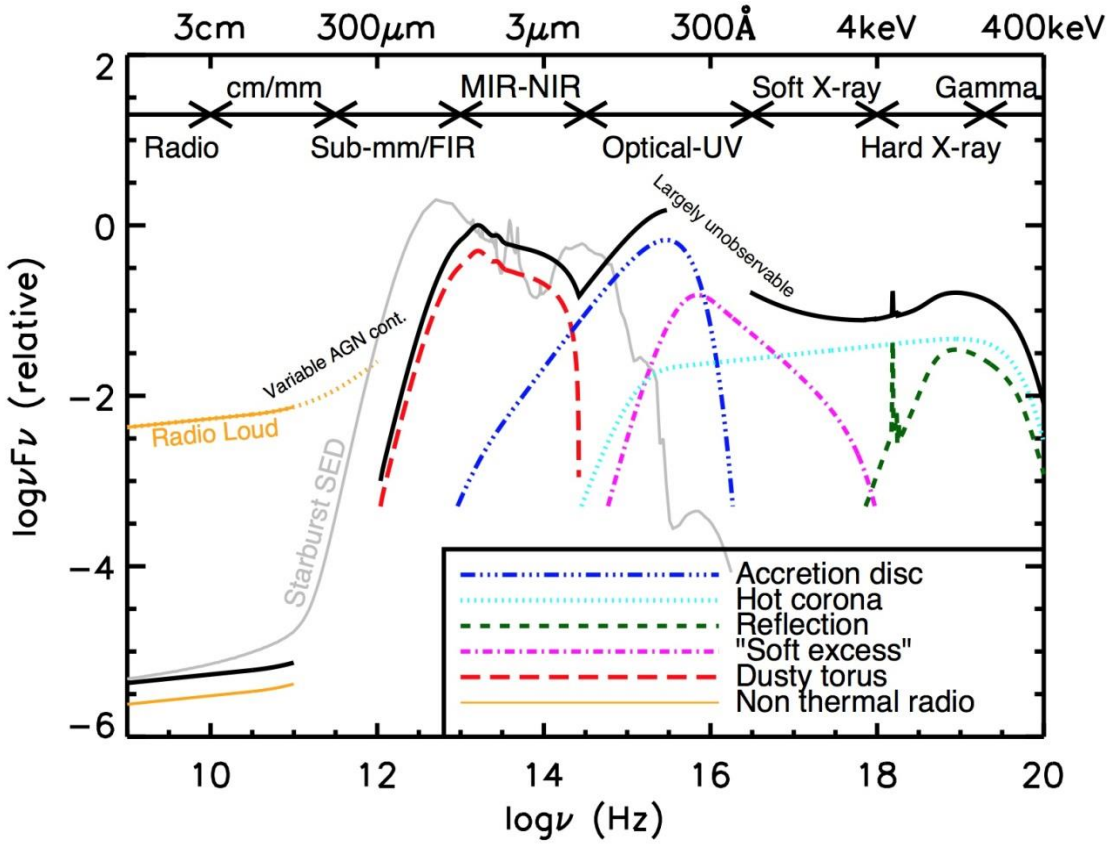

Figure 1.2: A schematic representation of an AGN SED, loosely based on the observed SEDs of radio-quiet quasars (e.g., Elvis et al. 1994; Richards et al. 2006). The black solid curve represents the total SED and the various coloured curves (with an arbitrary offset) represent the individual components. The SED of an AGN in the mm-FIR regime is uncertain; however, it is widely believed to have a minimal contribution (to an overall galaxy SED) compared to star formation, except in the most intrinsically luminous quasars and powerful radio-loud AGN. The primary emission from the AGN accretion disk peaks in the UV region. Radio-loud AGN have radio emission that can be several orders of magnitude higher than radio-quiet AGN (shown with the labelled orange line). Also shown is an example radio--UV SED of a starburst galaxy (grey curve; the SED is of M82 taken from the GRASIL library; Silva et al. 1998). Taken from Harrison (2016).

across the Universe in a very quick response with minimal reaction times compared to its predecessors.

Since X-ray do not directly probe the total accretion disk luminosity of SMBHs this will lead to higher uncertainties in derived bolometric luminosities (than by integrating all available photometric flux measurements on an average AGN SED). This was observed in Figure 5 of Winter et al. (2012) which determined a conversion equation (with a correction coefficient of $R^2 = 0.82$)[5] of the bolometric AGN luminosity (L_{BOL}) using the *Swift*-BAT luminosity (L_{BAT}) of the following form:

$$\log(L_{BOL}) = 1.1157\, x \log(L_{BAT}) - 4.2280 \qquad (1.4.4)$$

Other studies which have investigated X-rays have used this conversion and it is relevant for the work in this thesis, therefore it will be implemented throughout.

1.4.2 Infrared emission and observations

As described in Section 1.3, warm dust that is heated up by AGN will emit luminous infrared emissions. Since most AGN are "hidden" away due to the obscuring dust, the infrared waveband can give a lot of insight to the AGN since it not greatly affected by dust attenuation. This makes observations in the infrared waveband useful in identifying, especially heavily obscured, AGN. Before the operation of sensitive far-infrared observatories scientists were limited to the near-infrared and mid-infrared wave bands due to limiting sensitivity of the infrared detectors (see Low and Kleinmann 1968). Over many years the launches of observatories, listed below, have greatly progressed far-infrared astronomy.

[5] The correlation coefficient measures the linear relationship between two variables, e.g. a perfect correlation, $R^2 = 1$, suggests that the two variables have the strongest positive relationship. Winter et al. (2012) found $R^2 = 0.82$ which indicates there is a strong positive relationship between the two variables, but it is not perfect. Given that they correlate well, a connection between the bolometric luminosity and hard X-ray luminosity is found.

- The Infrared Astronomical Satellite (IRAS; Neugebauer et al. 1984) all-sky survey launched in 1983 operated at wavebands 12, 25, 60 and 100μm.
- The Infrared Space Observatory (ISO) launched in 1995 operated at wavelengths 2.5 to 200μm.
- The *Spitzer* Space Telescope launched in 2003 with the Infrared Array Camera (IRAC) operating at wavelengths 3.6 and 8.0μm.
- The Wide-field Infrared Survey Explorer (WISE; Wright et al. 2010) all-sky survey launched in 2009 observing at four bands in the near- to mid-infrared 3.4, 4.6, 12 and 22μm.
- The *Herschel* Space Observatory launched in 2009 with the Photodetector Array Camera and Spectrometer (PACS; Poglitsch et al. 2010) and Spectral and Photometric Imaging Receiver (SPIRE; Griffin et al. 2010) instruments operating at 60-210μm and 200-670μm respectively.

Unfortunately, AGN are not the only class of astrophysical sources to emit in the infrared waveband. Star formation is also often bright at infrared wavelengths due to young stars shrouded in dusty clouds. Fortunately, the infrared emission from AGN and star formation are often distinct. The dust being heated by the AGN will be hotter than the dust heated by the star formation. This will cause the AGN emission to peak more in the mid-infrared while star formation peaks in the far-infrared waveband (Domínguez Sánchez et al. 2014). Owing to the fact that even the deepest X-ray surveys can miss an AGN due to not being able to penetrate the dusty torus region, this makes the infrared a good identifier of AGN. However, it is always important to separate between the AGN and star-forming emission components in infrared SEDs (Mullaney et al. 2011, LaMassa et al. 2012, Del Moro et al. 2013, Delvecchio et al. 2014, Stanley et al. 2015).

1.5 Star formation

Galaxy evolution is predominantly driven by the process of star formation, i.e. dense cold regions of gas clouds collapsing together to form stars. A simple measurement for the rate of growth for a galaxy is the star formation rate. The availability of cold gas

used to form stars can be dependent on a number of different processes, such as AGN feedback and supernovae explosions. For example, AGN can release powerful winds, outflows and jets which can reduce star formation by causing an ejection of the cold gas supply and raising the entropy of gas (McCarthy et al. 2011), or alternatively increase star formation by compressing the interstellar medium which can raise the pressure and gas density (Ishibashi & Fabian 2012).

Star formation can be measured by using direct or indirect tracers of the emission from young stars. The direct approach relies upon measuring the UV emission from young massive stars. However, since stars often form within cold gas clouds the UV emission can be absorbed by the gas and dust surrounding them. The dust is heated by the young stars, which is re-radiated thermally, at far-infrared wavelengths. Therefore, star formation can be indirectly traced using far-infrared observations (e.g. Fritz et al. 2006; Calzetti et al. 2010; Lutz 2014). However, this indirect method only works for dusty galaxies and the measured star formation rates depend on the specific shape of the far-infrared SED (Kennicutt 1998).

As explored in Section 1.4.2, the most sensitive observatory at far-infrared wavelengths is the *Herschel* satellite. *Herschel* has been able to observe the far-infrared emission of star-forming galaxies out to high redshifts thanks to its high sensitivity. Many studies have used monochromatic luminosities as a proxy of star formation for a galaxy. For example, Shao et al. (2010) investigated the star formation of a sample of AGN (up to $z = 0.3$) using *Herschel* photometry and found that towards higher AGN luminosities a rise in star formation rate was apparent. Other studies use SED fitting of flux measurements to constrain the AGN and star formation emission in the infrared band, which provides more accurate star formation rates than taking a monochromatic luminosity that does not account for the AGN contribution. In this thesis, I use *Herschel* photometry to constrain the infrared SEDs and determine the star formation rates of the *Swift*-BAT sample of X-ray detected AGN in the local Universe.

1.6 The relationship between AGN activity and star formation

It has been found that there exists a tight correlation between the mass of the central SMBH and the galaxy bulge[6] in nearby galaxies (see Figure 1.3; Kormendy 1993; Magorrian et al. 1998; Kormendy & Ho 2013). This correlation shows that the SMBH mass is approximately three orders of magnitude lower than the galaxy bulge. The tightness of the correlation allows SMBH masses to be estimated for galaxies with stellar bulge masses to a reasonable degree of accuracy for most systems. However, we caution that some galaxies may lie off the SMBH – bulge mass relationships, such as galaxies with pseudobulges (Mathur et al. 2012; Kormendy & Ho 2013).

This correlation also implies a link between the rate of growth of galaxies (i.e. star formation) and AGN activity. Indeed, many studies have shown that luminous AGN reside in star-forming galaxies (Kauffmann et al. 2003; Alexander et al. 2005; Mullaney et al. 2012, Rosario et al. 2013a) and that the average star formation rates of moderate X-ray luminosity AGN and normal star-forming galaxies (named Main Sequence galaxies) are similar (e.g. Mullaney et al. 2012; Rosario et al. 2013a).This further strengthens the evidence for a connection between the AGN activity and the star formation, where possibly the coevolution between the two is regulated by either the AGN or the galaxy itself.

There have been a number of studies investigating, in more detail, the connection between AGN activity and the mean SFRs using far-infrared photometry (e.g. Lutz et al. 2010; Shao et al. 2010; Mullaney et al. 2012; Harrison et al. 2012; Rosario et al. 2013a; Stanley et al. 2015). The main results of these studies show that the mean SFR of AGN are similar to those found in normal star-forming galaxies of the same mass. Most studies conclude that they find no connection between the mean SFR and the bolometric AGN luminosity for moderate AGN luminosities. However, towards the higher range of AGN luminosity there is much more variation in the results in which some studies find an increasing relationship[7] (e.g. Lutz et al. 2010; Shao et al. 2010; Mullaney et al. 2010), a decreasing relationship (e.g. Page et al. 2012) or a broadly flat relationship (e.g. see Figure 1.4, Stanley et al. 2015) between mean SFR and X-ray luminosity. Stanley et al. (2015) explains the flat relationship is

[6] It is noted in a review from Kormendy & Ho (2013) that the bulge mass is defined for classical and elliptical bulges.

[7] It is noted that the increasing relationship is also found for similar studies that use X-ray derived star formation rates (e.g. Cohen 2003; LaMassa et al. 2012).

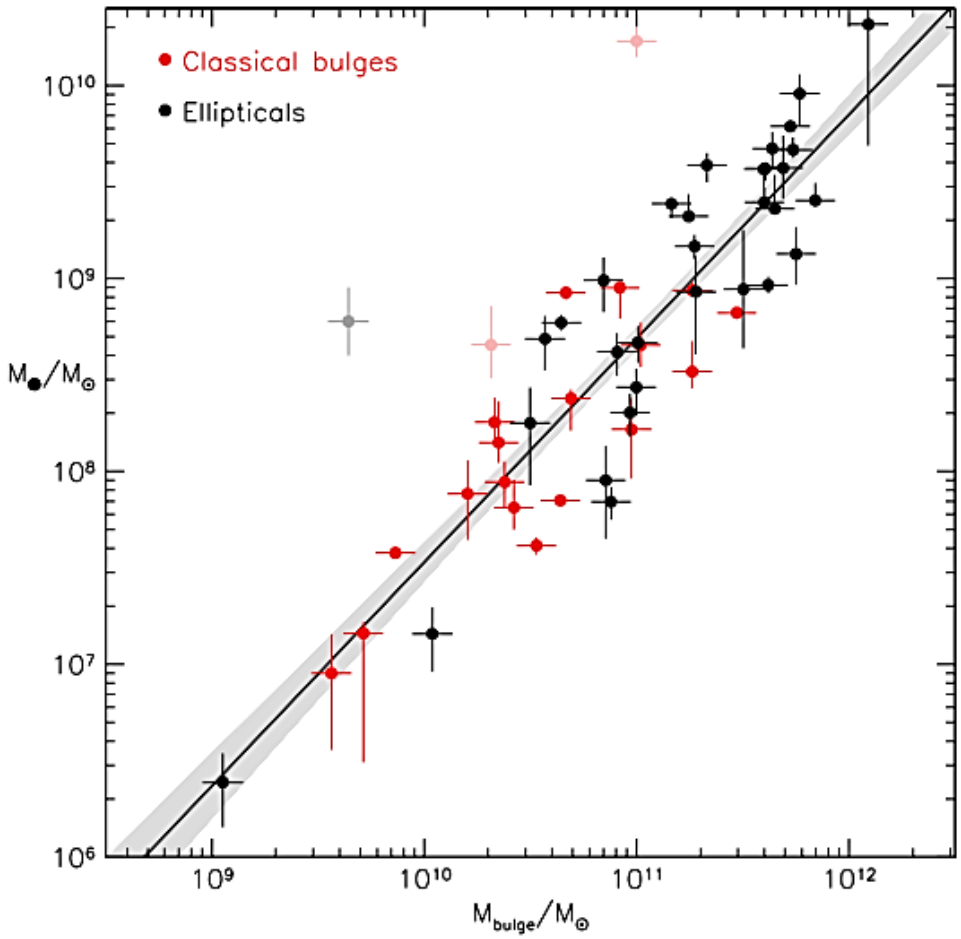

Figure 1.3: Black hole mass, M_{BH}, as a function of galaxy bulge mass, M_{bulge}, from Kormendy & Ho (2013) for a sample of classical and elliptical bulges. This correlation provides indirect evidence for the coevolution between the growing AGN and their host galaxies growth, i.e. AGN activity is related to star formation.

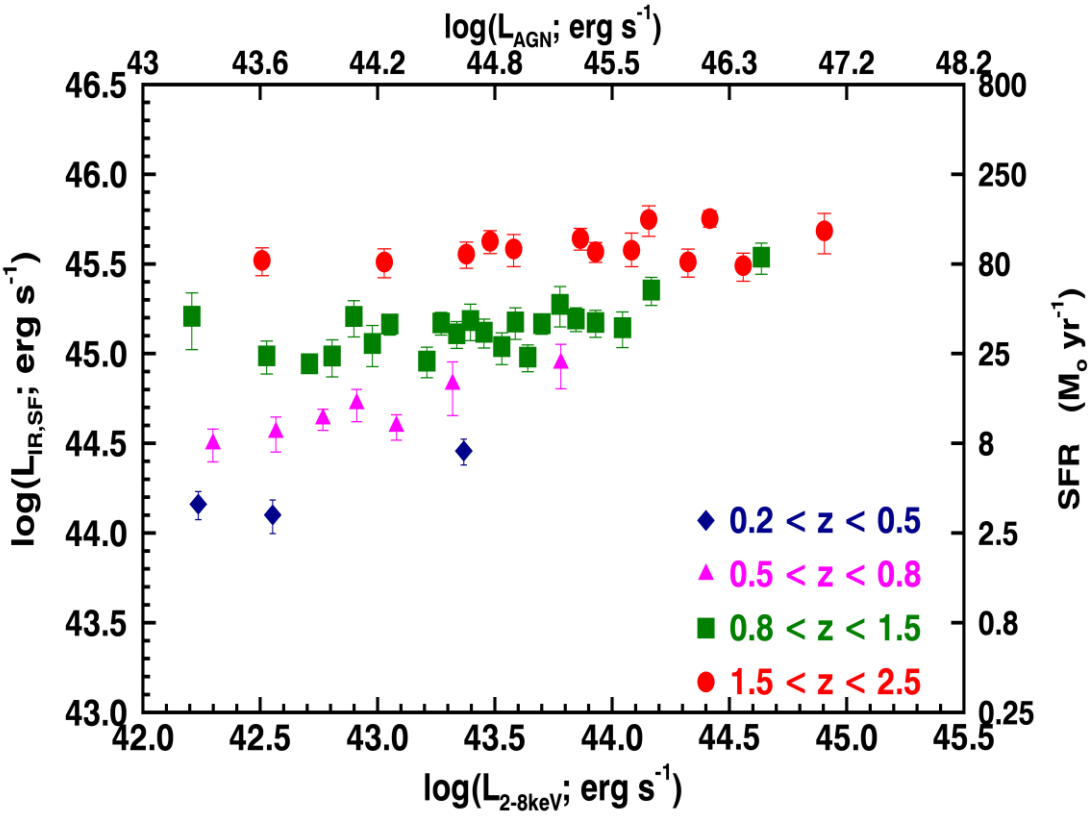

Figure 1.4: Mean IR luminosity due to star formation, $L_{IR,SF}$, as a function of X-ray luminosity, $L_{2\text{-}8\ keV}$, for four redshift ranges. Each $L_{2\text{-}8\ keV}$ bin gives the mean $L_{IR,SF}$ for ≈ 40 sources. The corresponding SFR values are converted using the Kennicutt (1998) relation corrected to a Chabrier IMF (Chabrier 2003), and the bolometric AGN luminosity L_{AGN} is calculated from $L_{2\text{-}8\ keV}$ using the luminosity dependent relation of Stern (2015). The errors on the $L_{IR,SF}$ are calculated using a bootstrap analysis. Taken from Stanley et al. (2015).

due to AGN variability on shorter timescales than the star formation. Hickox et al. (2014) showed that AGN variability could mask any correlation between the AGN luminosity and mean SFR (Stanley et al. 2015; Gabor et al. 2016). Stanley et al. (2015) provides the key foundation for the work presented in this thesis. They observe the flat relationship between AGN luminosity and mean SFRs of X-ray detected AGN over redshifts z = 0.2 – 2.5. However, they did not explore the relationship between the mean SFR and X-ray luminosity for X-ray AGN at $z \approx 0$. Therefore, using similar techniques as those adopted in Stanley et al. (2015) and in order to see what impact the AGN activity has on the star formation, this thesis will calculate the mean SFRs of X-ray AGN in the local Universe using H*erschel* far-infrared photometry to provide a $z \approx 0$ baseline to compare with Stanley et al. (2015).

1.7 Thesis Overview

The overall aim of this thesis is to find a connection between the AGN luminosity and the mean SFRs of local AGN using *Herschel* observations. This will be achieved by using multi-wavelength photometry to constrict broad-band SEDs and to then decompose these SEDs in the AGN and star forming components using a template fitting procedure. This work will extend the study of Stanley et al. (2015) to the local universe. Therefore, I use similar methods to those presented in Stanley et al. (2015), for example, the SED fitting procedure and the AGN decomposition method uses the same procedure adopted in Stanley et al. (2015). Throughout this thesis I assume H_o = 71km s^{-1}, $\Omega_\Lambda = 0.73$, $\Omega_M = 0.27$ and a Chabrier (2003) initial mass function (IMF). A short summary of the chapters included in this thesis are given below.

Chapter 2: The SED fitting procedure, analysis and results

This chapter provides the methods I use in this thesis to quantify the star formation in each source in our *Swift*-BAT AGN sample using *Herschel* photometric data. We give an overview to the multi-wavelength data acquired for this study, the SED fitting procedure and decomposition method, the calculation of the average SFRs, and provide some results on the SED fitting procedure. The results include some

analysis of how accurately our SED fitting procedure performs and some colour-colour analysis involving the use of the Mateos et al. (2012) AGN wedge.

Chapter 3: Results and discussions of the mean SFRs for local Active Galactic Nuclei

This chapter uses the individual star formation rates, provided from the previous chapter, to find the average SFR as a function of AGN bolometric luminosity. I assess what is driving the increase in mean SFR at high AGN luminosities at low redshift, compare our AGN results with those of normal star-forming galaxies (i.e. the main sequence) and finally, compare our results using *Herschel* photometric data to the data taken from the IRAS database.

Chapter 4: Conclusions and future work

This chapter provides an overall summary of the work presented in this thesis and describes the future work needed on questions yet to be answered.

Appendix:

In Appendix A I provide the SEDs and best-fitting template solutions for all 313 X-ray detected *Swift*-BAT sources from the SED fitting method described in Section 2.3.

CHAPTER 2

The SED fitting procedure, analysis and results

2.1 Motivation

In Section 1.6 it was explored how the AGN activity is connected to the star formation out to $z \approx 3$ using X-ray and infrared surveys. Most studies conclude that the mean star formation rate (SFR) of AGN at moderate luminosities ($L_{2\text{-}8\ keV} = 10^{42} - 10^{44}$ erg s^{-1}) are similar to those of normal coeval star-forming galaxies. These moderately luminous AGN tend to exhibit a flat relationship between the mean SFRs and AGN luminosity, caused by AGN variability (Hickox et al. 2014). For more luminous AGN ($L_{2\text{-}8\ keV} > 10^{44}$ erg s^{-1}) some studies find that the mean SFRs of AGN also have a flat relationship with AGN luminosity at high redshifts. However, this flat relationship is less apparent for lower redshifts and usually shows a subtle rise in mean SFRs towards higher luminosities (e.g. Stanley et al. 2015). The motivation of the work presented in this thesis is to provide a $z \approx 0$ baseline for the Stanley et al. (2015) work using a similar approach (i.e. compute the mean SFRs of local AGN at redshift $z = 0 - 0.05$ using *Swift*-BAT X-ray detections and *Herschel* far-infrared observations). For this we follow a similar method to that presented in Stanley et al. (2015) by disentangling the amount of AGN and star formation activity in the spectral energy distributions of AGN.

In this chapter we discuss the methodology used to calculate star formation rates of local AGN. In Section 2.2 I present the AGN sample along with the photometry acquired in the mid- and far-infrared bands. In Section 2.3 I describe the SED fitting procedure used to fit the photometry to determine the contributions of the AGN activity and star formation and how to convert these measurements in star formation rates. In Section 2.4, I discuss how accurately the SED fitting procedure

provides a reliable estimate for the contributions of the AGN activity and star formation. Finally, in Section 2.5 I discuss a new colour diagnostic for identifying AGN using *Herschel* photometry.

2.2 Catalogues and Data

2.2.1 X-ray Sample

The *Swift* Burst Alert Telescope (BAT) (Gehrels et al. 2004; Barthelmy et al. 2005) has conducted an all-sky survey in the ultra-hard X-ray wavelengths (14 – 195 keV) and detected 1171 hard X-ray sources at z ≅ 0 – 3.6. These high energy X-rays have a particular advantage over other wavelengths since that they can provide a direct line of sight to the AGN with as little contamination from the host galaxy while reducing selection effects due to obscuring dust and gas (Brandt & Alexander 2015).

Our sample of local AGN has been selected from the 58 month *Swift*-BAT catalog (Baumgartner et al. 2013) with a redshift cut-off at z ≤ 0.05 (Melendez et al. 2014; Shimizu et al. 2015) providing us with a total sample of 313 AGN (139 Seyfert 1-1.5s, 169 Seyfert 1.8-2s, 4 Liners, and 1 unidentified AGN; see Shimizu et al. 2015). In Figure 2.1, we present the bolometric AGN luminosity, calculated from (14 – 195 keV) X-ray BAT luminosity (L_{BAT}) using Winters et al. (2012) relation, versus redshift for our local AGN sample. Winter et al. (2012) determined the bolometric conversion using the *Swift*-BAT luminosity which was found to have a correlation coefficient of $R^2 = 0.82$. In order to be consistent with Stanley et al. (2015) we shall use this relation throughout our results which is defined as:

$$\log(L_{BOL}) = 1.1157\, x \log(L_{BAT}) - 4.2280 \qquad (2.1.1)$$

However, X-ray observations on their own will miss heavily obscured AGN (Treister et al. 2008, Alexander et al. 2008). This is despite being used extensively to measure the amount of absorbing gas in the nucleus of an active galaxy (e.g. Mullaney et al. 2009). Although finding the evidence of ultra-obscured SMBH provides a challenge (Comastri et al. 2015). Additionally, X-rays do not directly measure the total accretion

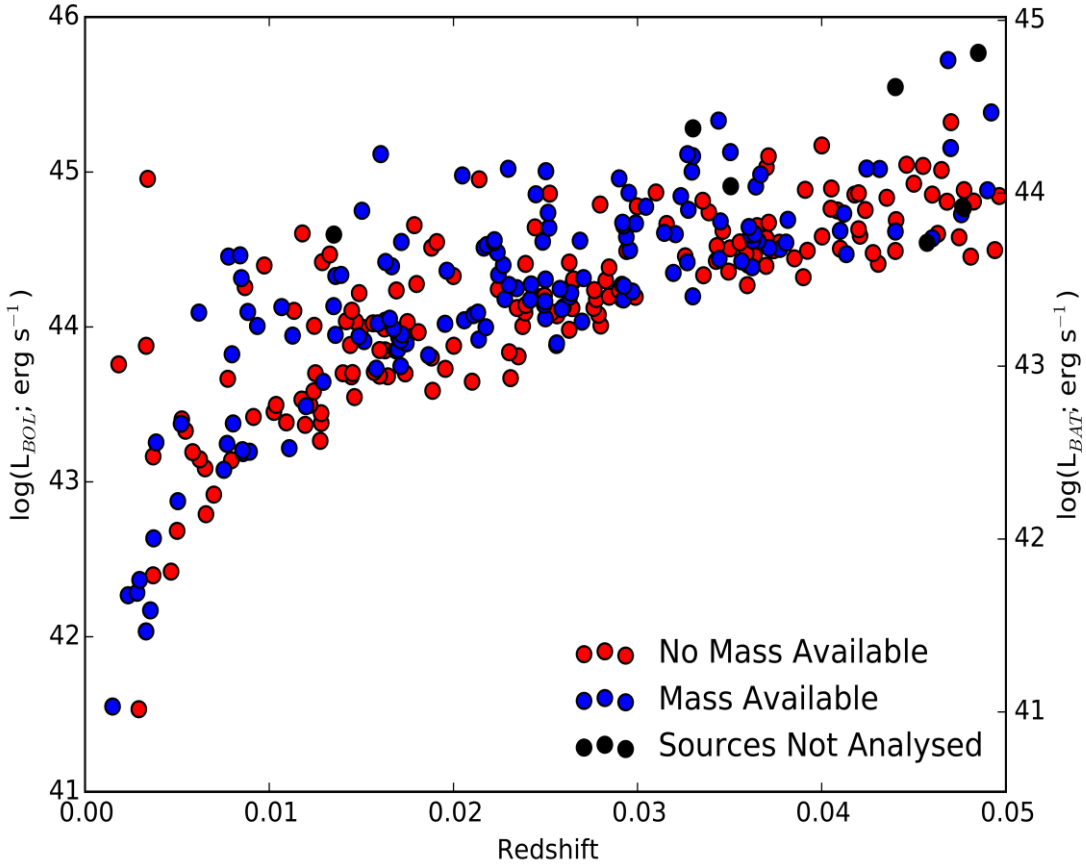

Figure 2.1: Bolometric AGN luminosity (calculated from the X-ray BAT luminosity (L_{BAT} ; 14-195 keV) using Winter et al. 2012 relation) as a function of redshift. The total AGN sample of 313 sources as originally presented in Melendez et al. (2014) with a redshift cut-off of $z \leq 0.05$. Overall, 141 sources have a stellar mass measurement (blue filled) provided in Koss et al. (2011). We have marked seven sources (black filled) not used in any analyses (since they exhibit radio characteristics or do not have mid-infrared photometry to successfully constrain the AGN and star formation contributions) although their respective SEDs are presented in Appendix A.

disk luminosity (see Figure 1.2 in Harrison 2016) which will lead to uncertainties in the derived bolometric luminosities (L_{BAT}).

2.2.2 Mid- Infrared and Far-Infrared Photometry

Our entire local AGN sample has been observed by *Herschel* providing, for the first time, publically available, sensitive photometry in the far-infrared bands 70 – 500μm (Melendez et al. 2014; Shimizu et al. 2015). One of the primary challenges of using *Herschel* far-infrared photometry is the low detection rate of individual sources at high redshift studies (e.g. Stanley et al. 2015). In Stanley et al. (2015) about 75% of their X-ray detected AGN sample only have an upper limit to their star-formation luminosities due to: (1) limiting photometry where many *Herschel* photometric measurements are upper limits and (2) some are AGN dominated and therefore have star formation upper limits. Our study is not affected by this as opposed to Stanley's study since our sample is at $z \approx 0$ and enjoys about 80% detection rate in the three shorter wavelengths (≈95% for just the 70μm band alone). This complete set of photometry gives us a great opportunity to determine the most accurate star formation rates of local AGN. Using both the PACS (70 and 160 μm; Melendez et al. 2014) and SPIRE catalogs (250, 350 and 500 μm; Shimizu et al. 2015) we compile 5σ detected photometry. The *Herschel* detection rates to each individual band of far-infrared wavelength is shown in Table 2.2, with 143 AGN (46%) having good detections in all five wave bands. A detailed description to the observations and data reductions of both the *Herschel* PACS and SPIRE photometry are available in Melendez et al. (2014) and Shimizu et al. (2015) respectively.

Additionally we cross matched our AGN sample with the Wide-Field Infrared Sky Explorer (WISE, Wright et al. 2010) entire sky catalog to extend our sample's photometry to cover the mid-infrared (3.4, 4.6, 12, 22 μm) range. The ALLWISE survey pipeline provides several different photometric measurements across the four wave bands. For this research we use the photometric measurements obtained from the Point Spread Function (PSF) decomposition of point sources (i.e. the profile-fitting photometry). A secondary photometric measurement is made using an elliptical

WISE Wavelength Bands	Total Number	Mpro (χ^2<3) (1)	Gmag (χ^2>3) (2)	Mpro (χ^2>3) (3)
3.4 μm	313	45	255	13
4.6 μm	313	127	176	10
12 μm	312*	213	89	10
22 μm	312*	283	23	6

Table 2.1: The number of sources per band that use profile fitted (mpro) photometry or elliptical aperture (gmag) photometry obtained from the WISE database. (1) Number of sources with reduced $\chi^2 < 3$ and therefore use profile fitted photometry. (2) Number of sources with reduced $\chi^2 > 3$ and therefore use elliptical aperture photometry. (3) Number of sources with reduced $\chi^2 > 3$ and therefore use profile fitted photometry since elliptical aperture photometry is unavailable.

*excluding MRK 3

Bands	Number of AGN detected in each Band
PACS 70/160 μm	296/260
SPIRE 250/350/500 μm	269/226/143
Subarcsecond Resolution 12/18 μm	80/22

Table 2.2: Mid-infrared and far-infrared coverage of X-ray detected AGN. PACS and SPIRE far-infrared data is provided from Meléndez et al. (2014) and Shimizu et al. (2015) respectively. The subarcsecond resolution mid-infrared data is given by Asmus et al. (2014).

aperture; this measurement captures the total true brightness. We use elliptical aperture when the profile-fitted photometry is a bad representation of the flux profile of resolved objects (as described by the reduced χ^2 of the profile fit). This mid-infrared photometry provided by WISE helps to build a broad coverage of the mid-to-far-infrared SEDs to reliably decompose the AGN and star formation contributions (since it is widely believed that the AGN typically dominates the mid-infrared emission and the star formation typically dominates the far-infrared emission; Mullaney et al. 2011).

With the exception of MRK 3, all of our local AGN sources are found in the ALLWISE catalog with flux estimations via profile-fitting photometry in all wave bands. If a source has been observed in the Two-Micron All Sky Survey (2MASS) Extended Source Catalog (EXC) then elliptical aperture photometry has been measured. However, as some sources contain both magnitudes, and the profile-fitted photometry would underestimate the flux, then we have to choose which photometry to take for each source. With this we used the reduced chi-squared (χ^2) test from the profile-fitting to assess the quality of the photometry. Should the test provide $\chi^2 < 3$ then the fit performed is satisfactory and so the profile-fitting photometry are selected. However, if $\chi^2 > 3$ then the profile fit is not accurate and the source is considered extended, therefore we select the elliptical aperture photometry to resolve this. As some sources are not in the 2MASS EXC catalog then we must use the profile-fitting photometry for completeness of our AGN sample when $\chi^2 > 3$. A breakdown for the number of sources using either profile fitted or elliptical aperture photometry across the four bands is shown in Table 2.1. The 3.4 and 4.6μm waveband measurements for the entire AGN sample are obtained, while the other wavebands 12 and 22μm are obtained for nearly the entire parent sample with the exception of MRK 3 where no useful brightness estimate could be made in the profile-fitting or elliptical aperture fitting. We provide the best-fitted SED solution of MRK 3 in Appendix A, but note that it is not used in any further analysis in this thesis since the unreliable photometry means that we cannot provide a precise estimate for the star formation. Similarly, we exclude six other objects (2MASXJ23272195+1524375, 3C111, 3C120, HB890241+622, PICTORA and PKS2331-240) since they are radio sources which have contamination from synchrotron emission in the far-infrared[1]. We identify these

seven objects (including MRK 3) as black filled circles in Figure 2.1.

While the *Herschel* and WISE photometry are applied to our SED fitting procedure, as shown in Section 2.3, it is necessary to assess the accuracy of our best-fitted SED solutions. For this, publically available subarcsecond-resolution mid-infrared photometry of local AGN (with wavebands 12 and 18μm; Asmus et al. 2014) is adopted. Subarcsecond-resolution data allows us to more reliably isolate the AGN emission across the central nucleus and produce nuclear photometry that can be compared to in our SED fitting results. Asmus et al. (2014) states that the majority (73 AGN) of BAT mid-infrared images were obtained with the European Southern Observatory (ESO) Very Large Telescope (VLT) spectrometer and imager for the mid-infrared (VISIR). Cross matching this data with our local AGN sample gives us 80 sources in total (≈26% of the parent AGN sample) with accurate mid-infrared photometry (see Table 2.2). Details of how this photometry is implemented into the fitting procedure to constrain our AGN template in the SED solutions are provided in Section 2.4.

2.3 SED fitting procedure and measuring average SFRs.

The main focus of this thesis is to compute star formation rates for local galaxies hosting an AGN. To do this we must compute the infrared luminosity due to star formation, $L_{IR,SF}$, which is typically performed in one of two ways. The first approach is by following many earlier studies and using the total luminosity in a far-infrared band, e.g., at 60μm (L_{60}) as a proxy of star formation (e.g. Shao et al. 2010, Rosario et al. 2012). The advantage of this approach is that it is simple but the disadvantage is that it does not account for the contamination from the AGN in the mid-infrared emission which could lead to an over-estimation of the star formation, especially for highly luminous AGN ($L_X > 10^{45}$ erg s^{-1}). The second approach and the preferred method we use in this thesis is by decomposing the contribution of AGN activity and star formation, which peak in the mid-infrared and far-infrared respectively, from the overall SED of each source using the mid-infrared and far-infrared photometry where

[1] Sources which have the ratio $S_{500\mu m}/S_{350\mu m}$ >1 show that these radio-loud sources contain excess synchrotron radiation due to their radio jets and allow a significant contribution to their far-infrared emission."

available, thus computing individual $L_{IR,SF}$ for all of our local AGN sample. This provides the advantage of determining a more accurate contribution to the star formation in each source than by simply taking L_{60}.

Explored in Section 1.4, most of the mid-infrared and far-infrared emission is a consequence of the dust heating by accretion onto a SMBH and by young stars respectively. Since the accretion disk is much hotter than young stars the dust being heated by star formation is colder than the dust heated by the AGN, thus the bulk of the AGN emission is produced at shorter mid-infrared wavelengths and drops off at far-infrared wavelengths (e.g., Mullaney et al. 2011). Since the AGN emits at infrared wavelengths, this will result in an overestimation of the SFR if it is not accounted for, which is why we perform a decomposition method in our fitting procedure to isolate the AGN from the star formation component. Therefore, in order to calculate $L_{IR,SF}$ values, we adopt a similar method as presented by Stanley et al. (2015). We fit the infrared data of our sample with a set of empirical templates, originally defined in Mullaney et al. (2011), consisting of a mean AGN template and five star-forming galaxy templates. In order to account for as much of the mid- to far-infrared colour space as possible the galaxy templates of Arp220 from Silva et al. (1998) and a dusty star-forming template from the Dale and Helou (2002) library are also included so that our SED fitting technique covers extreme star forming galaxies. Figure 2.2 presents all seven star-forming templates used in this study. As justified in Stanley et al. (2015) the motivation behind having a small number of templates in the SED fitting is to avoid degeneracy in the SED fitting solution given the limited amount of photometry. The seven templates cover a wide range of empirical shapes.

We constrain the SEDs of our sources by using the flux densities at 12μm, 22μm from WISE and 70-500μm from *Herschel*. The more photometric measurements of flux density that are available improve the accuracy of constraining the contribution of the AGN and the star formation to the SEDs of each source. Additionally, the broad wavelength range of data helps to improve the accuracy of constraining the two contributions, for example, in Figure 2.2 the Dale & Helou (2002) and Starburst 5 (SB5) templates are relatively similar in shape up to 100μm but then SB5 drops off

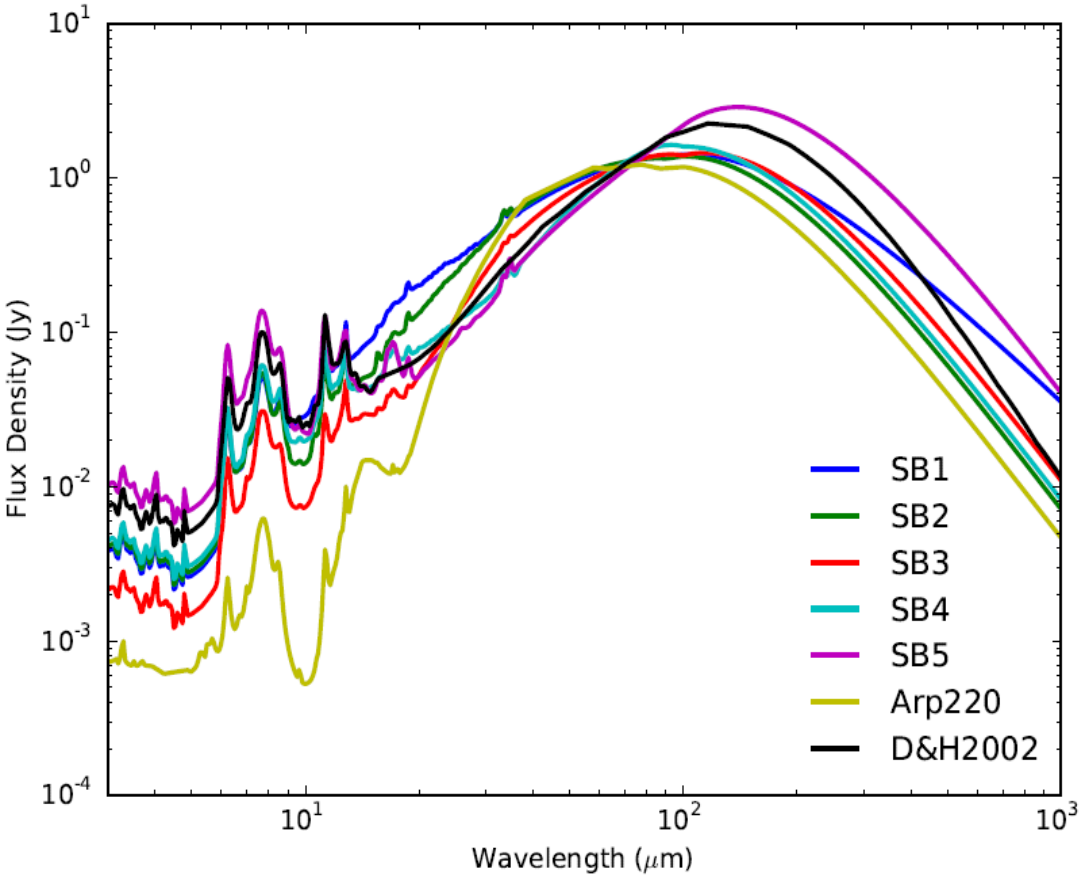

Figure 2.2: The SEDs of the seven star-forming templates used to fit the data of our sample. The starburst templates (SB1–SB5) are from Mullaney et al. (2011). We include the Arp220 galaxy template from Silva et al. (1998) to cover extreme star forming systems and an additional Dale & Helou (2002) galaxy template to allow more range in galaxy SED shapes.

quicker than the Dale & Helou (2002) template in the far-infrared, therefore the choosing of these two templates is possibly dependent on the *Herschel* SPIRE photometry. The flux densities from the 3.4 and 4.6μm bands from WISE are not included in the SED fitting process since we wish to avoid contamination by the older stellar population within the host galaxy.

In the SED fitting procedure the only free parameters are the normalization of the AGN template and star forming galaxy template for each source. Therefore, we require at least three photometric detections to fit both the templates together. If the case arises where there are less than three photometric detections we can only estimate upper limits on $L_{IR,SF}$ since it is not possible to constrain both the AGN and star formation components. All of our models are fitted to the detected photometric flux density measurements. However, for flux density upper limits we only allow fits where the star formation component does not exceed any of the 5σ upper limit values. For the case when we have three or more photometric detections we can simultaneously constrain the AGN and star forming galaxy templates.

In the first step we create two sets of SED solutions. Both sets involve fitting the data with each of the seven star forming galaxy templates separately but the second set involves fitting the star-forming templates in combination with the AGN template, resulting in 14 separate SED solutions. In order to determine the best fitting solution of these 14 different SED solutions we use the Bayesian Information Criteria (BIC; Schwarz 1978) which is defined as:

$$BIC = -2\ln(L) + k\ln(N) \tag{2.2.2}$$

where L is the maximum likelihood, k is the number of free parameters, and N is the number of data points. This provides a method to select the best-fitting SED solution out of a finite set of solutions because the BIC method favours smaller finite set of solutions as opposed to its rival the Akaike Information Criterion (1973). For each of the 14 separate SED solutions a BIC value is calculated. Typically, the SED with the lowest BIC value is considered to be the best-fitted SED solution out of the possible 14 solutions. If other SED solutions do not have a BIC value within $\Delta_{BIC} = 2$ of the lowest BIC value then the SED solution with the lowest BIC value is considered the best-

fitted solution. If other SED solutions have a BIC value within $\Delta_{BIC} = 2$ of the lowest BIC value then these solutions are considered equally good. If the latter case occurs then we simply take the average of these best-fitting solutions. In Appendix A we present the best-fitting SED solutions, whether it has been a single best template fit or an average best fit of different solutions, and which star forming galaxy templates were the best fits.

Figure 2.3 identifies four example best-fitting SED solutions from our sample. Figure 2.3(a) shows a best-fitting SED solution with more than three photometric data points that includes the combination of the AGN and star forming component. Figure 2.3(b) is a best-fitting SED solution with more than three photometric data points, that contains only the star forming component and no AGN component is required. Figure 2.3(c) and 2.3(d) are examples of best-fitting SED solutions with less than three photometric flux density detections where we increase the normalisation of each star forming galaxy template until it reaches one of the 5σ upper limits (with the exception of the 70μm upper limit data). Figure 2.3(c) shows the best-fitting AGN component with an upper limit star forming component, while Figure 2.3(d) shows a best-fitting star forming component with an upper limit AGN component. From the best-fitting SED solution we calculate the integrated 8-1000 μm infrared luminosity of the star formation component $L_{IR,SF}$, though examples like Figure 2.3(c) and 2.3(d) of $L_{IR,SF}$ will be an upper limit value. Note that for examples like Figure 2.3(a), 2.3(c) and 2.3(d), where the AGN contribution to the total SED is identified we can calculate the integrated 8-1000 μm infrared luminosity of the AGN component ($L_{IR,AGN}$). However, examples like Figure 2.3(b) $L_{IR,AGN}$ would be an upper limit value.

One of the challenges we faced in fitting the photometric data was that the PACS 70μm photometry appeared to cause the best-fitting SED solutions to be systematically underestimated. An example of this can be seen in Figure 2.3(b) where we have obtained a reasonable fit with the photometric data points used in the fitting procedure with the exception of the 70μm data point. To explore this issue we performed the SED fitting both with and without the 70μm data and compared the $L_{IR,SF}$ values (see Figure 2.4). We found that the 70μm included into the fitting procedure underestimates the star formation by an average of 0.2 dex. We therefore decided to exclude the 70μm from all the SED fits. A possibility as to why this is the

case is that a majority of these sources have significant AGN contribution to the 70μm. A study by Shimizu et al. (2017) found that nearly 30% of the BAT sample had a 50% or more contribution towards the 70μm by AGN-heated dust. This consequently means that the amount of star formation observed at this waveband is reduced. They also note that the 70μm emission is the only waveband with this kind of AGN contribution. If we compare the 70μm *Herschel* photometry with the 60μm IRAS photometry (see Figure 2.5), assuming that both sets of photometry are reliable, there does not appear to be any significant discrepancies and that they remain fairly consistent. Since IRAS has a lower sensitivity then any detected flux for fainter sources is most likely being overestimated. However, there is a large scatter witnessed in a considerable number of sources from the SED fits at 70μm (see Appendix A) than would be predicted by the fits. Rosario et al. (2017) finds a similar behaviour for a subset of nearby BAT AGN which uses an independent modelling approach, which would further suggest that the discrepancy is being caused by an underlying issue with the SED models that we have chosen.

Overall from the SED fitting to the 313 sources in our AGN sample, 207 best-fitting SEDs required a contribution from the AGN and star formation, 74 best-fitting SEDs required only a star-forming contribution and 32 best-fitting SEDs had upper limits on the star formation component due to a low number of photometric detections. All of the best-fitting SED solutions for our sample are presented in Appendix A, and for completeness, we included the seven sources that are not going to be implemented in any further analysis of this thesis.

Having determined the individual $L_{IR,SF}$ values for our X-ray AGN sample, we calculate the average star formation rates as a function of bolometric AGN luminosity and redshift. As noted earlier in this Section 1.4.1, the bolometric AGN luminosity can be calculated from the BAT luminosity using the Winter et al. (2012) relation. In order to calculate the mean star formation rates, <SFR>, we divide the sample into L_{BOL} bins of about 45 sources per bin to ensure consistency with Stanley et al. (2015). We then calculate the mean infrared luminosity due to star formation, $<L_{IR,SF}>$, and the mean

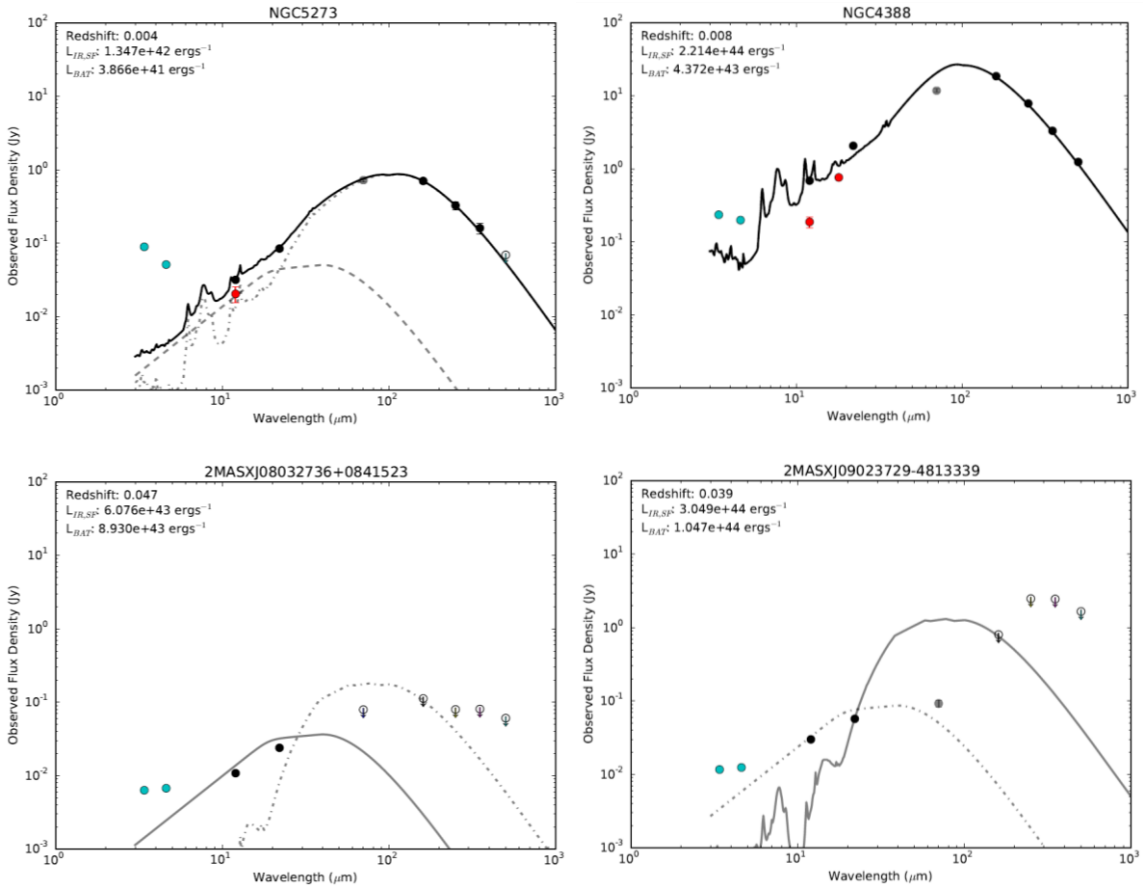

Figure 2.3: Four examples of our SED fits. In all four cases the black filled data points are measured flux densities from *Herschel* (160 – 500 μm) and WISE (12 and 22 μm) observations, the cyan filled data points are measured flux densities from WISE (3.4 and 4.6μm) observations, the red data points are measured subarcsecond-resolution mid-infrared (12 and 18μm wherever possible) photometry from Asmus et al. (2014), the grey data points are flux densities from *Herschel* at 70μm and are not used in the fitting procedure (see Section 4.2), while the empty circles with an downward arrow are flux density upper limits. Additionally, we provide the infrared luminosity due to star formation ($L_{IR,SF}$), the BAT (14-195 keV) X-ray luminosity (L_{BAT}), the redshift and the name of each source. Errors for the measure flux densities are provided but may be small. (a) The best fitting (black solid) SED solution is a combination of AGN (grey dashed) and star forming (grey dot-dashed) galaxy templates. (b) The best fitting (black solid) SED solution is that of a star-forming galaxy template with no AGN contribution. (c) The best fitting SED solution is an AGN (grey solid) that has no star formation due to limited photometric detections, so in this case we provide an upper limit (grey dot-dashed) with the star forming galaxy template that does not exceed the 160 μm data point. (d) The best fitting SED solution is a star forming (grey solid) galaxy template with no AGN contribution due to limiting photometric detections, therefore we provide an upper limit to the AGN (grey dot-dashed) contribution that does not exceed the 160μm data point.

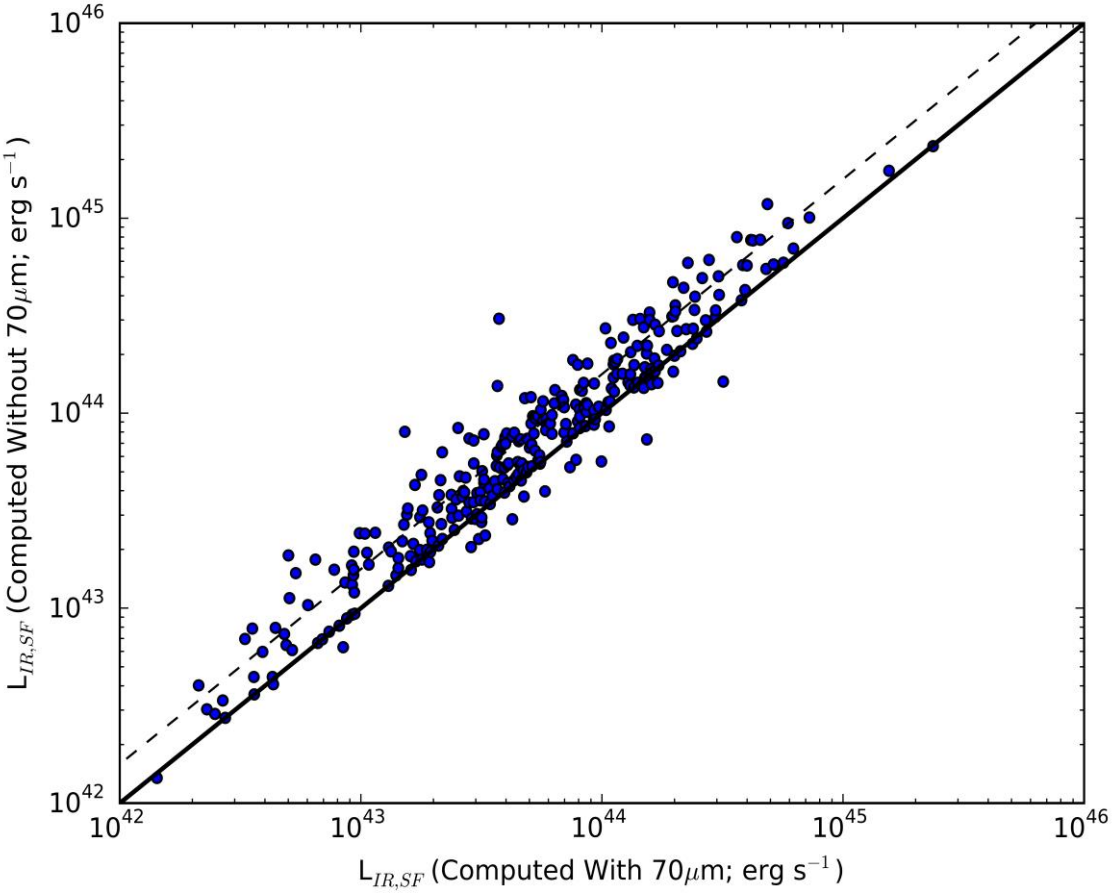

Figure 2.4: Infrared luminosity due to star formation, $L_{IR,SF}$, without the 70μm *Herschel* photometry included into the SED fitting procedure plotted against $L_{IR,SF}$ with the 70 μm included. Results of this tell us that the latter fit, in general, underestimates the star formation since sources lie above the one-one line (blue) with an average of ≈ 0.2 dex above.

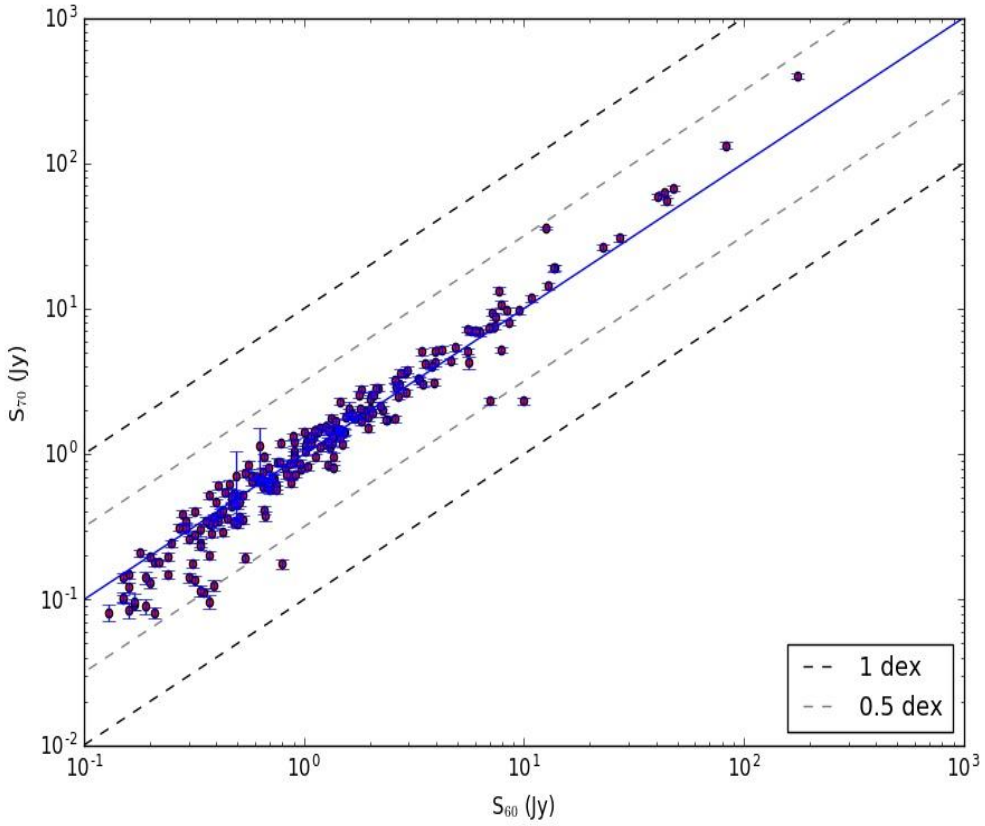

Figure 2.5: *Herschel* 70µm flux estimates against IRAS 60µm flux estimates. The (red) data points are the flux estimates with their respective (blue) error bars. An offset of 0.5 dex (grey dashed) and 1 dex (black dashed) is also provided to assess the amount of scatter witnessed, especially towards fainter sources.

bolometric AGN luminosity, $<L_{BOL}>$, per bin[2]. The errors on these binned measurements are the bootstrapped errors on the mean. This means that we take a random subsample of all AGN and recalculated the mean $L_{IR,SF}$ values 10000 times for each bin to produce a distribution and then take the 1σ error on the mean of this distribution to provide the uncertainty on the mean. Finally, the SFR can be calculated from the $<L_{IR,SF}>$ values using the Kennicutt (1998) relation corrected to a Chabrier IMF (Chabrier 2003) which is the following:

$$< SFR(M_{\odot}\, yr^{-1}) > = \frac{< L_{IR,SF}\ (erg\ s^{-1}) >}{3.7\ x\ 10^{43}} \tag{2.3.3}$$

2.4 The reliability of the SED fitting procedure

In this subsection I assess the accuracy of our SED fitting procedure using publicly available subarcsecond-resolution mid-infrared photometry at 12 and 18μm (Asmus et al. 2014) as explored in Section 2.2.2. We do this by assuming that the 12μm subarcsecond resolution photometry is totally dominated by the AGN and consequently that the AGN template can be fixed to the 12μm point. We then fit the source SEDs with the star-forming galaxy templates, including the fixed AGN component.

For the 80 sources with subarcsecond resolution 12μm data we compare the individual $L_{IR,SF}$ values calculated from the SEDs with a fixed AGN to those where the AGN component is a free parameter (see Figure 2.6). We see that most sources of this subsample have similar $L_{IR,SF}$ values. We identify the three main outliers as ESO548-G081, NGC526A and Fairall 51 and their respective SED solutions in Figure 2.7. These outliers appear to lie on an offset of 0.2 dex (black dashed lines) from the one-to-one (black) line seen in Figure 2.6. Considering that the largest outliers are only modest, and since we find good agreement in $L_{IR,SF}$ whether we fix the AGN

[2] $<L_{IR,SF}>$ is calculated with a combination of detected and upper limit $L_{IR,SF}$ values. Our upper limit values are the maximum values we calculated in our SED fitting procedure with star formation contributions not exceeding one of the 5σ upper limit flux densities (with exception to the 70μm flux density).

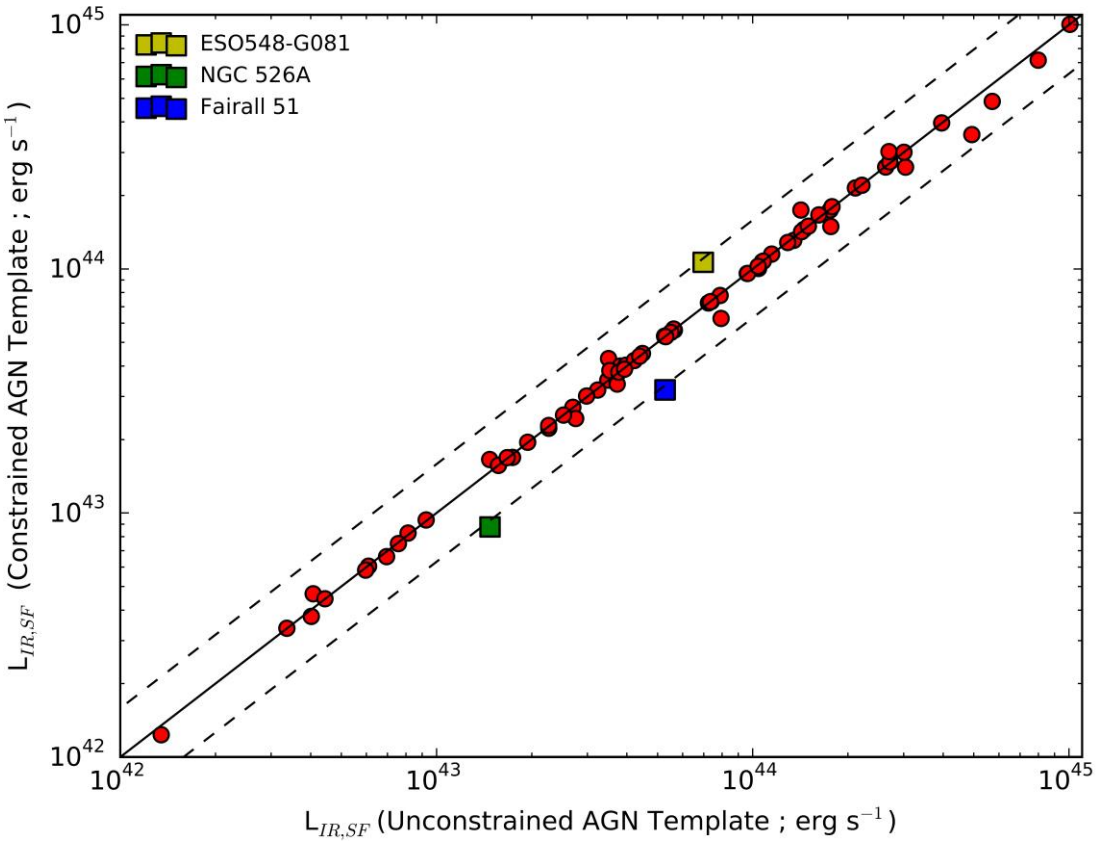

Figure 2.6: An assessment of how well the SED fitting procedure works in determining the infrared luminosity due to star formation, $L_{IR,SF}$, from sources where the AGN component is constrained to a 12μm subarcsecond resolution photometry (Asmus et al. 2014) versus $L_{IR,SF}$ where the AGN component is a free parameter. There are three major outliers within this figure and their individual best-fitting SED solutions with and without the subarcsecond resolution photometry are presented in in Figure 2.7.

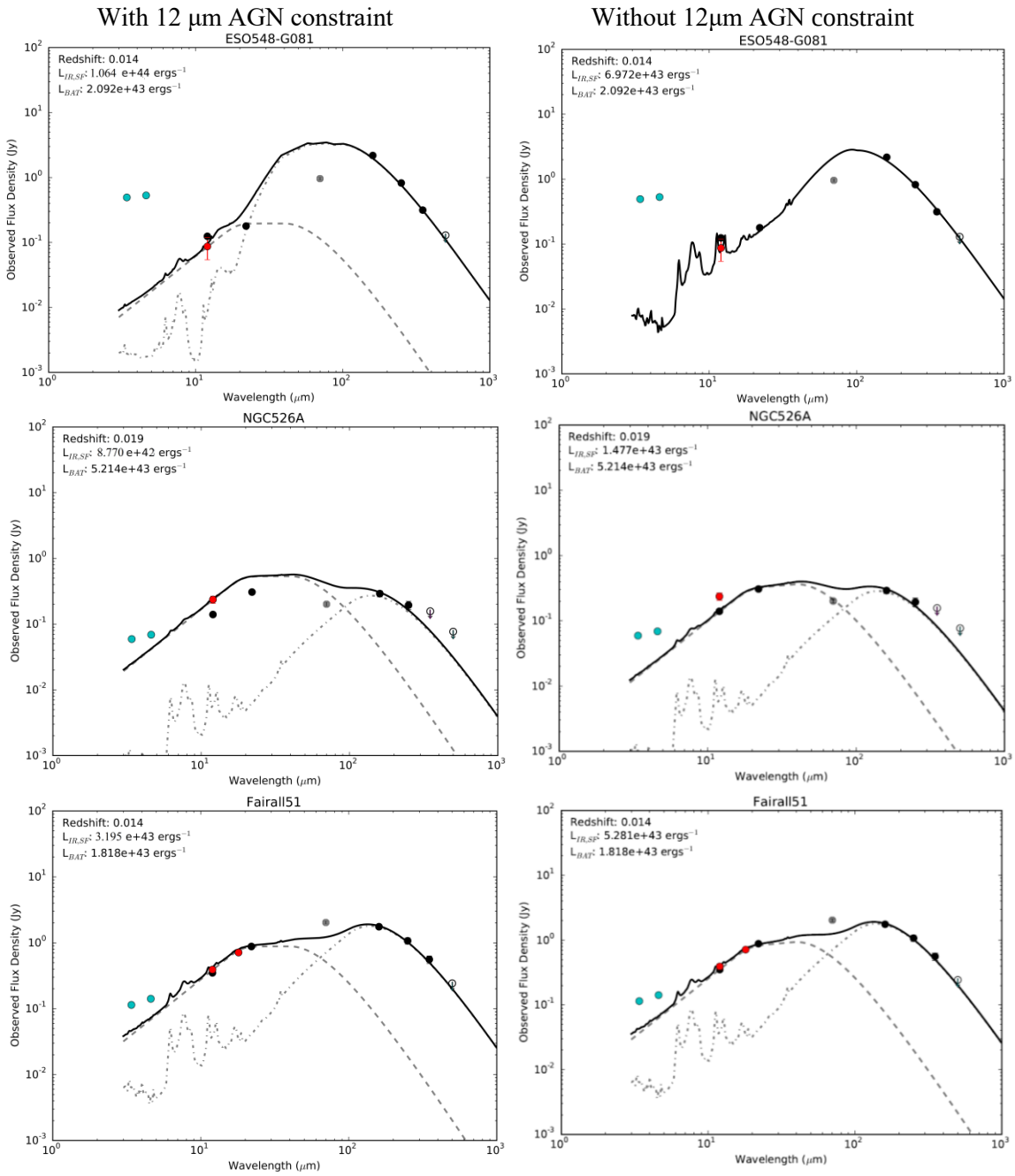

Figure 2.7: Best-fitting SED solutions for ESO548-G081, NGC 526A and Fairall 51, the three largest outliers from Figure 2.6. Left: The AGN template is fixed to the subarcsecond resolution 12μm photometry (Asmus et al. 2014). Right: The AGN template is left as a free parameter in the SED fitting procedure. In all six cases the black filled data points are measured flux densities from *Herschel* (160 – 500 μm) and WISE (12 and 22 μm) observations, the cyan filled data points are measured flux densities from WISE (3.4 and 4.6μm) observations, the red data points are measured subarcsecond-resolution mid-infrared (12 and 18μm wherever possible) photometry from Asmus et al. (2014), the grey data points are flux densities from *Herschel* at 70μm and are not used in the fitting procedure (see Section 4.2), while the empty circles with an downward arrow are flux density upper limits.

component or not we can therefore assume that our SED fitting procedure is a reliable method in measuring the $L_{IR,SF}$.

2.5 AGN selection wedge and colour diagnostic results

Using infrared photometry, SED fitting is a rather reliable method in constraining the relative contributions of the AGN and star formation activity. However, SED fitting is a comparatively complex procedure. Alternatively, there is another widely used approach that identifies the presence of AGN activity using colour-colour diagrams. Specifically, mid-infrared colours are used to assess the amount of dust heated by the AGN. Several studies have implemented an AGN wedge using IRAC colours (e.g., Lacy et al. 2004; Stern et al. 2005) and WISE colours (e.g., Mateos et al. 2012).

Mateos et al. (2012) gives a reliable mid-infrared colour selection of luminous AGN, from the Bright Ultra-Hard (4.5 – 10 keV) *XMM-Newton* Survey, by using the lower WISE bands (3.4, 4.6 and 12μm). The three-band AGN wedge (see Figure 2.8a) is defined as:

$$Y = 0.315\,X \begin{array}{l} +0.297\ (upper\ boundary) \\ -0.110\ (lower\ boundary) \end{array} \tag{2.5.4}$$

Where $X = log_{10}(f_{12\mu m}/f_{4.6\mu m})$ and $Y = log_{10}(f_{4.6\mu m}/f_{3.4\mu m})$. The bottom left mid-infrared power law α= -0.3 limit is given as

$$Y = -3.172\,X + 0.436. \tag{2.5.5}$$

As part of their analysis, Mateos et al. (2012) maximised the completeness of their mid-infrared selection by building a clean AGN sample using all of the WISE sources from the BUXS survey and detected in the 2-10 keV band (where they assume a detection in the hard X-rays is a good tracer of AGN activity). Stern et al. (2012) investigated that taking the colour cut of $[3.4] - [4.6] \geq 0.8\ (Vega)$ and a 4.6μm flux threshold of 160 μJy improves completeness, but also reduces the reliability of their results to 31.8% X-ray detected AGN. Mateos et al. (2012) acknowledges this and

further demonstrates that their WISE selection is one of the most reliable (with a 38.5% AGN found in the wedge with an X-ray detection) compared to those in literature (e.g., 31.8%; Stern et al. 2012).

In this study, using the same mid-infrared colours I apply the AGN wedge defined by Mateos et al. (2012) on the *Swift*-BAT AGN sample (see Figure 2.8a). I also define a new broader mid-to-far-infrared colour selection by introducing *Herschel* photometry in addition to the WISE photometry (see Figure 2.8b). A potential advantage of this approach over the WISE colour-colour analysis is that it is sensitive, both to the AGN and the star formation. Mateos et al. (2012) notes that mid-infrared selection techniques can by limited by the contamination from galaxies without strong AGN activity where the major contributions to the mid-infrared emission comes from the stellar population or strong star formation. Therefore, including a sensitive *Herschel* far-infrared measurement can allow a clear separation of AGN activity and star formation. This is observed in Figure 2.8b where a clear separation is made between AGN dominated sources inside the wedge and star-forming galaxies outside the wedge. Stern et al. (2012) notes that the inclusion of longer wavelengths would increase the reliability of the AGN selection but could potentially reduce completeness.

Another interesting result from Mateos et al. (2012) is the predicted WISE colours of AGN/ galaxy composite SEDs for the three-band AGN selection wedge. As presented in Figure 5 of Mateos et al. (2012) at low redshifts sources with minimal AGN activity (i.e., fractional contribution = 0%) lie outside the wedge, whereas sources with increasing fractional contributions of AGN activity are expected to lie closer or within the wedge. The transition value for AGN inside and outside the selection wedge is 50%, according to Figure 5 of Mateos et al. (2012). From Figure 2.8b, since the AGN typically peaks in the mid-infrared it is expected that AGN with high fractional contributions lie close to log (f_{160}/f_{12}) ≈ 0, whereas more star-forming galaxies will lie at log (f_{160}/f_{12}) ≥ 1 since star formation typically peaks in the far-infrared.

Referring back to Section 2.3 where the AGN activity and the star formation components of the infrared SED were computed (i.e. $L_{IR,SF}$ and $L_{IR,AGN}$). It was found that 66.0% of sources successfully constrained both the AGN and star formation

contribution, 23.5% constraining only the star formation contribution and 10.5% as upper limits providing an estimate of both the AGN and star formation contribution. Here, the fractional contribution of the AGN for each source is calculated as:

$$AGN\ Fraction\ (\%) = \frac{L_{IR,AGN}}{L_{IR,AGN}+L_{IR,SF}}. \quad (2.5.6)$$

For SEDs that only required a star-forming galaxy template, the AGN fraction is set to a maximum of 20%. The fraction is set to a maximum of 20% as these are clearly star forming galaxies (on the visual inspection of the SEDs and have only constrained a star-forming template) which do not have much in the way of AGN contribution.

It becomes apparent that as the fractional AGN contribution increases the more likely AGN lie inside the selection wedge (see Figure 2.9a). AGN with a fractional contribution greater than 50% most likely lie within the selection wedge which agrees well with the results in Mateos et al. (2012) and provides further evidence that the three-band selection wedge is an effective method for broadly selecting more luminous AGN sources than star-forming sources (see Table 2.3). This is much clearer in Figure 2.9b where the additional far-infrared data show that highly dominant AGN (80-100% AGN fraction) peak in the mid-infrared regions (i.e. log (f_{160}/f_{12}) ≈ 0) as opposed to weakly dominant AGN (0-20% AGN fraction) which peak in the far-infrared regions (i.e. log (f_{160}/f_{12}) ≈ 1.5). Similarly, the composite AGN also follow this mid-to-far-infrared transition. The AGN fractional group 20 – 50% (28.6% of the AGN sample), appear more star-forming by peaking at log (f_{160}/f_{12}) ≈ 1 than the fractional group 50-80% (17.6% of the AGN sample) which peaks at log (f_{160}/f_{12}) ≈ 0.5.

However, this is all under the assumption that using ultra-hard band (14-195 keV) X-ray detected AGN agrees well with the 2-10 keV X-ray band used for the three band AGN selection wedge. As found by Mateos et al. (2012) the mid-infrared bright AGN are predominantly X-ray luminous (typically around $L_{2-10} \geq 10^{43}$ erg s^{-1}; see Table 4 in Mateos et al. 2012). In Figure 2.10(a) this is similarly the case where most AGN with ultra-hard band X-ray luminosities greater than $10^{43.5}$ erg s^{-1} lie within the selection wedge (see Table 2.4) showing that the *Swift*-BAT AGN sample is relatively bright at mid-infrared wavelengths.

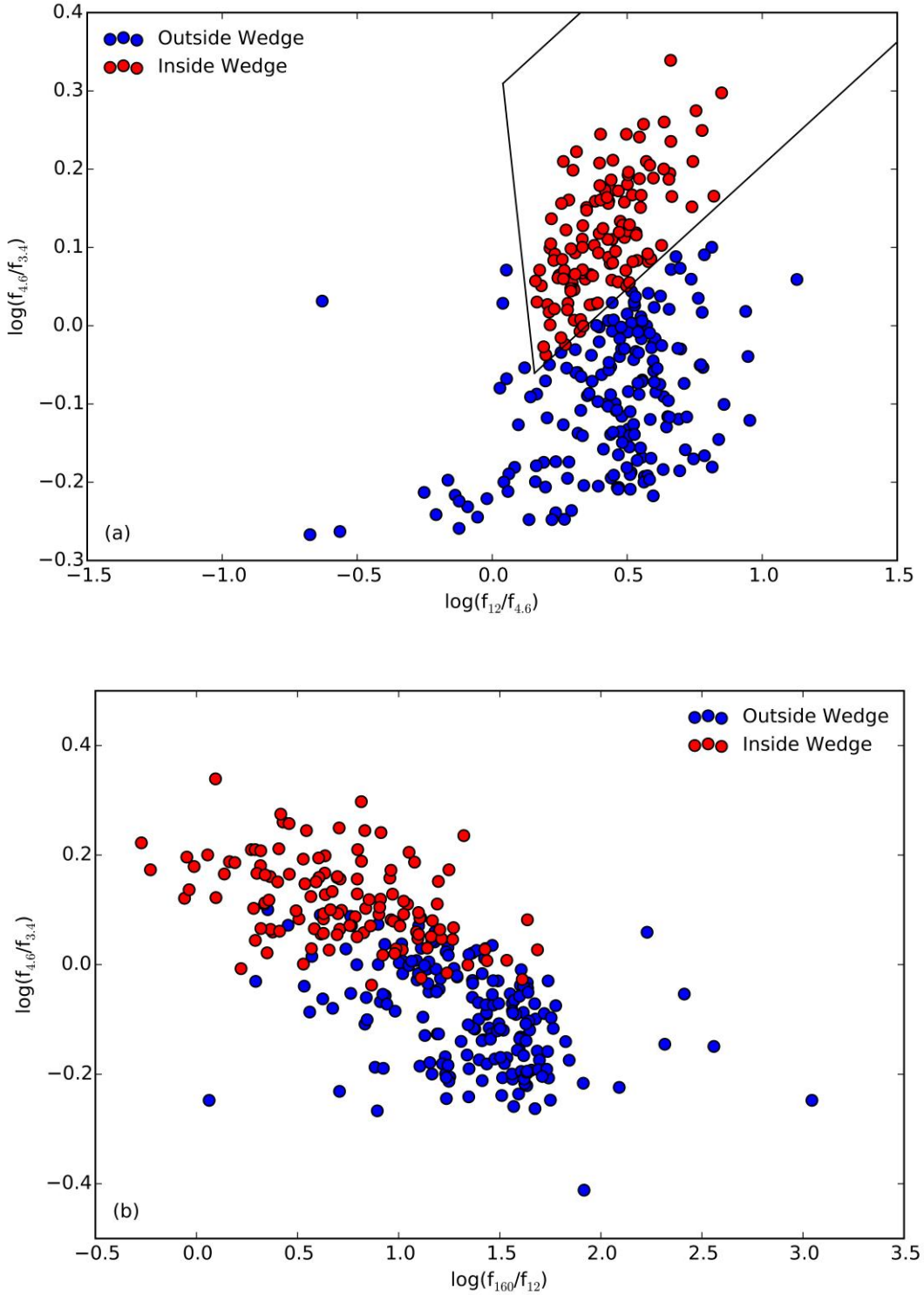

Figure 2.8: Colour-colour plots for *Swift*-BAT AGN sample with AGN selection (red filled; selecting sources within the AGN wedge) compared with star-forming selection (blue filled; selecting sources outside the AGN wedge). Top: Mid-infrared colour selection with an AGN wedge as defined from Mateos et al. (2012) for luminous X-ray detected AGN using WISE wavebands. Bottom: Mid-to-far-infrared colour selection that demonstrates the use of both WISE and *Herschel* waveband photometry.

AGN Fraction Groups	Inside AGN wedge[(a)]	Outside AGN wedge[(a)]	Total number of sources[(b)]
0-20%	12 (10%)	106 (90%)	118(39%)
20-50%	22 (25%)	66 (75%)	88 (29%)
50-80%	46 (85%)	8 (25%)	54 (18%)
80-100%	13 (93%)	1 (7%)	14 (5%)
No fraction available*	20 (63%)	12 (38%)	32 (11%)

Table 2.3: The results from calculating the AGN fraction of each AGN: (a) the percentage of sources in a specific AGN fraction group inside/outside the selection wedge, (b) the percentage of AGN present in each group with respect to the whole AGN sample.

* AGN that have an upper limit on the AGN activity or star formation are put in this group.

	Inside AGN wedge	Outside AGN wedge	Total number of sources
$L_{BAT} < 10^{43}$ erg s^{-1}	5 (9%)	54 (92%)	59(19%)
$L_{BAT} = 10^{43\text{-}43.5}$ erg s^{-1}	29 (30%)	67 (70%)	96(31%)
$L_{BAT} = 10^{43.5\text{-}44}$ erg s^{-1}	64 (54%)	54 (46%)	118 (39%)
$L_{BAT} > 10^{44}$ erg s^{-1}	28 (85%)	5 (15%)	33 (11%)

Table 2.4: Results of taking the *Swift*-BAT luminosity, L_{BAT}, with respect to the AGN selection wedge: (a) the percentage of sources in a specific L_{BAT} group inside/outside the selection wedge, (b) the percentage of AGN present in each group with respect to the whole AGN sample.

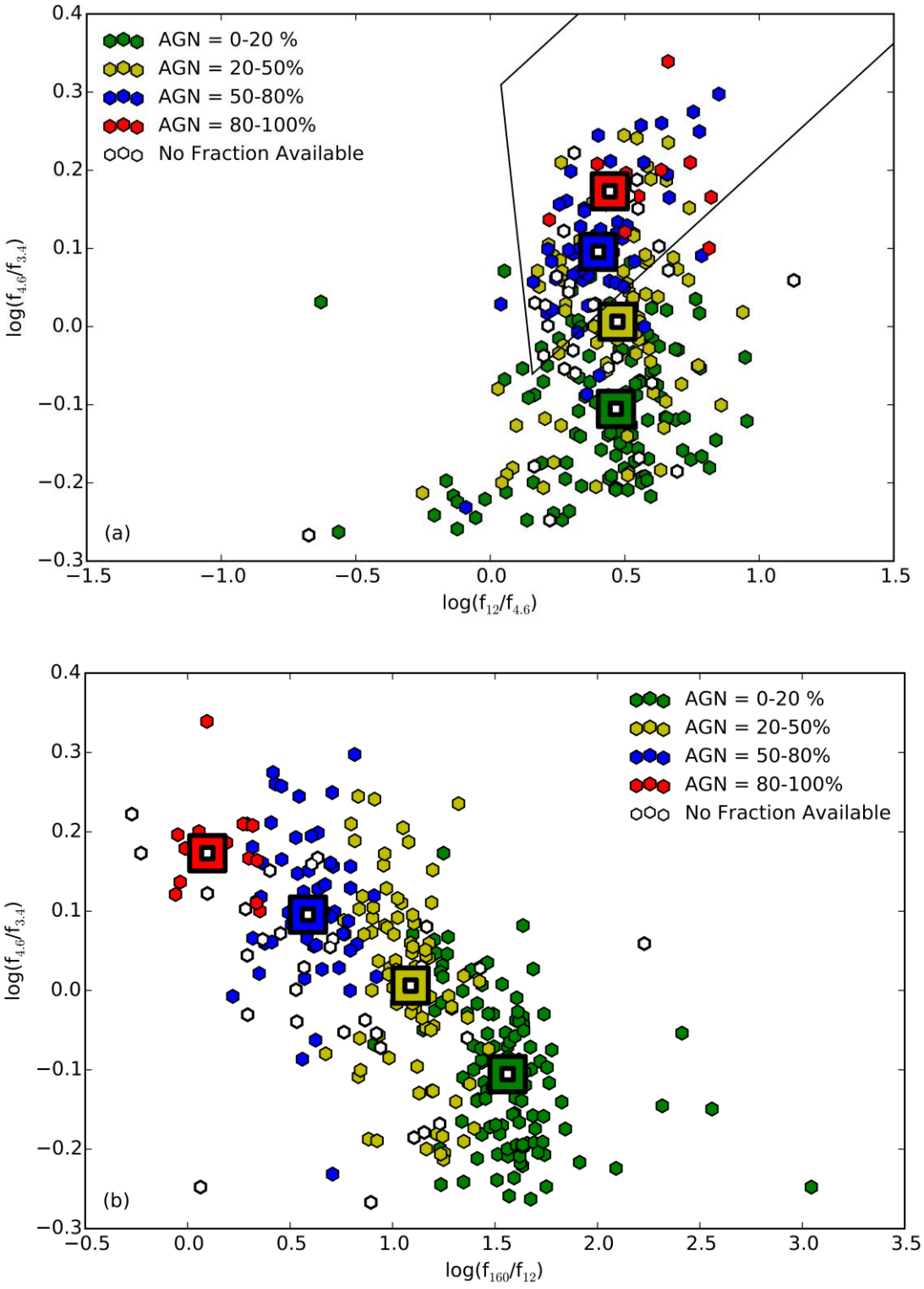

Figure 2.9: Colour-colour plots for *Swift*-BAT AGN sample with AGN selection based on AGN fraction. Top: Mid-infrared colour selection with an AGN wedge as defined from Mateos et al. (2012) for luminous X-ray detected AGN using WISE wavebands. Bottom: Mid-to-far-infrared colour selection that demonstrates the use of both WISE and *Herschel* waveband photometry. The larger filled circles with white dots are averages for each bin of AGN fractional contribution.

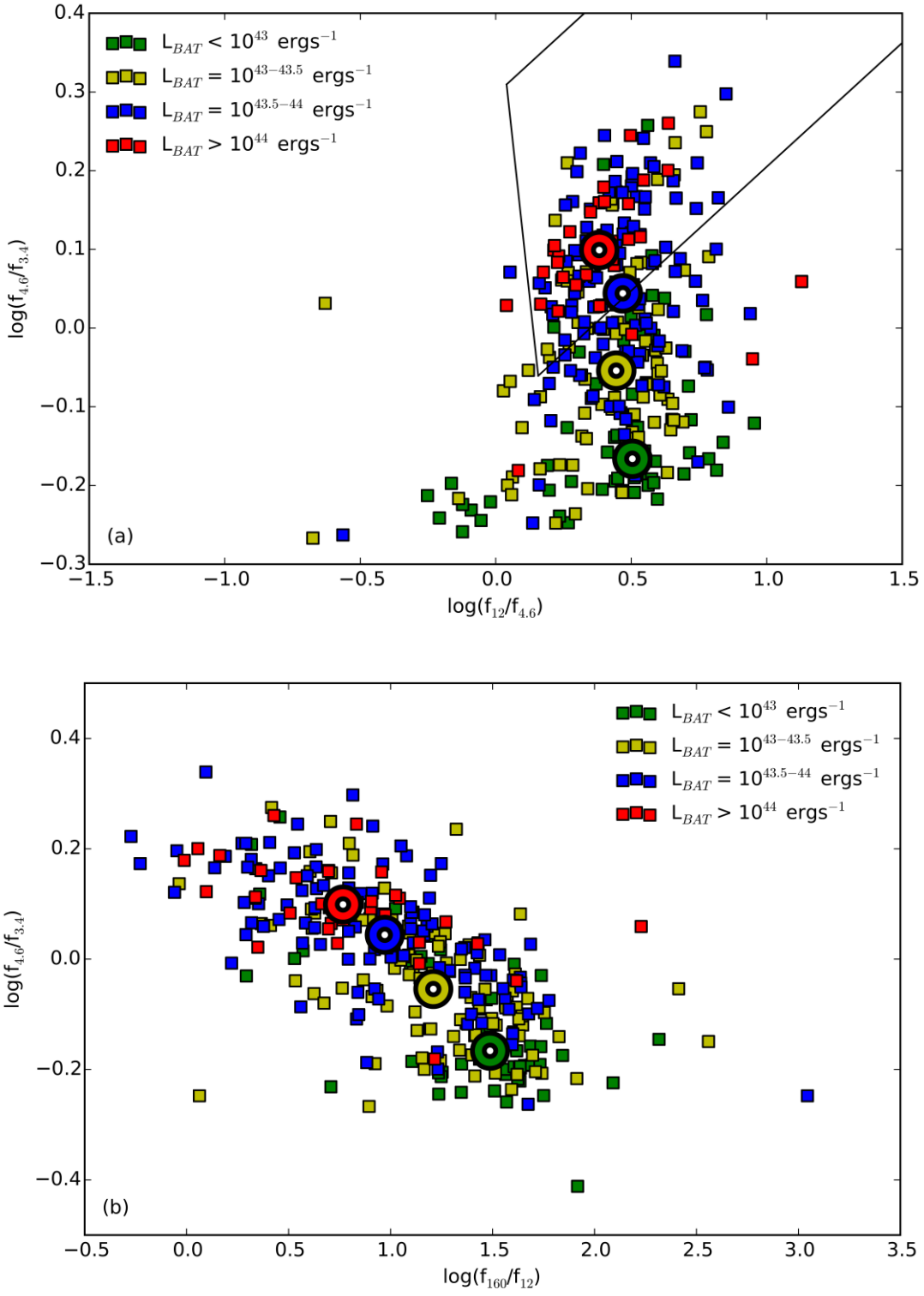

Figure 2.10: Colour-colour plots for *Swift*-BAT AGN sample with AGN selection based on the *Swift*-BAT X-ray luminosity, L_{BAT}. Top: Mid-infrared colour selection with an AGN wedge as defined from Mateos et al. (2012) for luminous X-ray detected AGN using WISE wavebands. Bottom: Mid-to-far-infrared colour selection that demonstrates the use of both WISE and *Herschel* waveband photometry. The larger filled circles with white dots are averages for each bin of BAT luminosity.

CHAPTER 3

Results and discussions of the mean SFR for local Active Galactic Nuclei

Following on from Chapter 2, where I discussed the fitting of infrared photometry with star-forming and AGN templates, I go on to discuss the results of this thesis. In this chapter, I will calculate the mean star formation rates as a function of bolometric AGN luminosity and analyse what this result means.

3.1 The mean SFR vs. bolometric AGN luminosity

Using the SED fitting procedure described in Section 2.3 on the X-ray detected sample of AGN a measurement of the infrared luminosity due to star formation, $L_{IR,\ SF}$, was calculated for each source. This value is then converted into SFRs using the Kennicutt (1998) relation corrected using a Chabrier IMF (Chabrier 2003). It is found that the individual SFRs of our sample agree generally with those of Shimizu et al. (2015) in that the SFR of BAT AGN hold values similar (within 1σ errors) to those found within this study indicating that the procedure used in Section 2.3 is well-suited. In order to be consistent with Stanley et al. (2015) the mean SFR is calculated in bins of ≈ 44 sources per bin across the bolometric AGN luminosity (L_{BOL}) range (see Figure 3.1) where each bin has calculated 1σ bootstrapped errors (see Table 3.1) on the mean. In Figure 3.1, there are a total of 274 detected $L_{IR,\ SF}$ (black filled circles) and 32 upper limit $L_{IR,\ SF}$ (empty circles). Additionally, Figure 3.1 also has a cyan shaded region indicating the 16^{th} and 84^{th} percentiles of the bootstrapped errors for each bin. In order to be consistent with how the upper limits are treated with the mean SFR, the upper limits are set to the value of zero in order to test whether or not they produce a major difference in the results of Figure 3.1. They make an insignificant difference between taking the mean SFR with maximum upper limits or upper limits set to zero, therefore

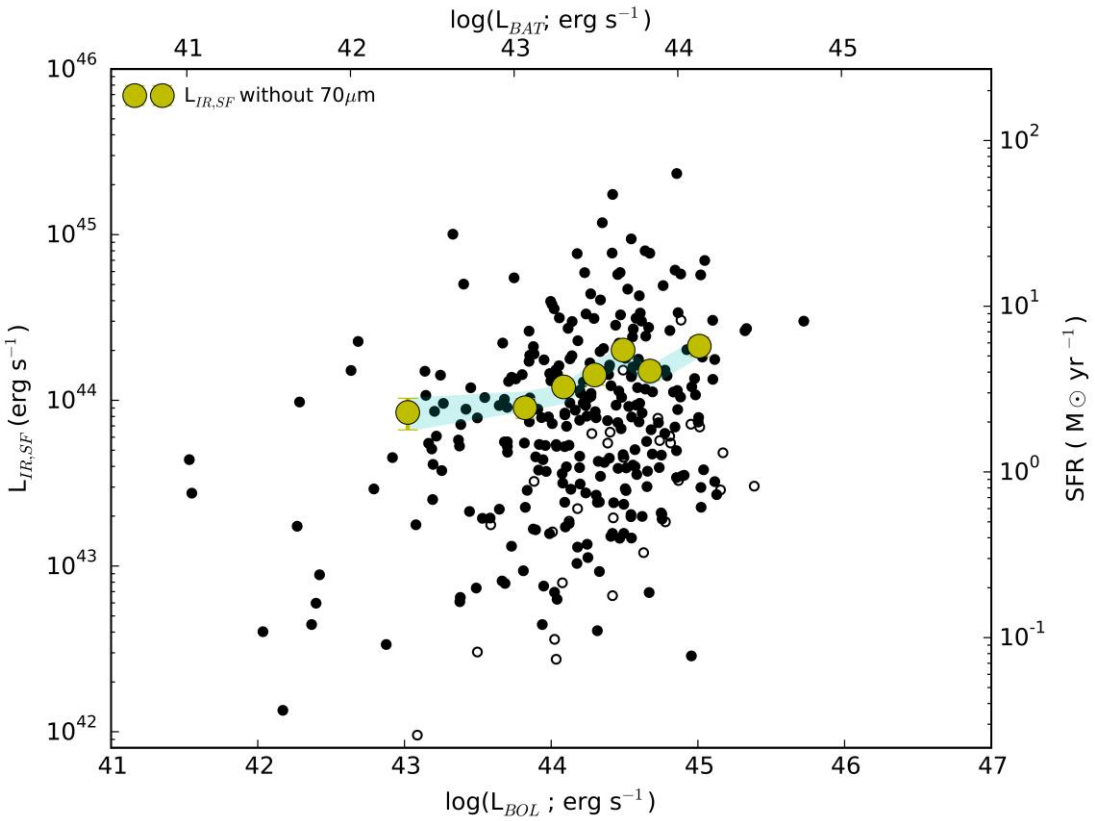

Figure 3.1: The infrared luminosity due to star formation, $L_{IR,SF}$, as a function of bolometric AGN luminosity, L_{BOL}. L_{BOL} was calculated from the hard-band (14-195 keV) X-ray luminosity, L_{BAT}, from the relation as shown in Figure 5 from Winter et al. (2012) and the star formation rate (SFR) was calculated from the $L_{IR,SF}$ using the Kennicutt (1998) relation corrected to a Chabrier IMF (Chabrier 2003). We plot the individual calculated $L_{IR,SF}$ (filled black circle), the upper limit $L_{IR,SF}$ (empty circle) and the mean infrared luminosity due to star formation $<L_{IR,SF}>$ (yellow filled circle). The number of sources that are presented in each $<L_{IR,SF}>$ bin is ≈44 which includes upper limit $L_{IR,SF}$ values. Setting the upper limit values to either the calculated (maximum) $L_{IR,SF}$ value or to zero does not change the results significantly so here we take the median of the two possible values. The errors on the $<L_{IR,SF}>$ have been quantified using a bootstrapping technique as described in Section 3.3 with results presented in Table 3. Additionally, the shaded region surrounding our main results (yellow filled circle) represents the 16th and 84th percentile of the bootstrapped distribution as our 1σ errors.

$\langle z \rangle$ (1)	$\langle L_{BAT} \rangle$ (2)	$\langle L_{BOL} \rangle$ (3)	$\langle L_{IR,SF} \rangle$ (4)	$\langle SFR \rangle$ (5)
0.008	1.09×10^{42}	1.09×10^{43}	$8.48 \times 10^{43} \pm 1.82 \times 10^{43}$	2.29 ± 0.49
0.017	1.20×10^{43}	6.82×10^{43}	$9.82 \times 10^{43} \pm 1.23 \times 10^{43}$	2.65 ± 0.33
0.021	2.05×10^{43}	1.25×10^{44}	$1.11 \times 10^{44} \pm 1.28 \times 10^{43}$	3.00 ± 0.35
0.025	3.22×10^{43}	2.06×10^{44}	$1.54 \times 10^{44} \pm 1.88 \times 10^{43}$	4.17 ± 0.51
0.032	4.78×10^{43}	3.20×10^{44}	$1.91 \times 10^{44} \pm 2.32 \times 10^{43}$	5.15 ± 0.63
0.035	6.99×10^{43}	4.89×10^{44}	$1.46 \times 10^{44} \pm 1.79 \times 10^{43}$	3.94 ± 0.48
0.037	1.48×10^{44}	1.13×10^{45}	$2.23 \times 10^{44} \pm 2.82 \times 10^{43}$	6.03 ± 0.76

Table 3.1: (1) Mean redshift of each bin. (2) Mean hard (14-195 keV) X-ray BAT luminosity (erg s^{-1}) of each bin. (3) Mean bolometric AGN luminosity (erg s^{-1}) of each bin calculated from $\langle L_{BAT} \rangle$ using the Winter et al. (2012) relation. (4) Mean infrared luminosity due to star formation (erg s^{-1}) of each bin. (5) Mean star formation rates (M_O yr^{-1}) of each bin calculated using $L_{IR,SF}$ and applying the Kennicutt (1998) relation corrected with a Chabrier IMF (Chabrier 2003). The quoted uncertainties are derived from our bootstrap method (see Section 2.3).

in this thesis the upper limits are set to a median value of the calculated (maximum) upper limit and zero.

As seen in Figure 3.1 the mean SFR appears to show a slight rise towards higher L_{BOL}. This is in agreement to many studies that take monochromatic infrared luminosities as a proxy for star formation (e.g. the $z \approx 0$ study performed by Shao et al. 2010 holds similar rise in mean SFR towards higher L_{BOL}). However, Stanley et al. (2015) show for their high-redshifted X-ray detected AGN that there is a flat relationship in the mean SFRs. While this appears to be broadly true when extended to this studies results (see Figure 3.2), this rise in mean SFRs from the *Swift*-BAT AGN sample is more pronounced than the higher redshift AGN explored by Stanley et al. (2015). In the case of taking a monochromatic luminosity as a proxy of star formation, this runs the risk of having an increasing rise in mean SFR since the AGN contribution to the infrared SED is not accounted for. However, the SED fitting procedure implemented in Section 2.3 does not run this risk since it separates out the two components. Additionally, redshift dependency can produce a bias in results if not accounted for, especially for samples with broad redshift ranges (e.g. Shao et al. 2010 has an AGN sample ranging in redshift of $0 \leq z \leq 0.3$). The results in this study are unlikely to have any such bias given the small range in redshift for this sample, i.e. $z = 0 – 0.05$.

It is widely known that AGN prefer to reside in galaxies with on-going star formation, therefore it is useful to compare AGN host galaxies to star-forming galaxies that do not host an AGN (Rosario et al. 2013b). Schreiber et al. (2015) found that massive galaxies tend to produce more star-formation than less massive galaxies (and the redshift evolution; see Mullaney et al. 2010, Harrison et al. 2012, Speagle et al. 2013) and that the star formation generally increases with redshift (up to $z \approx 4$) to form a tight correlation known as the “main sequence. Mullaney et al. (2012) showed that X-ray detected AGN trace the evolution of this main sequence. As expected, the results of Figure 3.2 trace a similar rate of growth as seen in normal star-forming galaxies in that towards higher redshifts the star formation greatly increases (Elbaz et al. 2011; Speagle et al. 2014; Schreiber et al. 2015).

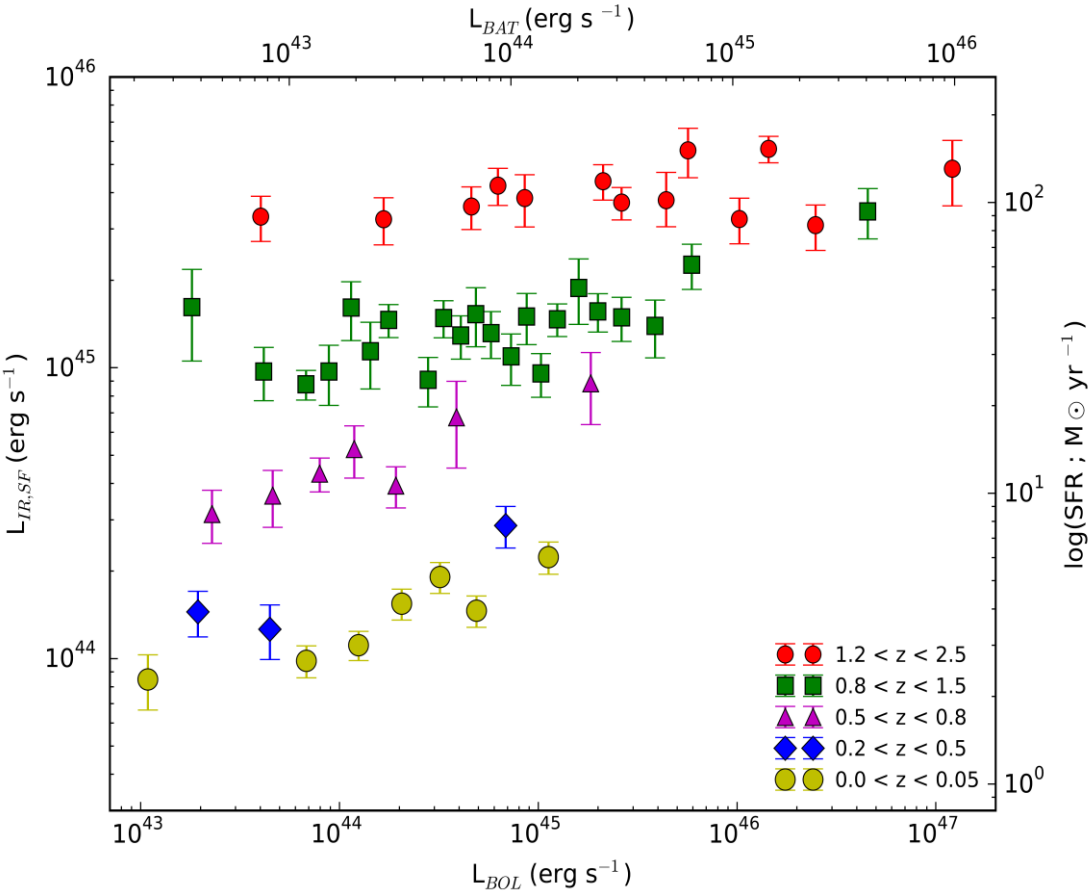

Figure 3.2: Mean infrared luminosity due to star formation, $\langle L_{IR,SF} \rangle$, as a function of bolometric AGN luminosity, L_{BOL}, across the four higher redshift ranges as originally presented in Figure 3 from Stanley et al. (2015) and our extended region ($0.0<z<0.05$) as presented in Figure 3.1 of this thesis.

The rise in mean SFRs towards higher AGN luminosity could be explained by mass effects, i.e. the more massive galaxies have larger SFRs. In order to test if stellar mass play any influence in the results here, the mean SFRs for the sample of X-ray

detected AGN are compared with that of main sequence galaxies. Before that, it is important to investigate if the binning of the AGN subset with mass estimates produces the same results as the binning of the whole AGN sample in case a bias is made. Stellar masses for each AGN are required for this purpose. I refer to Koss et al. (2011) which when cross-matched with the *Swift*-BAT AGN sample provides a total of 141 (46%) sources with mass estimates. It is found that taking bins for the mean SFRs of the mass subset as a function of L_{BOL}[1] does not greatly affect the overall results, except that there appears to be a larger scatter of mean SFR for higher L_{BOL} (see Figure 3.3). While the parent sample appears to be somewhat flatter than our mass subset the overall trend of both samples in Figure 3.3 shows that the binning of the mass subset agrees well with the binning of the whole sample. However, Figure 3.3 does not show if stellar mass has any effect on the results, therefore, to explore if the stellar mass is contributing to the rise of SFR at higher bolometric luminosities we need to first define a baseline of normal star-forming galaxies, i.e. a main sequence.

Several studies use their own definition of the main sequence, so one of the key issues in this study is which definition is the most accurate for extremely local galaxies. This issue was also addressed in Shimizu et al. (2015), for which they determined that it was best if they defined their own main sequence with a $z \approx 0$ baseline. This was because they found each definition of the main sequence is defined using different stellar mass estimates and redshift ranges that resulted in a large spread of values. Additionally, they noted that other $z \approx 0$ main sequence definitions are extrapolated from higher redshift studies (e.g. Speagle et al. 2014) therefore by creating their own main sequence they could make stronger conclusions to their results.

For low redshift ranges, Speagle et al. (2014) defined a redshift-dependent main sequence relation which agreed well for star-forming galaxies at all

[1] For this subset, the mean SFRs are measured in 7 bins of ≈ 20 AGN each.

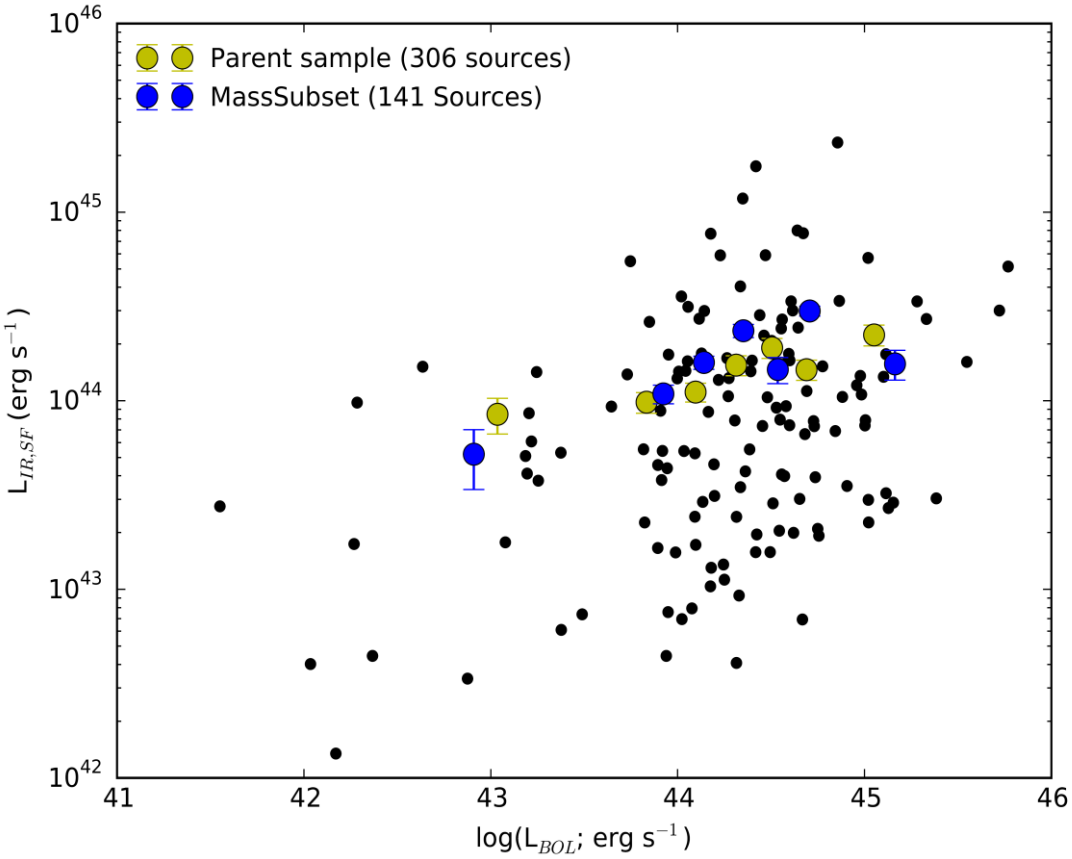

Figure 3.3: This plot is similar to Figure 3.1, except it shows the average SFR as a function of bolometric AGN luminosity using the entire parent AGN sample (yellow filled circles) and the mass subset (blue filled circles) defined by Koss et al. (2011). The individual points of the mass subset are plotted as black filled circles. This is to assess if the mass plays an integral role in the influence of the average SFR rise at higher AGN luminosities. There is no major difference between the two relationships, except for a large scatter in the mass subset.

redshifts when the low redshift and high redshift data are excluded from the fitting process. It is concluded that if using the main sequence relation from Speagle et al. (2014), the main sequence at low redshift is a best-fitted extrapolation. For this reason, Shimizu et al. (2015) defined their own mass-dependent main sequence relation by fitting a linear best-fitting slope to *Herschel* Reference Survey and the *Herschel* Stripe 82 survey (HerS) sample from Rosario et al. (2016). Shimizu states that the slope they fitted is much steeper than Speagle's main sequence relation possibly due to the addition of the less massive objects from the *Herschel* Reference Survey. As a result, Shimizu concludes that the majority of the *Swift*-BAT AGN lie inside (with 1σ scatter) or below their definition of the main sequence. A similar result is shown with this study's calculated SFRs (with mass measurements from Koss et al. 2011) if the Shimizu main sequence relation is chosen (see Figure 3.4). However, it is also interesting to note that if the Speagle et al. (2014) main sequence relation was chosen, then the majority of the subset *Swift*-BAT AGN sample would lie in (with 1σ scatter) or above the main sequence.

Another main sequence relation was defined by Schreiber et al. (2015) for redshifts up to z = 4. Despite being poorly constrained at extremely low redshifts, in their paper Schreiber et al. (2015) explains that they take infrared constraints on the main sequence of star-forming galaxies using *Herschel* and observe a steady increase in SFR with stellar mass and redshift (from z = 0.3 – 5). In Shimizu et al. (2015), they observe that the HerS AGN sample have lower SFRs than the HerS star forming galaxy sample with 48% and 78% respectively inside in the main sequence and 44% and 8% respectively below the main sequence. Shimizu et al. (2015) observe that the mass distributions for the HRS and HerS AGN samples are significantly different, and show an AGN turnover at approximately 10^{10} $M_{\odot}$. This AGN turnover appears in Figure 1 of Shimizu et al. (2015) but is not accounted for in the linear extrapolation of the main sequence relation. However, this turnover is accounted for by the Schreiber et al. (2015) relation at low redshifts (see Figure 3.4). Furthermore, Stanley et al. (2015) uses Schreiber's redshift and mass dependent main sequence relation to observe how the mean SFR of their X-ray detected AGN sample compares to normal star-forming galaxies. In order to be consistent with Stanley et al. (2015), this study will focus on using the Schreiber et al. (2015) main sequence relation.

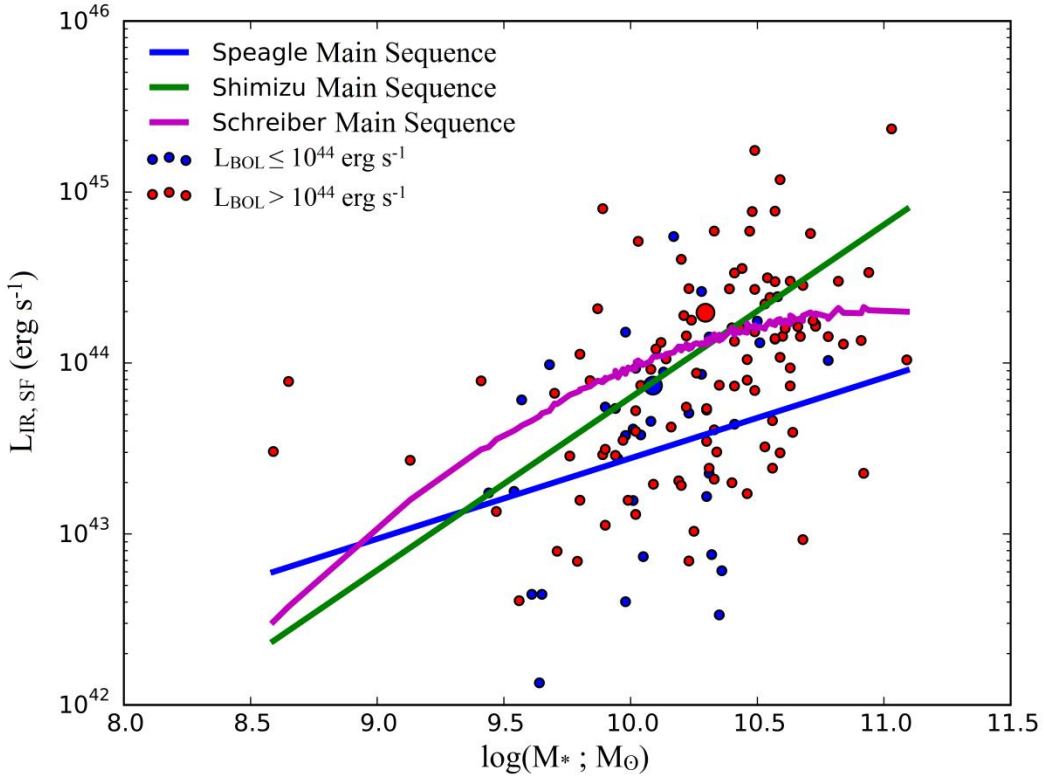

Figure 3.4: The SFR-M_* plane, indicating the variation in three main sequence relations used in this analysis. The mass subset in the top plot is split here into two groups of bolometric luminosity, $L_{Bol} \leq 10^{44}$ (blue) and $L_{Bol} > 10^{44}$ erg s^{-1} (red), with their average SFR of the whole subset presented as the larger filled squares. A large variation is seen between the relationships at high mass. The Schreiber relation is chosen in the analysis since it follows the "turnover" as seen in the *Herschel* Stripe 82 survey (HerS) sample.

Taking the Schreiber et al. (2015) main sequence relation for low redshift sources provides an interesting result in the SFR-M_* plane. The rise in mean SFR, seen in Figure 3.2, is significantly apparent at $L_{BOL} > 10^{44}$ ergs^{-1}. Therefore, it makes sense to split the mass subset of the parent AGN sample further in two bins of AGN bolometric luminosity to see whether mass is the contributing factor to the rise in mean SFR. By splitting the mass subset further into two bins of AGN bolometric luminosity, i.e. $L_{BOL} \leq 10^{44}$ erg s^{-1} and $L_{BOL} > 10^{44}$ erg s^{-1}, and determining the mean SFR of each bin, this helps to compute the distribution of SFRs and build a picture of what effects are taking place to explain the rise in mean SFR (see Figure 3.4). It can clearly be seen from Figure 3.4 that by splitting the AGN subset further into bins of bolometric luminosity show that the mean bin containing AGN with higher bolometric luminosities experience more star formation than the mean bin of AGN with low bolometric luminosities.

In Figure 3.5, the offset from the calculated SFR from SED fitting and the estimated SFR from the main sequence relation is presented as a normalised distribution. The distribution indicates that low L_{BOL} sources are more likely to lie below the main sequence, whereas the high L_{BOL} sources lie on or above the main sequence. The mean SFR for the higher range of L_{BOL} is much greater than the similar massive normal star-forming galaxies, unlike the lower range of L_{BOL} that shows the mean SFR is lower than that of similar star-forming galaxies. The results of a Kolmogorov-Smirnov (KS) test on the distribution of normalised SFRs for the two subsets of L_{BOL} (D_{KS} = 0.27, P_{KS} = 0.0295) suggests that these subsets show a moderately significant difference. Although the difference in star formation is not hugely significant it is still strong enough to cause an impact. However, in Figure 3.4 the high L_{BOL} bin appears to have enhanced star formation, possibly due to starbursts, while the low L_{BOL} bin tend to contain galaxies with lower star formation rates than that of main sequence galaxies.

Performing a KS test on the distribution of masses from the high and low L_{BOL} selection bins, instead of the normalised SFRs, results in the subsets of L_{BOL} showing a clear difference (D_{KS} = 0.38, P_{KS} = 0.00007). The difference between the samples show that mass has a clear impact on the SFR. It is generally known that more massive

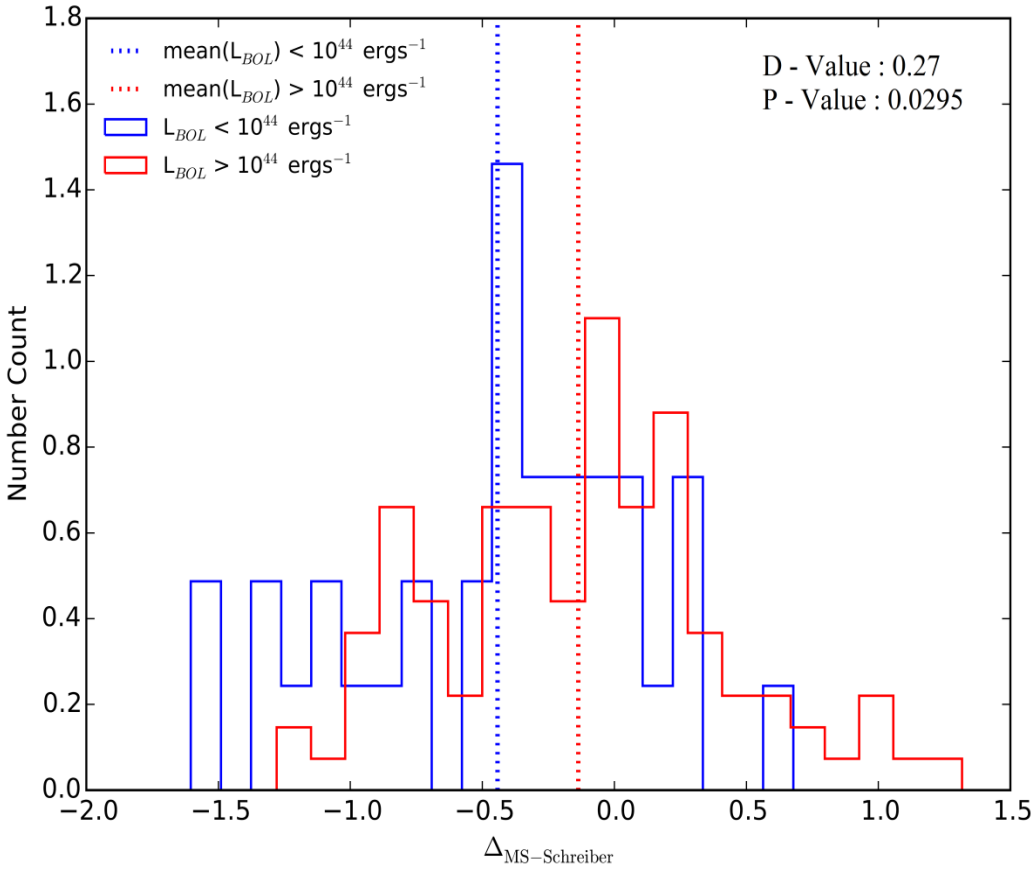

Figure 3.5: The normalised distributions of the star formation rate offsets from the Main Sequence for low (blue) and high (red) AGN luminosity subsets. This indicates that the majority of sources for both subsets lie below the Main Sequence since their average offset distributions (blue and red dotted lines) are both below zero. The results of the Kolmogorov-Smirnov test are shown in the corner with a D-value of 0.27, and P-value of 3%. Since the P-value lies under 5% (which some studies class as the maximum) the null hypothesis is rejected and this means that the main influence in the rise, as shown for high AGN luminosity in Figure 8, is not fully due to the mass. The likely reason for the rise is therefore due to the high fraction of starbursts present among the high luminosity subset.

galaxies will exhibit higher star formation, which appears to be the case for this subset of masses. However, this subset with mass estimates is only 46% of the total sample. A better way to show if the mass is clearly causing a rise in mean SFR is to have a sample where all the masses could be determined. Despite the lack of stellar masses, the results of the KS-tests shows that the increase in mean SFR is due to both mass and SFR effects, i.e. the low L_{BOL} sources are less massive and low star-forming galaxies while the high L_{BOL} sources appear to be more starbursts and more massive. Of course, this result is also dependent on the chosen main sequence relation and so there lies a possibility that low L_{BOL} sources are in fact average star-forming galaxies when choosing the Shimizu et al. (2015) main sequence relation. Further work in needed to investigate the main sequence at low redshifts and mass estimates of AGN in order to come up with a well-rounded conclusion.

3.2 Comparing the mean SFR to that of SF-galaxy population.

Stanley et al. (2015) determined that there was a flat relationship of the mean SFR and L_{BOL} for X-ray detected AGN (see Section 1.6). Hickox et al. (2014) suggested that the variability of AGN could flatten any intrinsic correlation between the mean SFR & bolometric luminosity. This was tested with the extended empirical model tracks from Aird et al. (2013) that predicts the SFR as a function of L_{BOL} on an assumed Eddington ratio distribution (see Figure 1.4). Where the black hole masses, based on Marconi & Hunt (2003), are estimated as a function of X-ray luminosity by scaling between SMBH mass and galaxy mass as $M_{BH} \approx 0.002\ M_{Bulge}$ with a fixed Eddington limit $\log(\lambda) = 0$. This redshift dependent model can predict the distribution of stellar masses by using a combination of the observed galaxy stellar mass function (Moustakas et al. 2013) and the redshift dependent probability of a galaxy hosting an AGN as a function of stellar mass. The model uses an Eddington ratio distribution as a broken power law with indices $\alpha = -0.65$ and $\alpha = -0.2$. The predicted tracks all appear intrinsically flat up to moderate luminosities for all redshift ranges ($z = 0.2 – 2.5$) in Stanley et al. (2015). The conclusion was the observed flat relationship was due to short timescale variations ($\approx 10^7$ years) in AGN luminosity, caused by changes in the mass accretion rate, which

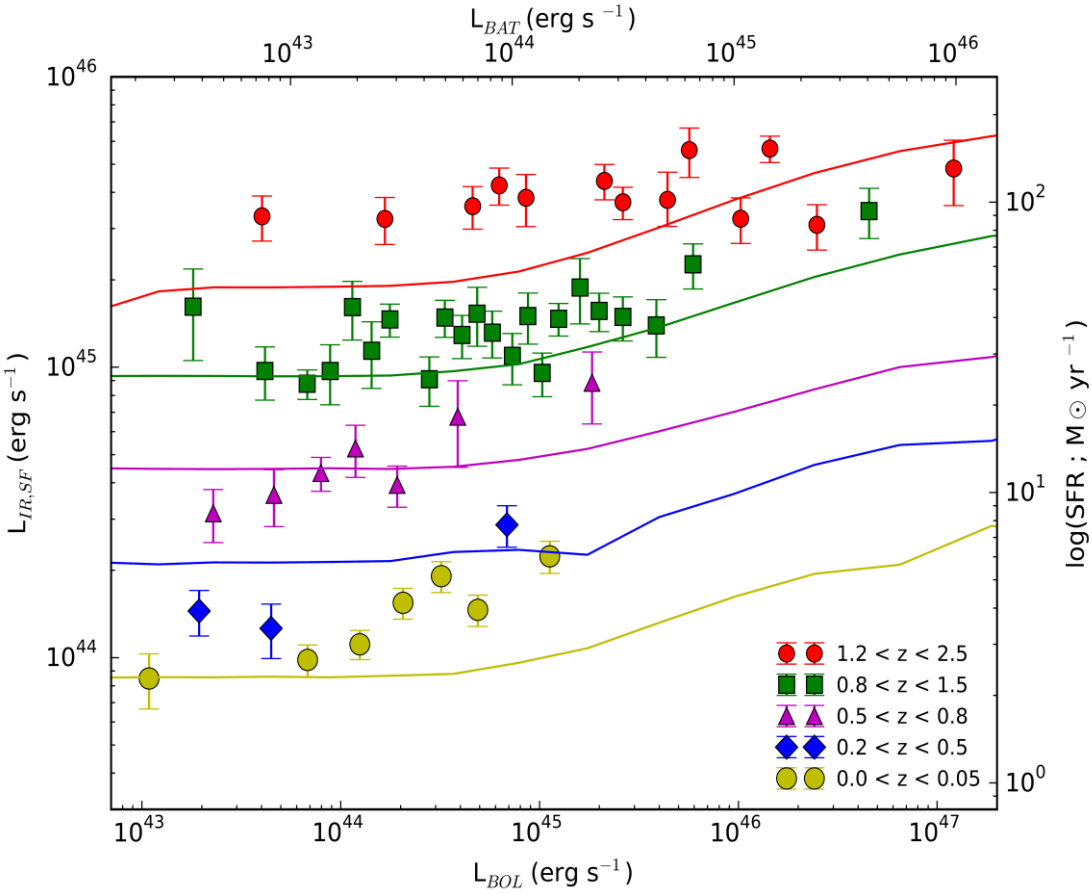

Figure 3.6: The mean infrared luminosity due to star formation as a function of the bolometric AGN luminosity in five redshift ranges with additional model tracks from the extended Aird et al. (2013) model. The redshift ranges z = 0.2-2.5 are originally defined in Figure 7(b) from Stanley et al. (2015). The additional Aird model for the redshift range z = 0 – 0.2 are presented for comparison for the *Swift*-BAT AGN sample of redshifts z = 0 - 0.05.

remove any correlations between SFR and AGN luminosity. However, for higher bolometric luminosities there appears to be a subtle rise in SFR for each of the Aird et al. (2013) tracks. This rise is being driven by an increase in stellar mass with increasing bolometric luminosity.

In Figure 3.6, I present the empirical Aird model extended for a baseline of the low redshift ranges z = 0.0-0.2. This low redshift model is based on normal main sequence galaxies at that redshift but does not take into account any starbursts. In the previous section, it was determined that the AGN at $L_{BOL} > 10^{44}$ erg s^{-1} are most likely experiencing enhanced star formation, this helps to explain the large variance between the mean SFRs and the Aird et al. (2013) model. The model itself appears to be in reasonable agreement with the results from Figure 3.1 at low AGN luminosities, but it also appears to be significantly lower towards higher luminosities. On the basis of the comparison to the Aird et al. (2013) model, the increase in mean SFRs for the most luminous X-ray AGNs in this AGN sample are most likely due to two effects: (1) an increase in the stellar mass compared to the AGN in the Aird et al. (2013) model and (2) a fraction of the AGN host galaxies are undergoing starburst activity, which is not included in the Aird et al. (2013) model.

An interesting result occurs when a slight modification is made to the Winter et al. (2012) conversion for BAT luminosity. If the correlation between the BAT luminosity and the bolometric luminosity was perfect, i.e. one-to-one, this would result in an unusually high number of starburst sources towards lower luminosities and display similar star-forming properties to AGN at redshift of $0.2 < z < 0.5$. Similarly, a poorer correlation would illustrate results of low ($z \leq 0.05$) redshift studies supporting the Aird et al. (2013) models better than previously before which would suggest less starbursts. It is also important to note that we can assume whether the Winter et al. (2012) conversion automatically applies to all the AGN in our sample when the 14-195 keV luminosity is a direct unobscured signature from the AGN (see Winter et al. 2012). This signature is much more likely to be found for AGN at lower redshifts, which can provide unbiased AGN samples for X-ray survey, than for the higher-redshifted AGN.

3.3 *Herschel* versus IRAS

The first telescope to complete an all-sky survey at infrared wavelengths was the Infrared Astronomical Satellite (IRAS). While IRAS provided an essential step in observational astronomy, it was rivalled by the Akari satellite which gave greater detail up to 200μm. At the time, quantifying star formation was a challenge as accurate photometry was required. The launch of *Herschel* has gifted astronomers another great step in observational astronomy by providing highly sensitive data up to 500μm. Understanding the far-infrared remains an important challenge.

We wish to show a comparison between taking the SED decomposition method using *Herschel* photometry and taking the monochromatic 60μm data as a proxy to star formation using IRAS photometry. This will investigate the value of modern *Herschel* photometry compared to legacy IRAS photometry in the estimation of SFRs. A study of star formation from Shao et al. (2010) involved taking the *Herschel* PACS photometry of the GOODS-N field and computing the rest frame monochromatic luminosity at 60μm as a proxy for star formation across a redshift range of $z = 0.2 – 2.5$ [2]. An additional local AGN reference sample (see Figure 6 of Shao et al. 2010) was originally presented in Lutz et al. (2010) and selected from the 39 month *Swift*-BAT catalog (Cusumano et al. 2009) with an additional selection criteria for excluding objects with galactic latitude $|b| < 15$ and objects with greater redshifts of $z > 0.3$. A total of 293 AGN used the IRAS Faint Source Catalog detections in the rest-frame 60μm were used, while Scanpi was used to get photometry for IRAS undetected sources. The luminosities of these measurements were stacked in seven bins of 2-10 keV luminosity. The study provided by Shao et al. (2010) defined a $z \approx 0$ AGN baseline of SFRs compared with the higher-redshifted AGN, which is why we compare the results of the local AGN reference sample with the *Swift*-BAT sample in Figure 3.7. This is why we question if the inclusion of highly sensitive *Herschel* photometry gives better estimations of star formation than IRAS.

[2] Even though the monochromatic far-infrared measurements are a good tracer of star formation it meets a limitation, especially in the local universe since local AGN do not have very dusty galaxies. Therefore the infrared re-emission produced will be much lower than a galaxy at higher redshifts (for a review see Lutz et al. 2014).

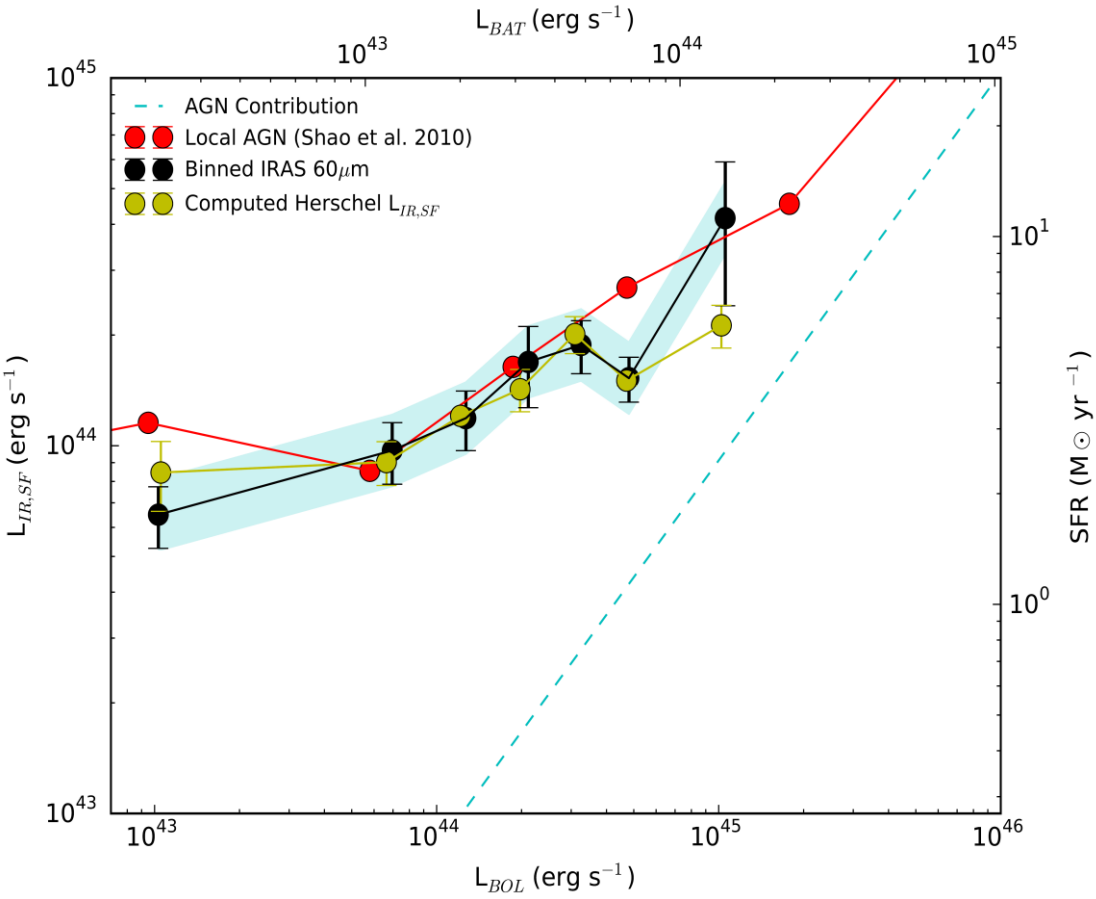

Figure 3.7: A comparison between using *Herschel* far-infrared photometry (yellow) and IRAS far-infrared photometry (black) as a proxy of star-formation. The low redshift (z = 0 - 0.3) results of X-ray detected AGN (red) defined by Shao et al. (2010) and the AGN contribution to star formation (dashed) are presented here for comparison.

In order to remain consistent with Shao et al. (2010) Figure 3.7 presents a comparison of mean SFRs computed using *Herschel* far-infrared photometry and using IRAS photometry. By cross matching the AGN sample with the IRAS database 283 sources (≈90.4% of our parent sample) have a far-infrared 60μm flux measurement. This was done by using Scanpi which can measure the fluxes of extended and faint sources. These flux estimates can then be converted into the 60μm luminosity (L_{60}) with a scaling factor of two, which corresponds to a typical Chary & Elbaz (2001) galaxy far-infrared template. This method is used as it is similar to the stacking procedure but may contain higher uncertainties. As there are a fewer number of sources from IRAS the mean SFRs are computed in smaller bins of ≈ 40 sources per bin (see Figure 3.7).

The results show that the converted 60μm luminosity from the IRAS database ($z \leq 0.05$) is relatively consistent with Shao et al. (2010) despite the samples different redshift ranges. The IRAS computed mean SFRs are similar with the mean SFRs computed using *Herschel* photometry. However, a modest upturn of SFR is present towards the higher bolometric luminosities. This result is consistent with previous studies that have taken a monochromatic rest-frame far-infrared emission as a proxy to star formation (e.g. Rosario et al. 2012). This modest upturn is likely caused by not taking into account the far-infrared contribution from the AGN activity. When accounted the mean SFRs computed by IRAS photometry appear nearly as flat as the mean SFRs computed by *Herschel* photometry. It can be noted that when investigating SFRs on galaxies hosting luminous AGN that there appears to be some differences in the results. Namely, an offset of ≈0.3 dex is seen between the IRAS and *Herschel* computed SFRs for highly luminous AGN. However, given the sensitivity and larger detection rates towards longer wavebands and X-ray luminosities, *Herschel* photometry would be the more reliable choice for estimating SFRs than IRAS photometry.

CHAPTER 4

Conclusions and Future Work

4.1 Summary of presented work

The main focus of this study is to investigate the SFRs of galaxies hosting a central AGN at redshifts up to $z \leq 0.05$. It is also to provide a $z \approx 0$ baseline in order to compare with the Stanley et al. (2015) study at higher redshifts in the range of $z = 0.2 – 2.5$. In this chapter I summarise the main results of this thesis and will discuss some of the future work that will help to address the outstanding questions from this work.

4.1.1 The SED fitting procedure, analysis and results

Chapter 2 gives a detailed view into the SED fitting procedure (based on a similar method adopted from Stanley et al. 2015) applied to *Herschel*/WISE photometry (70 - 500μm/ 3.4 - 22μm respectively) of the AGN sample. By fitting a set of empirical star-forming and AGN templates to the photometry, including upper limit constraints on photometry, this allowed the contributions of the AGN activity and star formation of the infrared SED to be constrained. This allows the SFR of each source to be computed by using equation 2.3. As explored in section 2.3, the SED fitting procedure implemented has only produced 10% upper limit values of SFR. This shows that by using highly sensitive far-infrared photometry the star formation and AGN contributions can successfully be constrained. An issue that was found was that the computed SFR was underestimated for most of the best-fitting SED solutions due to the 70μm photometry (see Figure 2.4). This was addressed by

removing the 70μm photometry from the SED fitting procedure and it was found that the average rise in SFR by implementing this was ≈ 0.2 dex.

The accuracy of the SED fitting procedures for decomposing the infrared emission into an AGN and star forming component was assessed by fixing the AGN template to the 12μm subarcsecond-resolution nuclear photometry (see Asmus et al. 2014). Since the subarcsecond 12μm data will be dominated by the AGN component, simply fixing the AGN component to this data will allow us to explore how reliable our overall SED-fitting procedure constrains the luminosity due to star formation. This is important since it determines how accurately the decomposition of the infrared emission can be constrained with sources that do not have subarcsecond-resolution nuclear photometry, which is ≈ 74.4% of the AGN sample. The result, shown in Figure 2.5, found that the SED fitting procedure is a robust method of decomposing the AGN activity and star formation with most of the subsample (95%) with nuclear photometry (≈ 80 sources) providing similar SFRs and only a couple of sources with an average difference of 0.2 dex.

In previous literature mid-infrared colours have been used to determine the amount of dust heated by the AGN and apply some colour selections for selecting AGN dominated systems (e.g., Stern et al. 2005; Lacy et al. 2007; Mateos et al. 2012). The Mateos et al. (2012) AGN wedge has provided an effective way of selecting AGN dominated systems from star-forming galaxies using mid-infrared colours. Here, I test the reliability of the Mateos et al. (2012) AGN wedge by applying it with the ultra-hard (14 – 195 keV) X-ray detected *Swift*-BAT AGN. Similarly to what was found in Mateos et al. (2012), the *Swift*-BAT AGN appears to be relatively bright at mid-infrared wavelengths, with the majority of AGN at X-ray luminosities greater than $10^{43.5}$ erg s $^{-1}$ (i.e. 54% and 85% for $L_{BAT} = 10^{43.5\text{-}44}$ and $> 10^{44}$ erg s^{-1} respectively; see Table 2.4) lying inside the selection wedge. Additionally, from the results of the SED fitting, most AGN (>85%) with a fractional dominance greater than 50% lie in the selection wedge which agrees well with Mateos et al. (2012) analysis in that more dominating AGN galaxies (>50% fractional dominance) lie within the selection wedge.

I extended these analyses by also including sensitive *Herschel* photometry to define a new and broader mid-to-far-infrared colour selection. I found that the most

robust mid-to-far-infrared colour selection was the S_{160}/ S_{12} since it is able to distinguish a clear separation of AGN activity and star formation (see Figure 2.7b; Figure 2.8b). The separation that is clearly apparent in Figure 2.8b of star-forming SEDs and AGN SEDs indicates the reliability of both the Mateos et al. (2012) AGN wedge and the SED fitting procedure used in this analysis.

4.1.2 Results and discussions of the mean SFR for local Active Galactic Nuclei

In Chapter 3, I studied the computed SFRs from the best-fitting SED solutions of Chapter 2. By computing the mean SFRs as a function of bolometric AGN luminosity (see Figure 3.1), the results were broadly consistent with the study performed by Stanley et al. (2015), in that the low redshifted AGN sample produced mean SFRs lower than similar luminous AGN at higher redshifts (see Figure 3.2). Previous literature has found that the mean SFRs of AGN samples as a function of bolometric luminosity can have an increasing (e.g., Lutz et al. 2010; Shao et al. 2010), or decreasing (e.g., Page et al. 2012) or a flat relationship (e.g., Stanley et al. 2015) at higher luminosities ($L_{BOL} > 10^{44}$ erg s^{-1}). The results of this thesis are consistent with previous studies where no connection exists between the mean SFRs and low bolometric luminosities (i.e. a flat relationship; $L_{Bol} \leq 10^{44}$ erg s^{-1}).

However, a slight rise in mean SFRs is observed towards higher luminosities in this study. This rise is similarly observed in the study by Shao et al. (2010) which calculated mean SFRs of local AGN by using monochromatic flux measurements from *Herschel* (see Figure 3.7). It is found that the rise observed in Shao et al. (2010) was most likely a result of not taking into account any of the AGN emission. The SED method explored in Chapter 2 has already accounted for this emission though, therefore, in order to account for the slight rise in mean SFR of this study there must be other factors that have not been accounted for (e.g. mass effects).

To investigate if mass effects are influencing this rise in mean SFR, I refer to Koss et al. (2011) which provides stellar mass estimates for some (46%) of the *Swift*-BAT AGN sample up to redshift $z \leq 0.05$. Using the Schreiber et al. (2015) main

sequence relation to calculate the offset between the mean SFRs and the SFRs of similarly massive galaxies, it is found that the rise in mean SFR towards higher bolometric luminosities is a result of higher fractions of galaxies appearing as starbursts in the higher AGN luminosity range but equally a higher fraction of quiescent galaxies in the lower AGN luminosity range (see Figure 3.4 and 3.5).

Additionally, as presented in Stanley et al. (2015), the extended empirical evolutionary track (based on Aird et al. 2013) for the low redshift range $0 \leq z \leq 0.2$ was plotted with the main results (see Figure 3.6). This model provides the mean SFR as a function of bolometric AGN luminosity from predicted stellar masses around the main sequence relation. The predictive tracks all appear intrinsically flat up to moderate luminosities, possibly caused by short timescale variations in the AGN luminosity. Towards higher luminosities (i.e. $L_{BOL} > 10^{45}$ erg s^{-1}) a rise in SFR is observed which could be being driven by small increases in mass for galaxies hosting luminous AGN. Broadly speaking the Aird et al. (2013) model does not agree well with the results. As seen in Figure 3.6, the results do not appear as intrinsically flat as those in the Stanley et al. (2015) study. A clear enhancement in mean SFR is witnessed for the results of this study when compared to the Aird et al. (2013) model. It was determined earlier that most of the AGN sample is hosting galaxies that appear to be more like starburst galaxies. This difference is aided by the Aird et al. (2013) model since it does not take starburst galaxies into account.

In Section 3.3, the mean SFRs obtained by fitting *Herschel* photometry are compared with the mean SFRs computed using IRAS photometry to explore the reliability of using IRAS data. Comparing the results from scaling far-infrared photometry from IRAS (scaling adopted from Rosario et al. 2013a) as a value of SFR with the main results of this thesis (see Figure 3.7) it is apparent that the two results are broadly consistent. Except at higher bolometric luminosities where the mean SFR computed with IRAS photometry are systematically higher ($\approx$ 0.4 dex) due to not taking into account the contribution of the AGN activity by scaling a monochromatic luminosity. Accounting for AGN activity leads to a “flatter” relationship, however, the higher sensitivity gives *Herschel* the advantage to provide the best estimates of SFR than IRAS.

4.2 Future work

The work presented in this thesis has extended the study performed by Stanley et al. (2015) to a redshift baseline of $z \approx 0$, which aimed to understand the relationship between star formation and AGN luminosity. It has now resulted in an outstanding question. In this section, this is outlined.

Following the discussion from Section 3.1 where I assess which of the three main sequence relations (Speagle et al. 2014; Schreiber et al. 2015; Shimizu et al. 2015) should be used in this study's analyses, there does not exist a well-defined main sequence relation for low redshift galaxies. Many studies that use a low redshifted main sequence extrapolate this via a higher redshifted main sequence relation. Shimizu et al. (2015) has defined their own main sequence relation for the purpose of identifying where local AGN lie on the SFR-M_* plane.

However, the relation made from the HerS sample in Shimizu et al. (2015) is entirely dependent on a linear extrapolation, which can be avoided if the range in stellar masses is increased. In this study, I find that this linear extrapolation does not fairly represent the AGN population witnessed in Shimizu et al. (2010). The AGN population in this case provides a "turnover" at approximately 10^{10} $M_\odot$ between the HRS and HerS AGN samples. While this turnover is broadly accounted for by using the low redshifted extrapolation of the Schreiber et al. (2015) main sequence relation, this relation was not observed at such low redshifts. Therefore, a new model of the main sequence at low redshifts is needed to reproduce the observed trends of local galaxies. However, this can remain a challenge, especially when observing at far-infrared wavebands since galaxies at such low redshifts do not possess a large amount of freely available gas to form many stars.

Bibliography

Aird J. et al., 2013, ApJ, 775, 41

Alexander, D. M., Bauer, F. E., Chapman, S. C., et al. 2005, ApJ, 632, 736

Alexander, D. M., Chary, R.-R., Pope, A., et al. 2008, ApJ, 687, 835

Antonucci, R., 1993, ARAA, 31, 473

Asmus, D., Hönig, S. F., Gandhi, P., et al. 2014, MNRAS, 439, 1648

Barthelmy, S. D., Chincarini, G., Burrows, D. N., et al. 2005, Nature, 438, 994

Baumgartner, W. H., Tueller, J., Markwardt, C. B., et al. 2013, APJS, 207, 19

Bianchi, S., Maiolino, R., and Risaliti, G., 2012, ArXiv E-Prints: 1201.2119

Brandt, W. N., Alexander, D. M., 2015, A&A, Rev 23, 1

Calzetti, D., Wu, S.-Y., Hong, S., et al. 2010, ApJ, 714, 1256

Chabrier, G. 2003, PASP, 115, 763

Chary, R., & Elbaz, D. 2001, ApJ, 556, 562

Cohen, J. G., 2003, ApJ, 598, 288

Comastri, A., Gilli, R., Marconi, A., et al. 2015, A&A, 574, L10

Cusumano, G., La Parola, V., Segreto, A., et al. 2010, A&A, 524, A64

Dale, D. A., & Helou, G. 2002, ApJ, 576, 159

Del Moro, A., Alexander, D. M., Mullaney, J. R., et al. 2013, A&A, 549, A59

Delvecchio, I., Gruppioni, C., Pozzi, F., et al. 2014, MNRAS, 439, 2736

Domínguez Sánchez, H., Bongiovanni, A., Lara-López, M. A., et al. 2014, MNRAS, 441, 2

Einstein, A. Annals of Mathematics Vol. 40, No.4

Elbaz, D., Dickinson, M., Hwang, H. S., et al. 2011, A&A, 533, A119

Elvis, M., Maccacaro, T., Wilson, A. S., et al. 1978, MNRAS, 183, 129

Elvis, M., Wilkes, B. J., McDowell, J. C., et al. 1994, APJS, 95, 1

Fath, E. A. 1909, Lick Observatory Bulletin, 5, 71

Fritz, J., Franceschini, A., & Hatziminaoglou, E. 2006, MNRAS, 366, 767

Gabor, J. M., Capelo, P. R., Volonteri, M., et al. 2016, A&A, 592, A62

Gehrels, N., Chincarini, G., Giommi, P., et al. 2004, ApJ, 611, 1005

Ghez, A. M., Salim, S., Weinberg, N.N., et al., 2008, ArXiv E-Prints: 0808.2870

Gilfanov, M. & Merloni, A. Space Sci Rev, 2014, 183: 121.

Gillessen, S., Eisenhauer, F., Fritz, T. K., et al., 2009, ArXiv E-Prints: 0910.3069

Griffin, M. J., Abergel, A., Abreu, A., et al. 2010, A&A, 518, L3

Harrison, C. M., 2016, Springer Theses, "Observational Constraints on the Influence of Active Galactic Nuclei on the Evolution of Galaxies"

Harrison, C. M., Alexander, D. M., Mullaney, J. R., et al. 2012, ApJL, 760, L15

Heinicke, C. & Hehl, F. W., 2015, ArXiv E-Prints: 1503.02172v1

Hickox, R. C., Mullaney, J. R., Alexander, D. M., et al. 2014, ApJ, 782, 9

Hubble, E. P. 1925, Popular Astronomy, 33, 252

Ishibashi, W. & Fabian, A. C., 2012, MNRAS, 427, 2998

Kauffmann, G., Heckman, T. M., Tremonti, C., et al. 2003, MNRAS, 346, 1055

Kennicutt, Jr., R. C. 1998, ARAA, 36, 189

King, A. 2008, New Astron. Rev., 52, 253

Kormendy, J., J. Beckman, L. Colina, & H. Netzer, 1993, (Madrid: Consejo Superior de Investigaciones Científicas), 197

Kormendy, J., & Ho, L. C. 2013, ARAA, 51, 511

Koss, M., Mushotzky, R., Veilleux, S., et al. 2011, ApJ, 739, 57

Lacy, M., Storrie-Lombardi, L. J., Sajina, A., et al. 2004, ArXiv E-Prints: 0405604

LaMassa, S. M., Urry, C. M, Glikman, E., et al. 2012, ArXiv E-Prints:

Li, A. 2007, ASPC, 373, 561

Low, F. J., & Kleinmann, D. E. 1968, AJ, 73, 868

Lutz, D., Mainieri, V., Rafferty, D., et al. 2010, ApJ, 712, 1287

Lutz, D. 2014, ARAA, 52, 373

Lynden-Bell, D. 1969, Nature, 223, 690

Magorrian, J., Tremaine, S., Richstone, D., et al. 1998, AJ, 115, 2285

Marconi, A., & Hunt, L. K. 2003, ApJL, 589, L21

Mateos, S., Alonso-Herrero, A., Carrera, F. J., et al. 2012, MNRAS, 426, 3271

Mathur, S., Fields, D., Peterson, B. M., and Grupe, D., 2012, ArXiv E-Prints: 1102.0537

McCarthy, I. G., Schaye, J., Bower, R. G., et al. 2011, MNRAS, 412, 1965

Meléndez, M., Mushotzky, R. F., Shimizu, T. T., et al. 2014, ArXiv E-Prints: 1408.5889v1

Moustakas, J., Coil, A. L., Aird, J., et al. 2013, ApJ, 767, 50

Mullaney, J. R., Ward, M. J., Done, C., et al. 2009, MNRAS, 394, L16

Mullaney, J. R., Alexander, D. M., Goulding, A. D., & Hickox, R. C. 2011, MNRAS, 414, 1082

Mullaney, J. R., Daddi, E., Béthermin, M., et al. 2012, ApJ, 753, L30

Netzer, H., 2015, ArXiv E-Prints: 1505.00811

Neugebauer, G., Habing, H. J., van Duinen, R., et al. 1984, ApJ, 278, L1

Orosz, J. A., McClintock, J. E., Aufdenberg, J. P., et al. 2011, ApJ, 742, 84

Osterbrock, D.E., 1981, ApJ, 249, 462

Page, M. J., Symeonidis, M., Vieira, J. D., et al. 2012, Nature, 485, 213

Peterson, B. M., 1997, Cambridge University Press, An Introduction to Active Galactic Nuclei.

Poglitsch, A., Waelkens, C., Geis, N., et al. 2010, A&A, 518, L2

Polletta, M. Courvoisier, T. J.-L., Hooper, E. J., Wilkes, B. J., 2000, A&A, 362, 75

Ramos Almeida, C., Rodriguez Espinosa, J. M., Barro, G., et al. 2009, AJ, 137, 179

Richards, G. T., Lacy, M., Storrie-Lombardi, L. J., et al. 2006, ApJS, 166, 470

Rosario, D. J., Santini, P., Lutz, D., et al. 2012, A&A, 545, A45

Rosario, D. J., Trakhtenbrot, B., Lutz, D., et al. 2013a, A&A, 560, A72

Rosario, D. J., Lutz, D., and PEP Consortium, 2013b, ArXiv E-Prints: 1309.3569

Rosario, D.J., Mendel, J. T., Ellison, S. L., et al. 2016, MNRAS, 457, 2703

Salpeter, E. E., 1964, ApJ, 120, 796

Schartmann, M., Meisenheimer, K., Camenzind, M., et al. 2008, A&A, 482, 67

Schmidt, M. 1963, Nature, 197, 1040

Schödel, R., Merritt, D., Eckart, A., 2009, A&A, 502, 91

Schreiber, C., Pannella, M., Elbaz, D., et al. 2015, A&A, 575, A74

Schwarz, G. 1978, The Annals of Statistics, 6, 461

Seyfert, C. K. 1943, ApJ, 97, 28

Shakura, N. I., Sunyaev, R. A., 1973, A&A, 24, 337

Shao, L., Lutz, D., Nordon, R., et al. 2010, A&A, 518, L26

Shimizu, T. T., Mushotzky, R. F., Meléndez, M., Koss, M., & Rosario, D. J. 2015, MNRAS, 452, 1841

Silva, L., Granato, G. L., Bressan, A., & Danese, L. 1998, ApJ, 509, 103

Speagle, J. S., Steinhardt, C. L., Capak, P. L., & Silverman, J. D. 2014, APJS, 214, 15

Stanley, F., Harrison, C. M., Alexander, D. M., et al. 2015, MNRAS, 453, 591

Stern, D., Einsenhardt, P., Goujian, V., et al., 2005, ApJ, 631, 163

Stern, D., Assef, R. J., Benford, D. J., et al. 2012, ApJ, 753, 30

Treister, E., Schawinski, K., Volonteri, M., and Natarajan, P., 2013, ArXiv E-Prints: 1310.2249

Treister, E., Urry, C. M., Chatzichristou, E., et al 2004, ArXiv E-Prints: 0408099

Treister, E., Virani, S., Gawiser, E., et al. 2008, ArXiv E-Prints: 0810.3917v2

Trichas, M., Green, P. J., Silverman, J. D., et al. 2013, ArXiv E-Prints: 1204.5148

Urry, C. M., & Padovani, P. 1995, PASP, 107, 803

Volonteri, M., 2010, ArXiv E-Prints: 1003.4404

Wilson, A. S., Colbert, E. J. M., 1994, ArXiv E-Prints: 9408005

Winter, L. M., Veilleux, S., McKernan, B., Kallman, T. R., 2012, ApJ, 745, 107

Wright, E. L., Eisenhardt, P. R. M., Mainzer, A. K., et al. 2010, AJ, 140, 1868

Zamorani, G., Henry, I. P., Maccacaro, T., et al. 1981, ApJ, 245, 357

Appendix A

Spectral Energy Distributions of Swift-BAT AGN

Chapter 2 gives an overview of the SED fitting procedure and decomposition method used to disentangle the AGN and the star formation contributions effectively from the overall SED. The mid-infrared (12 and 22 μm) and far-infrared (70 – 500 μm) photometry are obtained from the WISE database and *Herschel* Observations respectively. Using a similar method presented in Stanley et al. (2015), the photometry is fitted by using 7 star-forming galaxy templates (defined by Silva et al 1998; Dale & Helou 2002; Mullaney et al 2011) and an AGN template (Mullaney et al 2011) in order to assess the SED contributions from the AGN and star formation. This is only the case for when there are three or more photometric detections, otherwise an upper limit on both contributions are fitted. After performing a total of 14 SED fits (seven star-forming only fits and seven combined star-forming and AGN fits), the best-fitting SED solution is defined by the smallest BIC value (see section 3.3). If any other SED solutions have a BIC value within $\Delta_{BIC} \leq 2$ of the best-fitting SED solution BIC value, then these other SED solutions are considered as equally good fits. When this occurs an average of these best-fitting SED solutions is made. After determining the best-fitted SED solution, the integrated 8-1000 μm infrared luminosity due to star formation, $L_{IR,SF}$ and the infrared luminosity due to AGN, $L_{IR,\,AGN}$, can be computed.

Each of the plotted best-fitted SED solutions follows this criteria: the photometric 5σ detections (black filled circles) and the upper limit photometry (unfilled circle with arrow) cover the wavelength range 12 - 500 μm (with exception to the 70 μm which is plotted as grey filled circles); the extra WISE photometry (blue filled circles) cover the wavelengths 3.4 and 4.6 μm; 5σ errors on each of the photometry are provided, unless an upper limit on photometry is provided; subarcsecond resolution photometry (12 and 18 μm) provided by Asmus et al. (2014) is plotted as red filled circles with errors; AGN template is plotted as dashed grey line;

star-forming template is plotted as dot-dashed grey line; best fitted (combination of the AGN and star-forming templates) is plotted as thick black line.

The resulting best-fitted SED solutions are presented in this appendix in alphabetical order. We provide a number of information for each SED: the redshift value; the $L_{IR,SF}$ value, the BAT luminosity, L_{BAT} ; an upper limit value; a flag number; in-wedge value; the star-forming template index. The redshift and L_{BAT} were provided in the studies by Melendez et al. (2014) and Shimizu et al. (2015). The upper limit value indicates if the best-fitted SED solution has placed an upper limit constraint due to lack of photometry: 0 means no upper limit was placed; 1 means an upper limit was placed. The flag number is a crucial part of the SED fitting procedure since it determines if an AGN template or a star-forming template or both templates were used to describe the best fit. Flag 6 indicates that an AGN and star-forming template are the best fit; Flag 5 indicates that the star-forming template only is the best fit; Flag 2 and 3 mean that an upper limit was placed on the star-forming and AGN templates. The In-wedge value indicates if the source lies inside the Mateos et al. (2012) wedge: 0 means the source does not lie inside the wedge; 1 means the source does lie inside the wedge. This result is interesting since we use it in Section 3.6 to assess how reliable this wedge is and how many of our sources used only a star-forming template. We have also provided the star-forming template index. If only one value in the index is 1 then a specific template is used to provide the best-fitting SED solution. If multiple values in this index are 1 then these templates selected are equally good SED solutions, therefore an average best fit is made given the large variability in our star-forming templates. The templates used can be seen in Figure 2.2 and the star-forming template index is given as:

[SB1, SB2, SB3, SB4, SB5, ARP220, D&H2002]

For example, the source MRK18 (see Figure A.1) has an index of [0 0 0 0 0 1 0] and a flag value of 6. This indicates that the best-fitting SED solution has a successfully identified the contribution from the AGN and star-forming components where the template selected was the ARP220 from Silva et al (1998).

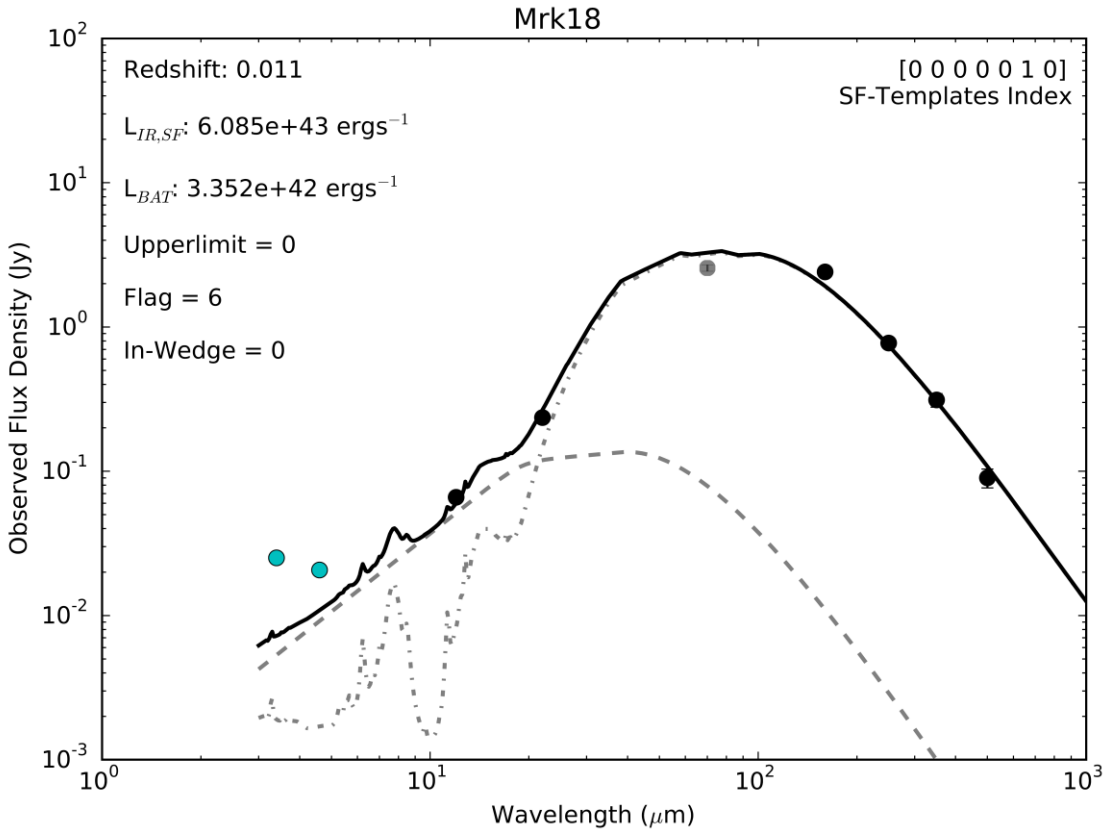

Figure A.1: SED solution for *Swift*-BAT source MRK18

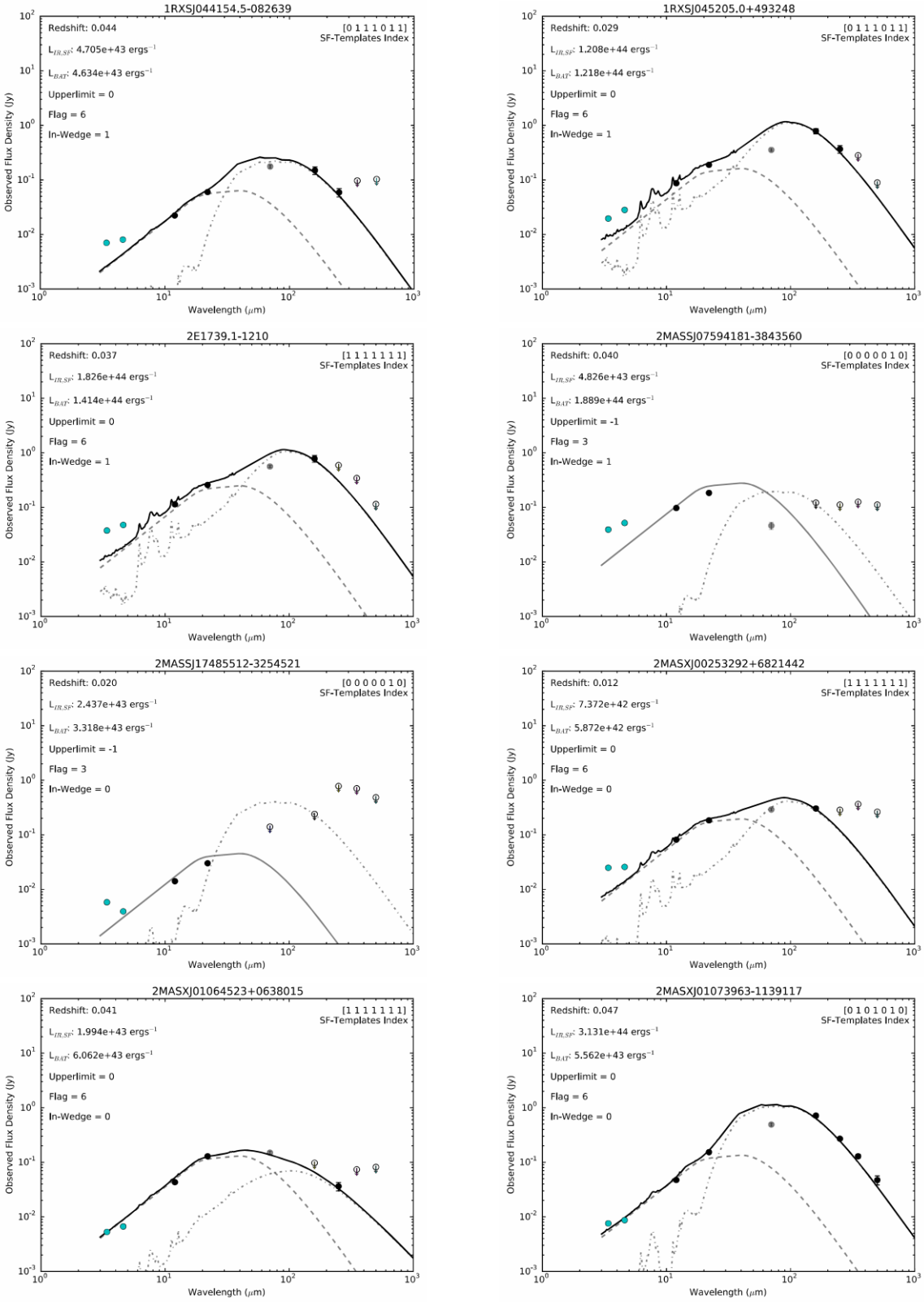

Figure A.2: Best-fitted SED solutions for eight Swift-BAT sources (listed alphabetically).

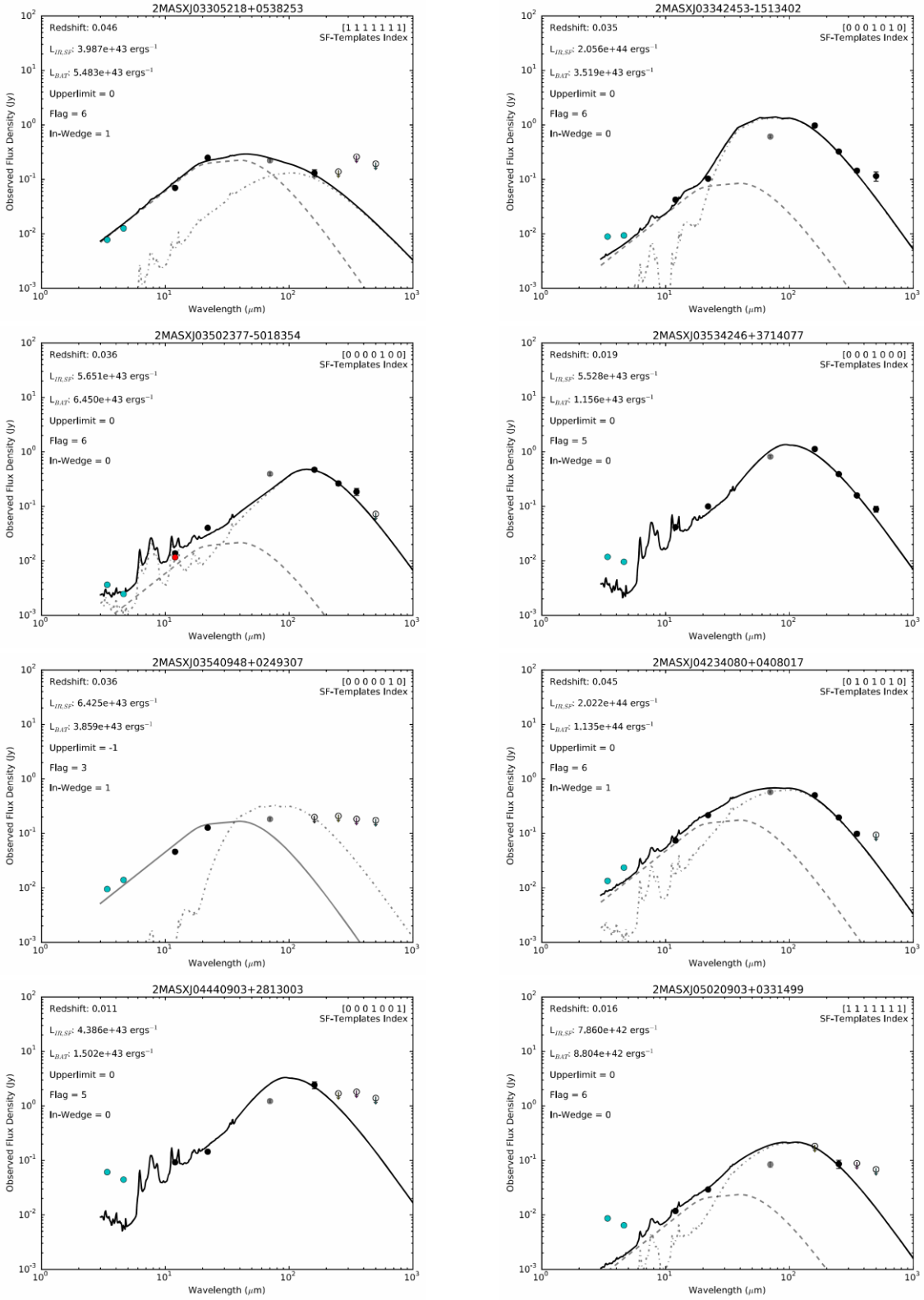

Figure A.3: Continued from Figure A.2, best-fitted SED solutions for eight Swift-BAT sources (listed alphabetically).

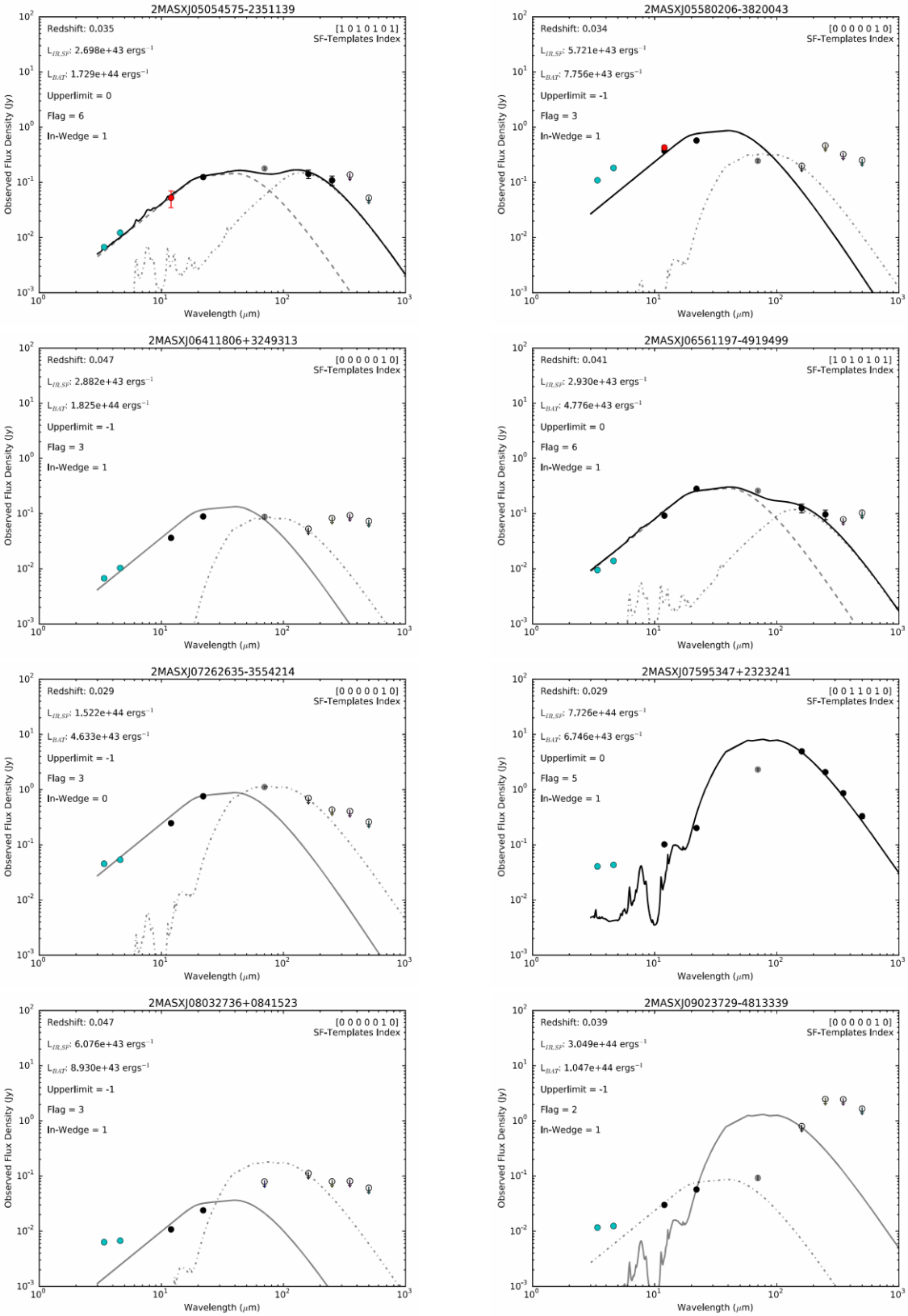

Figure A.4: Continued from Figure A.2, best-fitted SED solutions for eight Swift-BAT sources (listed alphabetically).

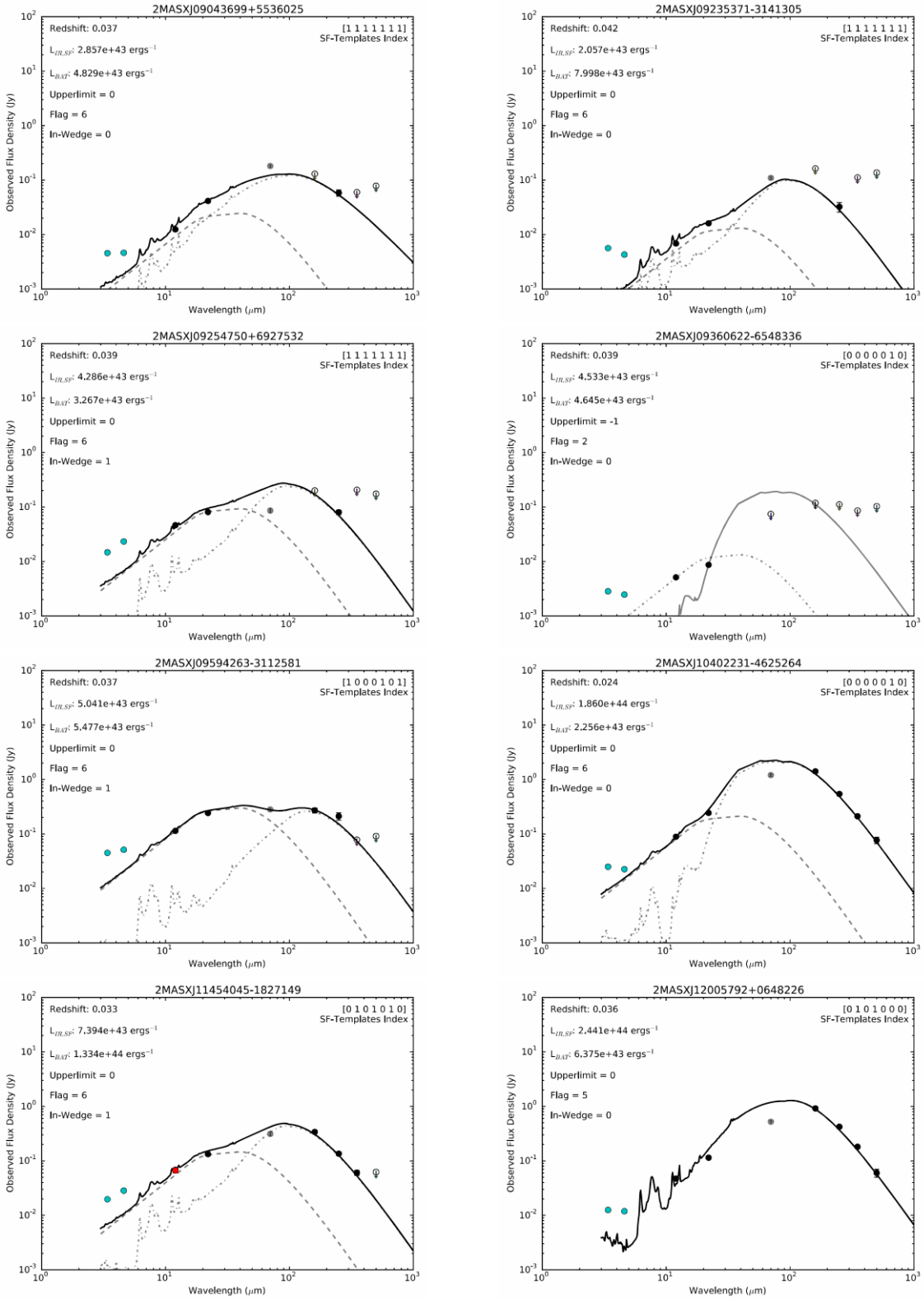

Figure A.5: Continued from Figure A.2, best-fitted SED solutions for eight Swift-BAT sources (listed alphabetically).

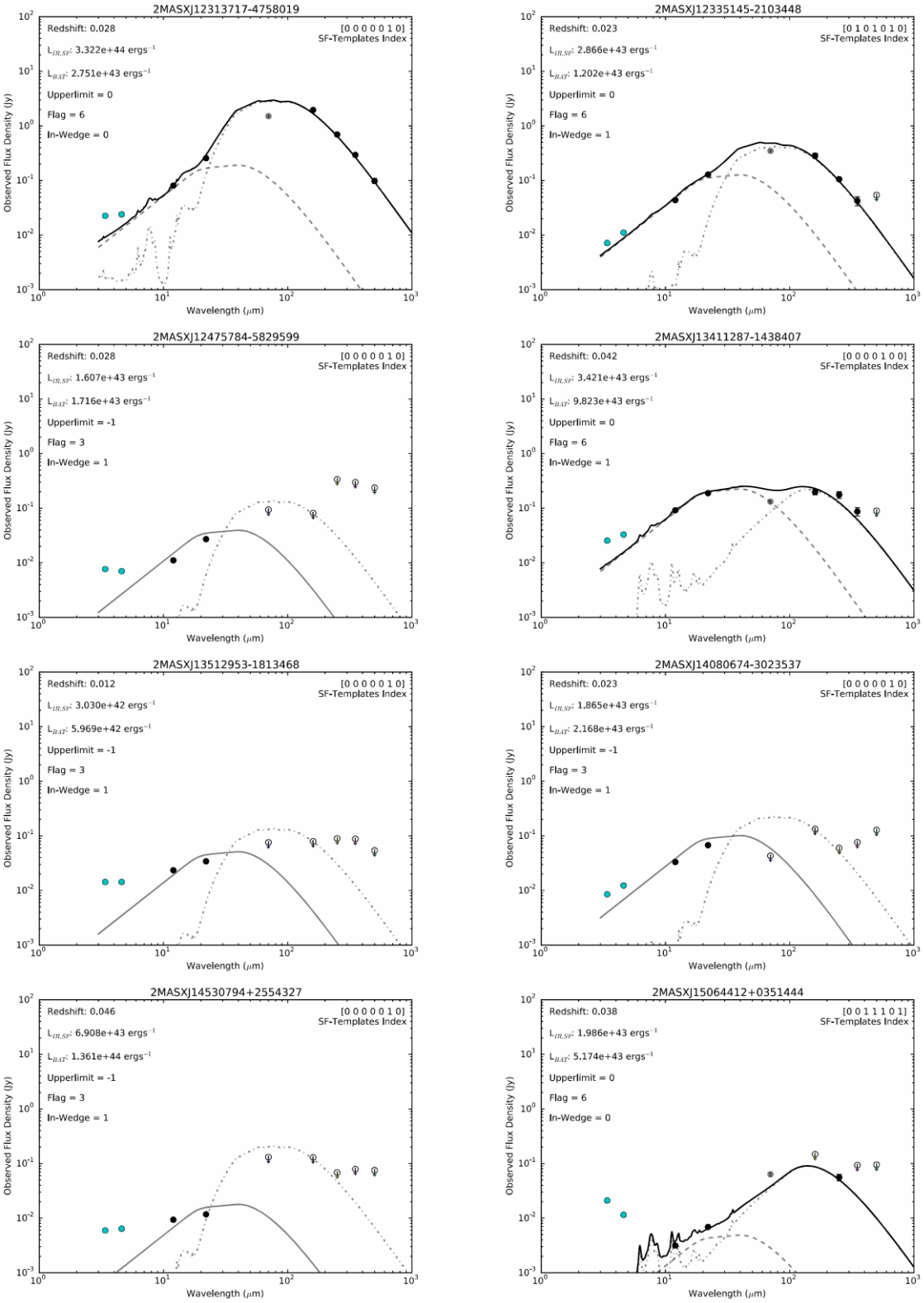

Figure A.6: Continued from Figure A.2, Best-fitted SED solutions for eight Swift-BAT sources (listed alphabetically).

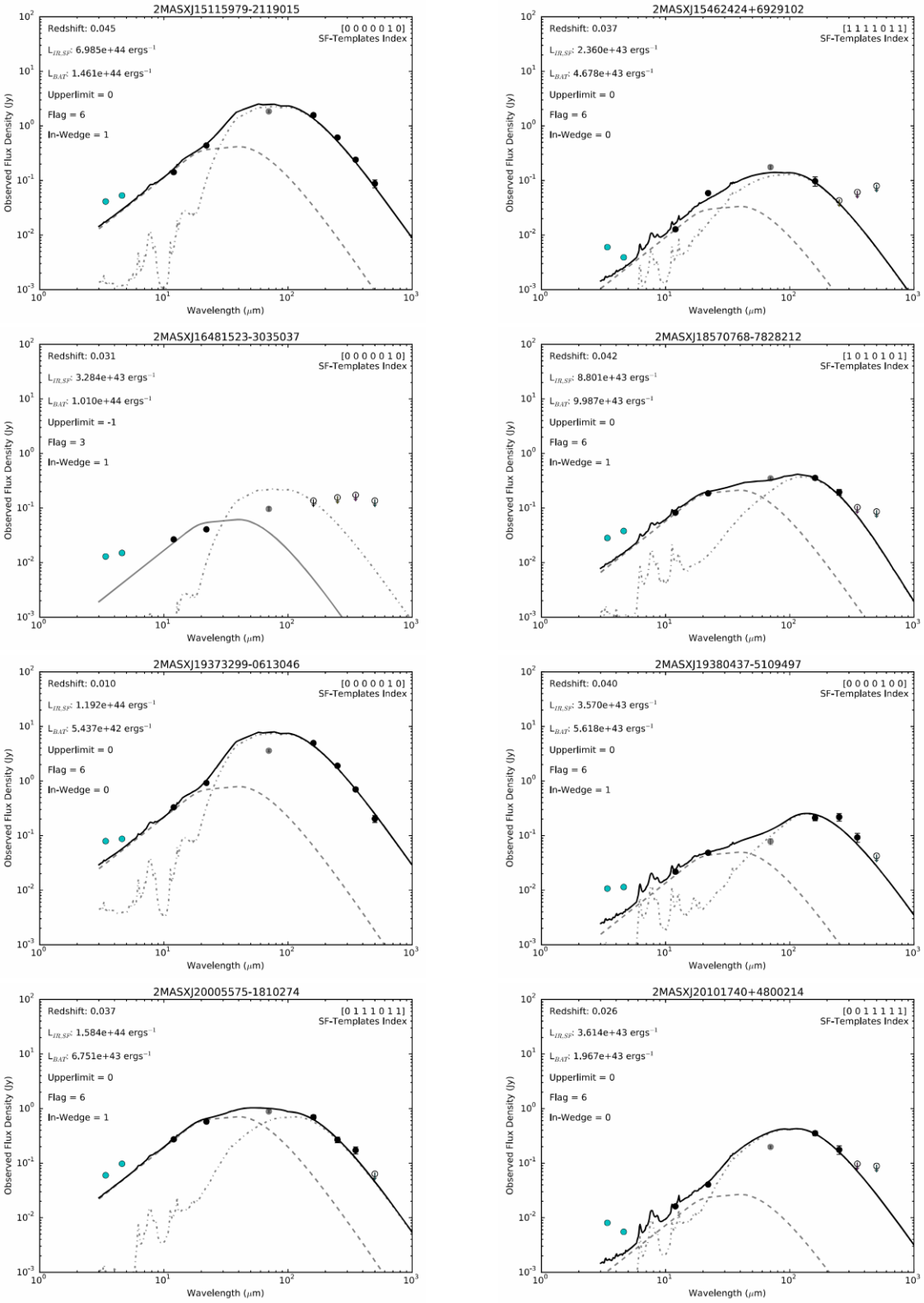

Figure A.7: Continued from Figure A.2, Best-fitted SED solutions for eight Swift-BAT sources (listed alphabetically).

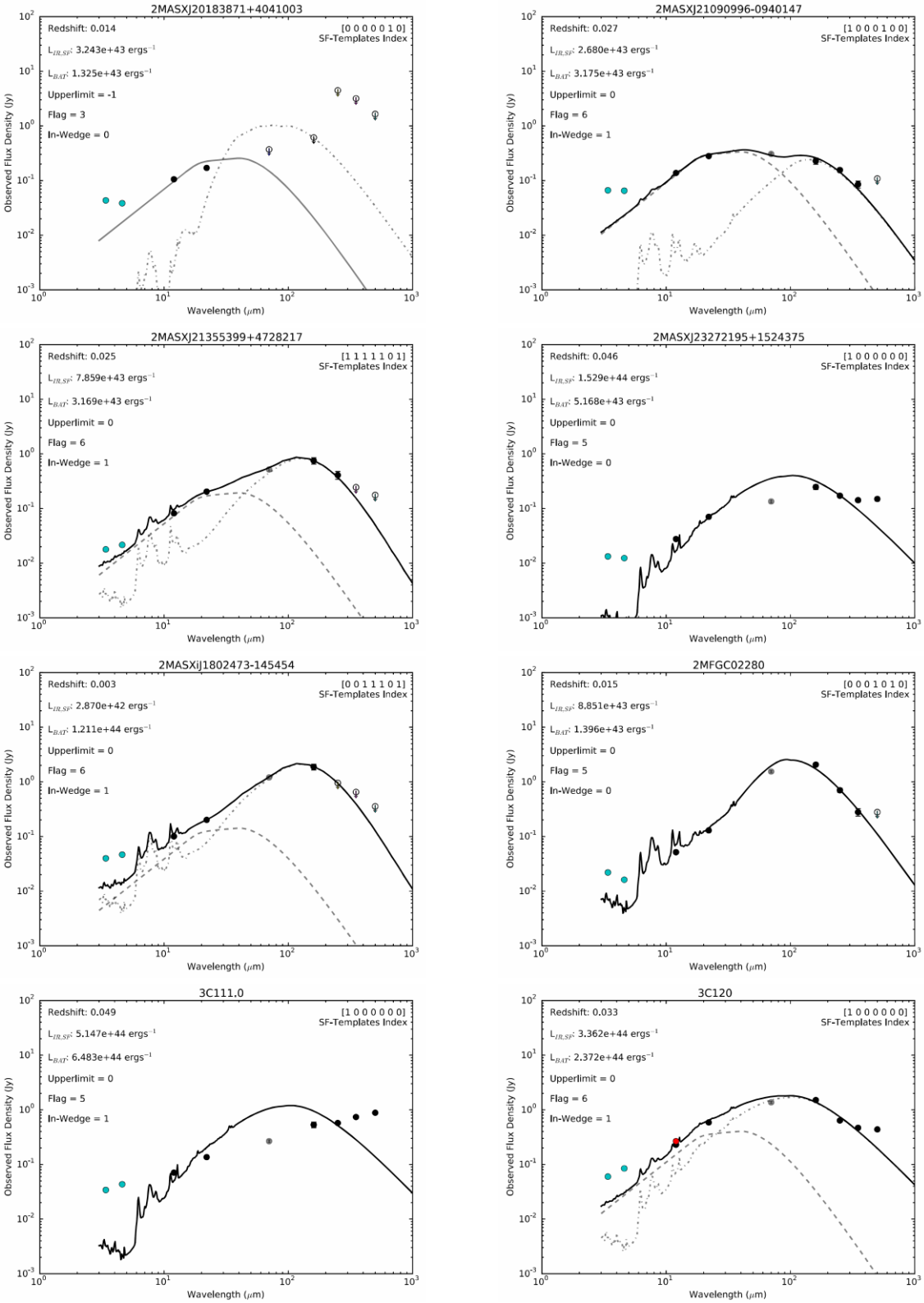

Figure A.8: Continued from Figure A.2, Best-fitted SED solutions for eight Swift-BAT sources (listed alphabetically).

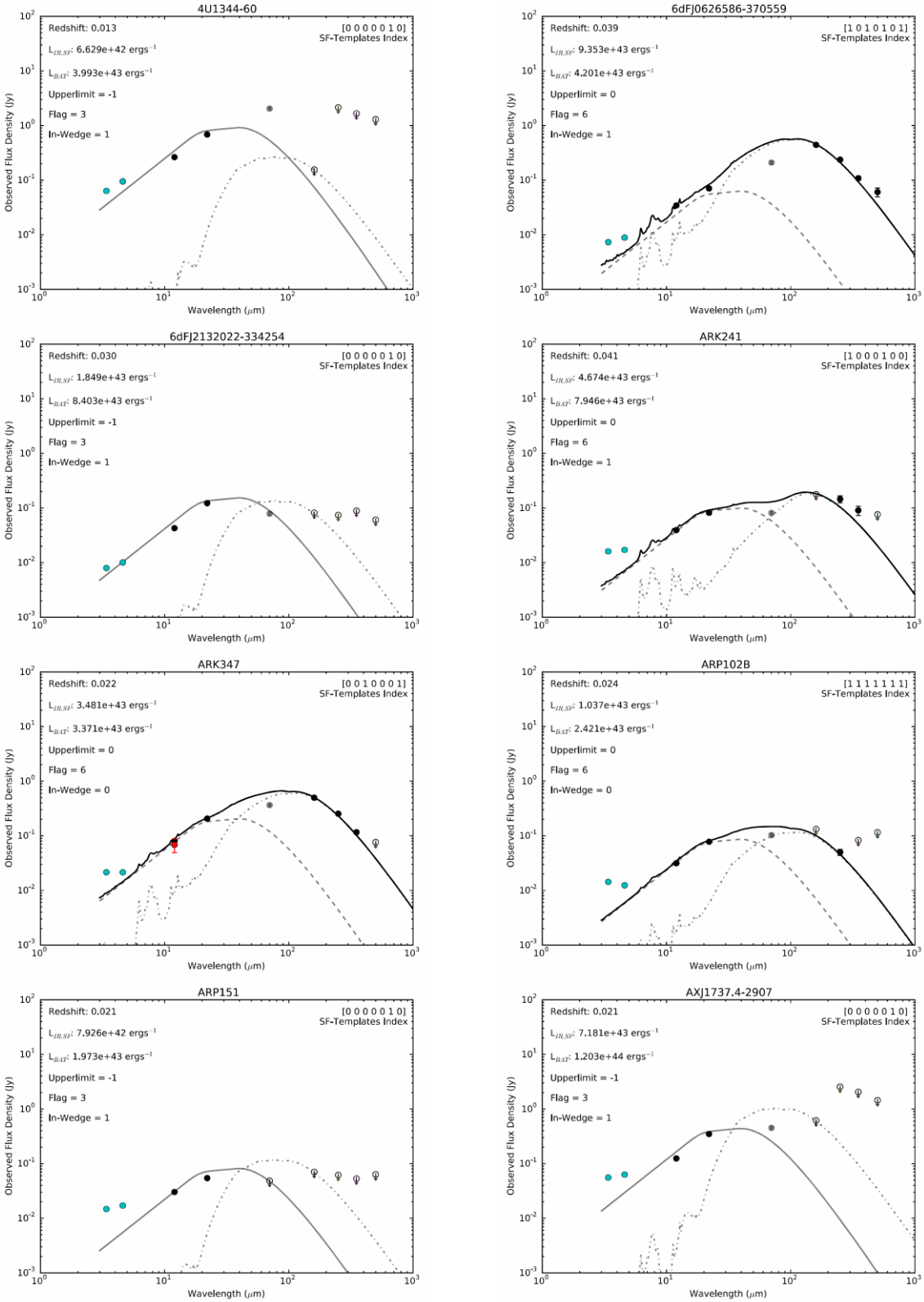

Figure A.9: Continued from Figure A.2, Best-fitted SED solutions for eight Swift-BAT sources (listed alphabetically).

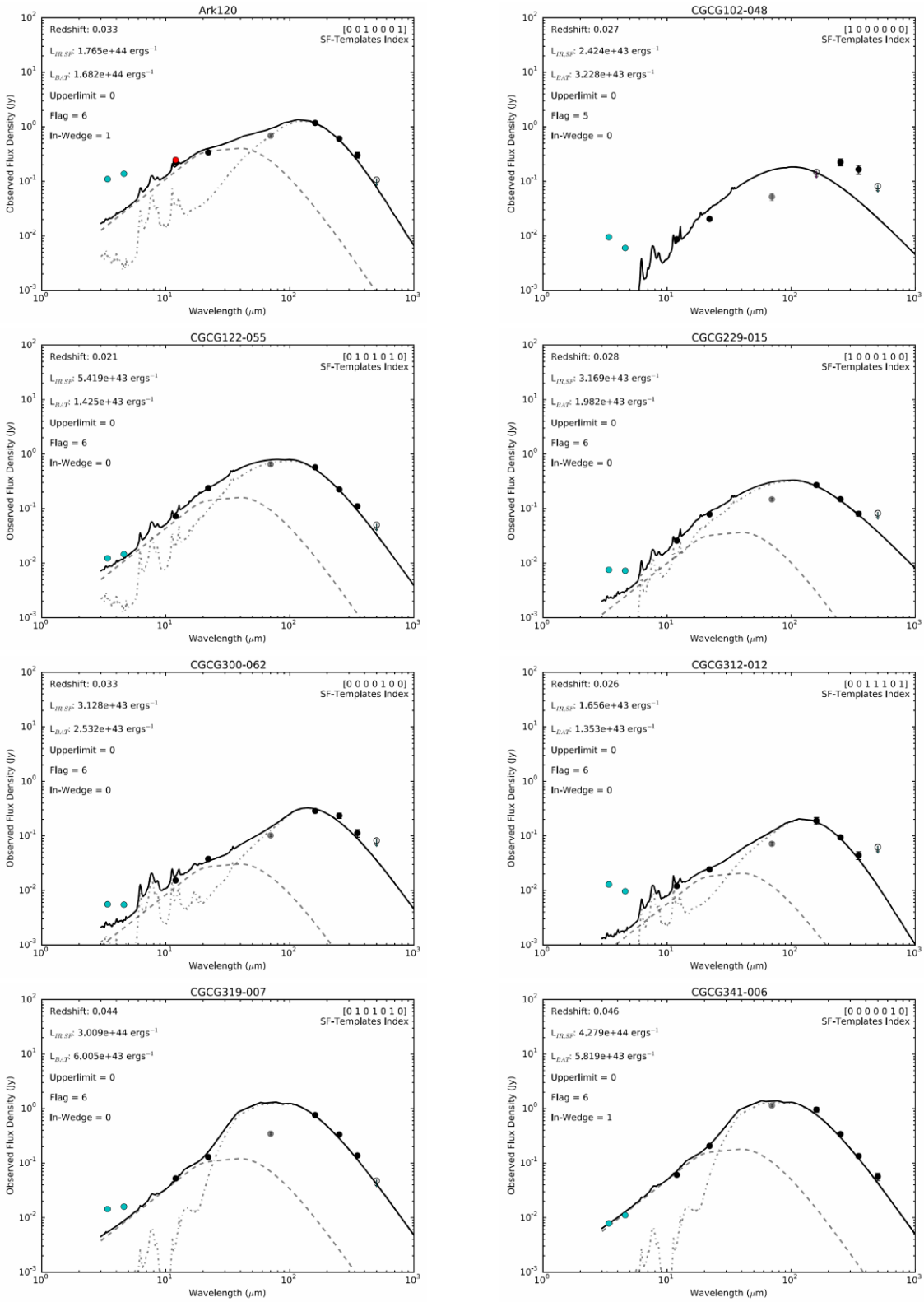

Figure A.20: Continued from Figure A.2, Best-fitted SED solutions for eight Swift-BAT sources (listed alphabetically).

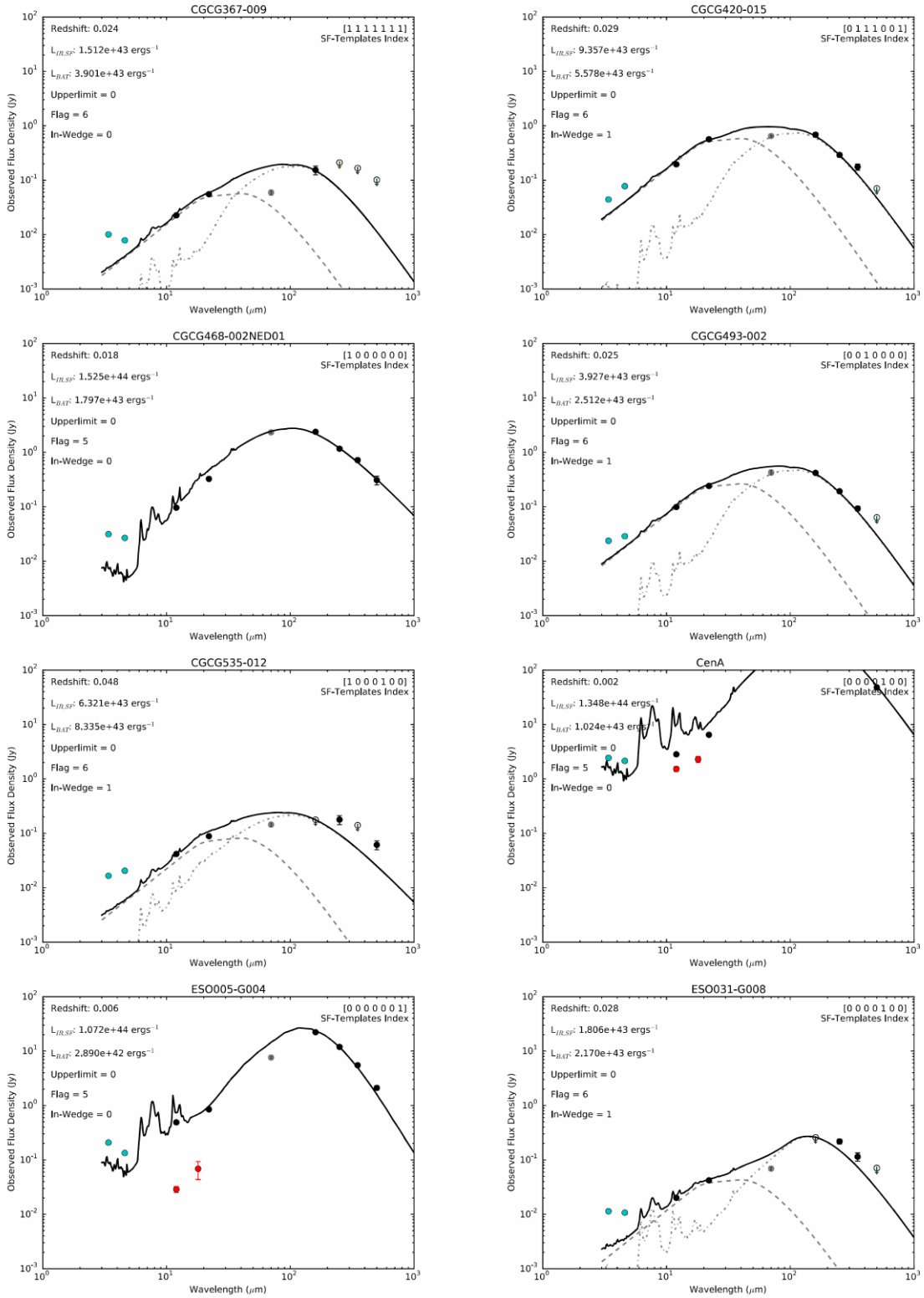

Figure A.21: Continued from Figure A.2, Best-fitted SED solutions for eight Swift-BAT sources (listed alphabetically).

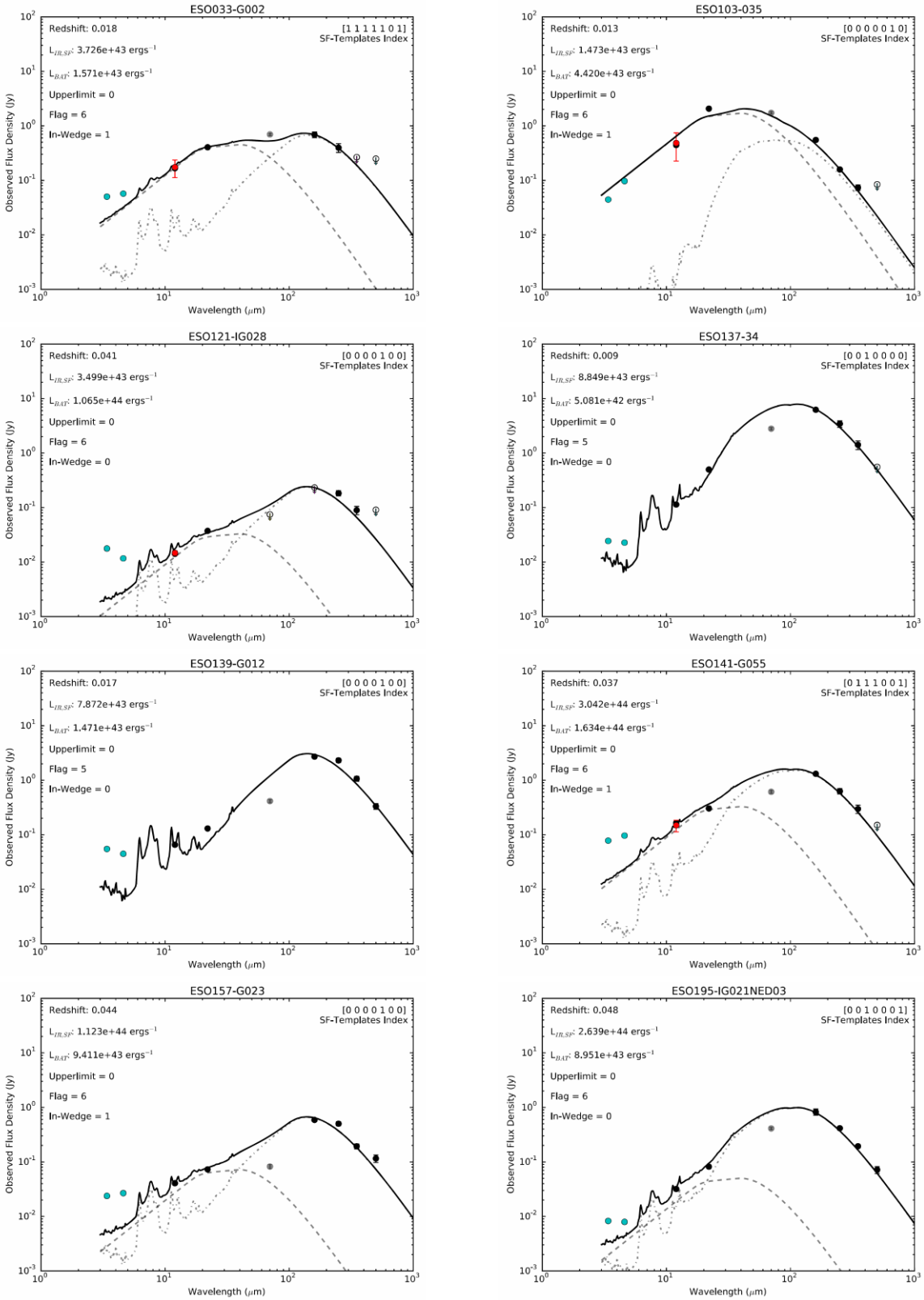

Figure A.22: Continued from Figure A.2, Best-fitted SED solutions for eight Swift-BAT sources (listed alphabetically).

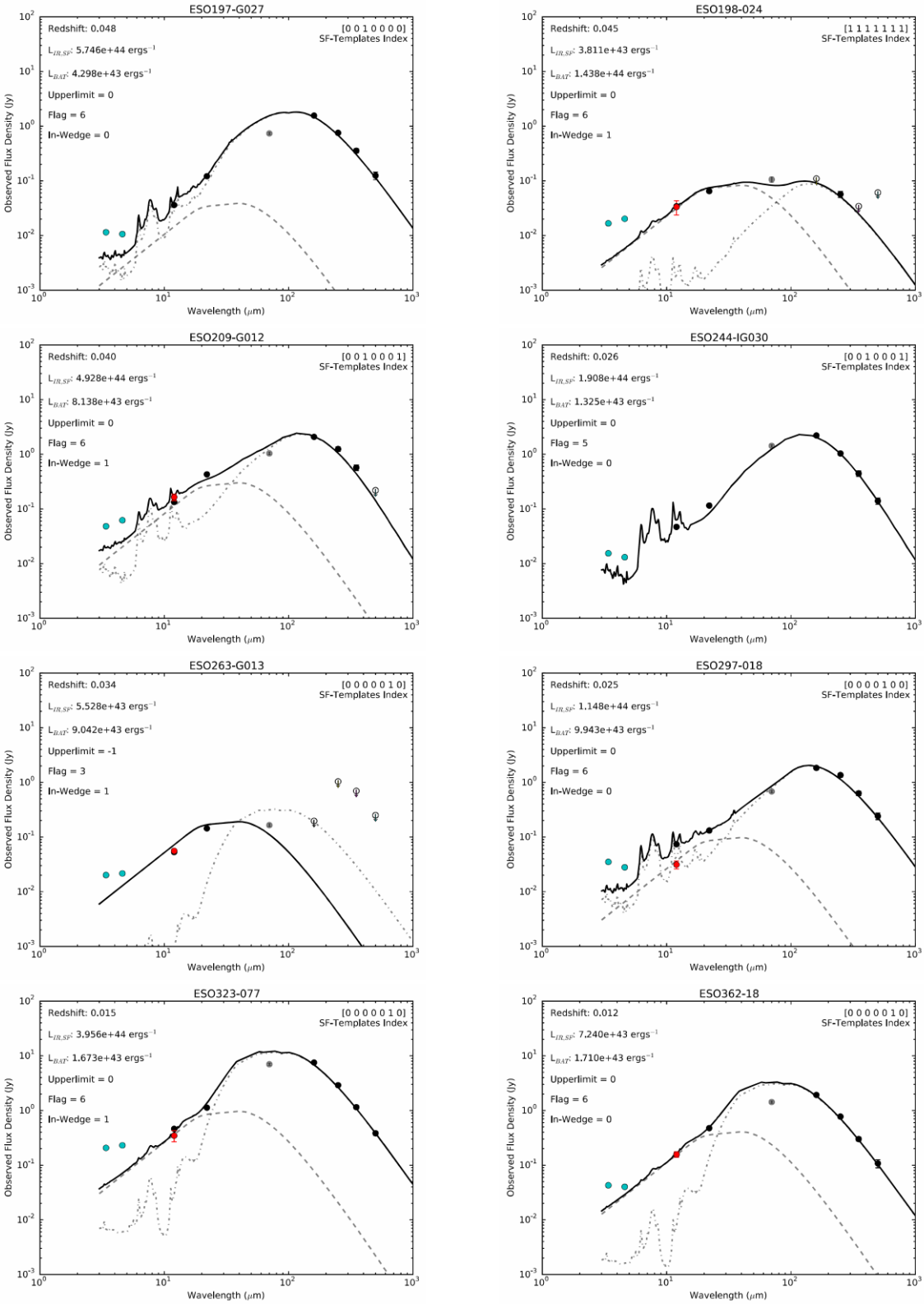

Figure A.23: Continued from Figure A.2, Best-fitted SED solutions for eight Swift-BAT sources (listed alphabetically).

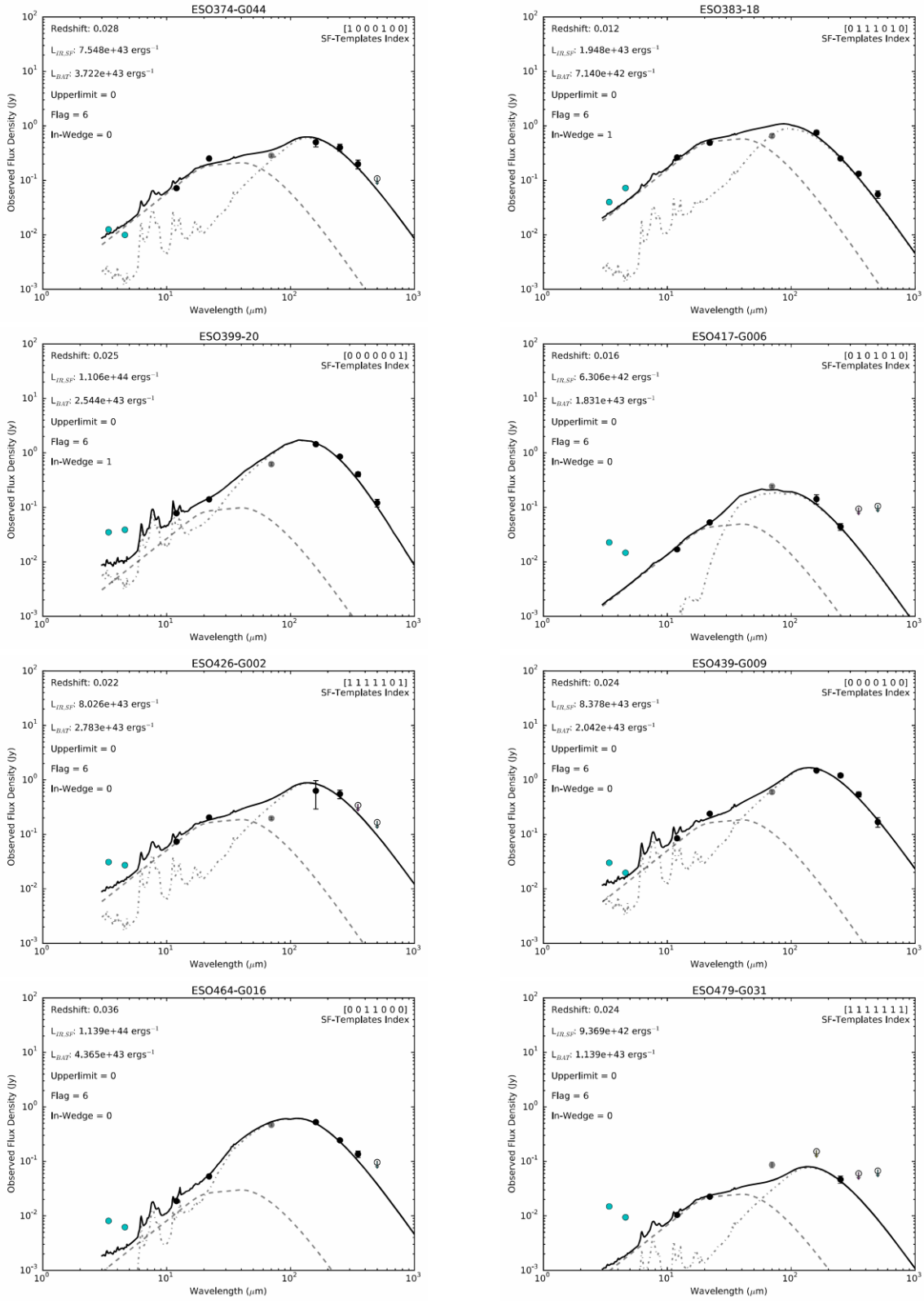

Figure A.24: Continued from Figure A.2, Best-fitted SED solutions for eight Swift-BAT sources (listed alphabetically).

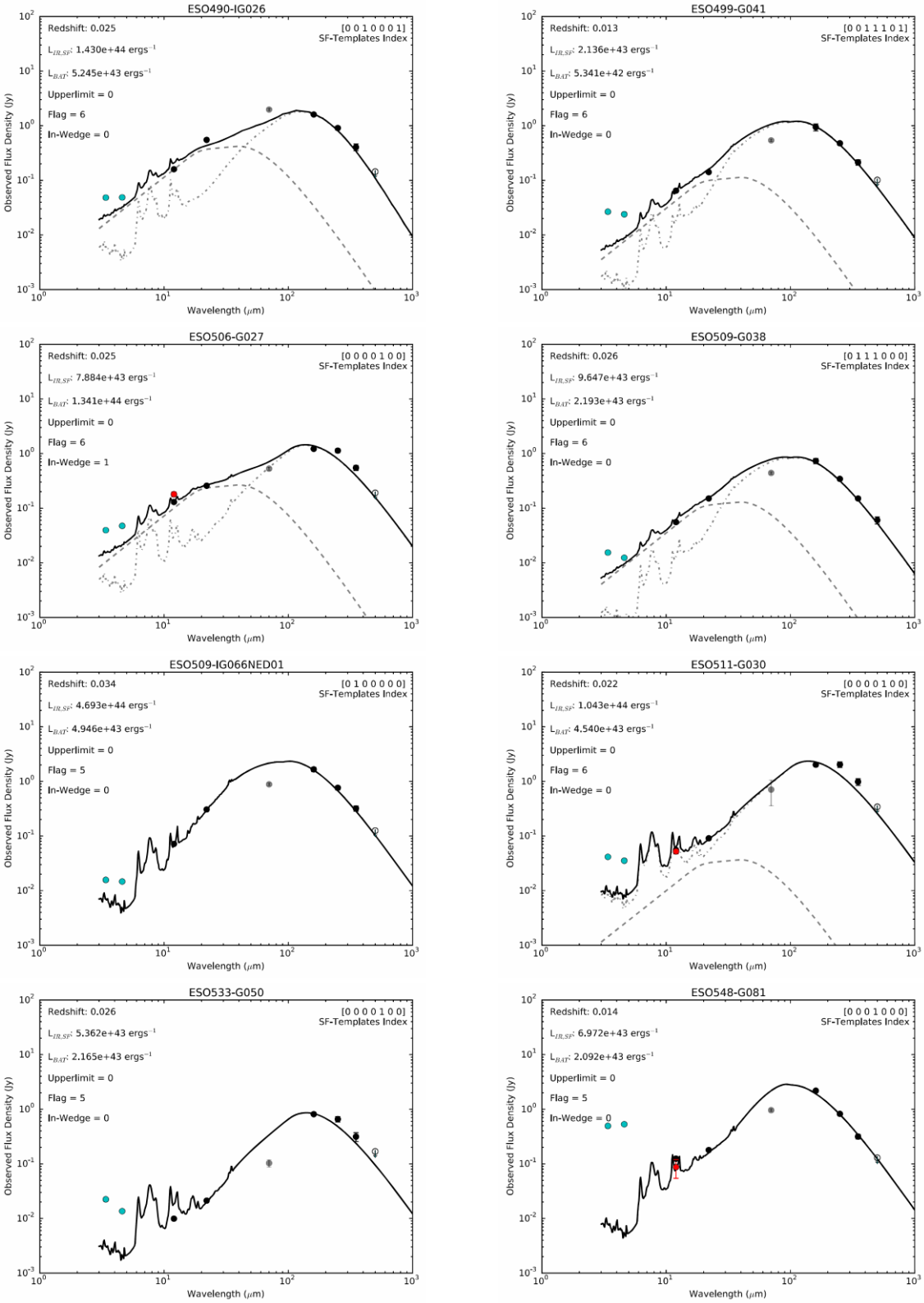

Figure A.25: Continued from Figure A.2, Best-fitted SED solutions for eight Swift-BAT sources (listed alphabetically).

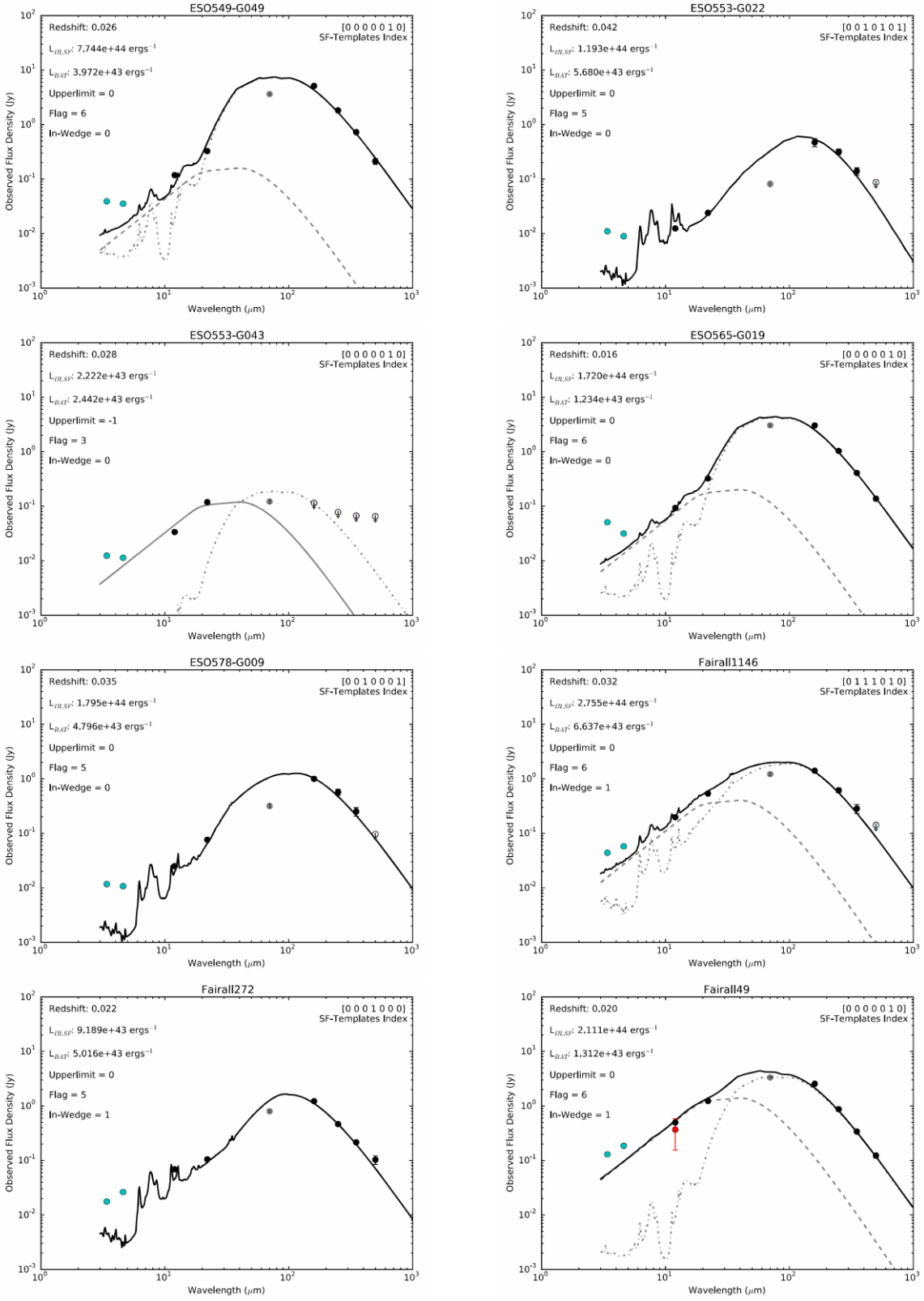

Figure A.26: Continued from Figure A.2, Best-fitted SED solutions for eight Swift-BAT sources (listed alphabetically).

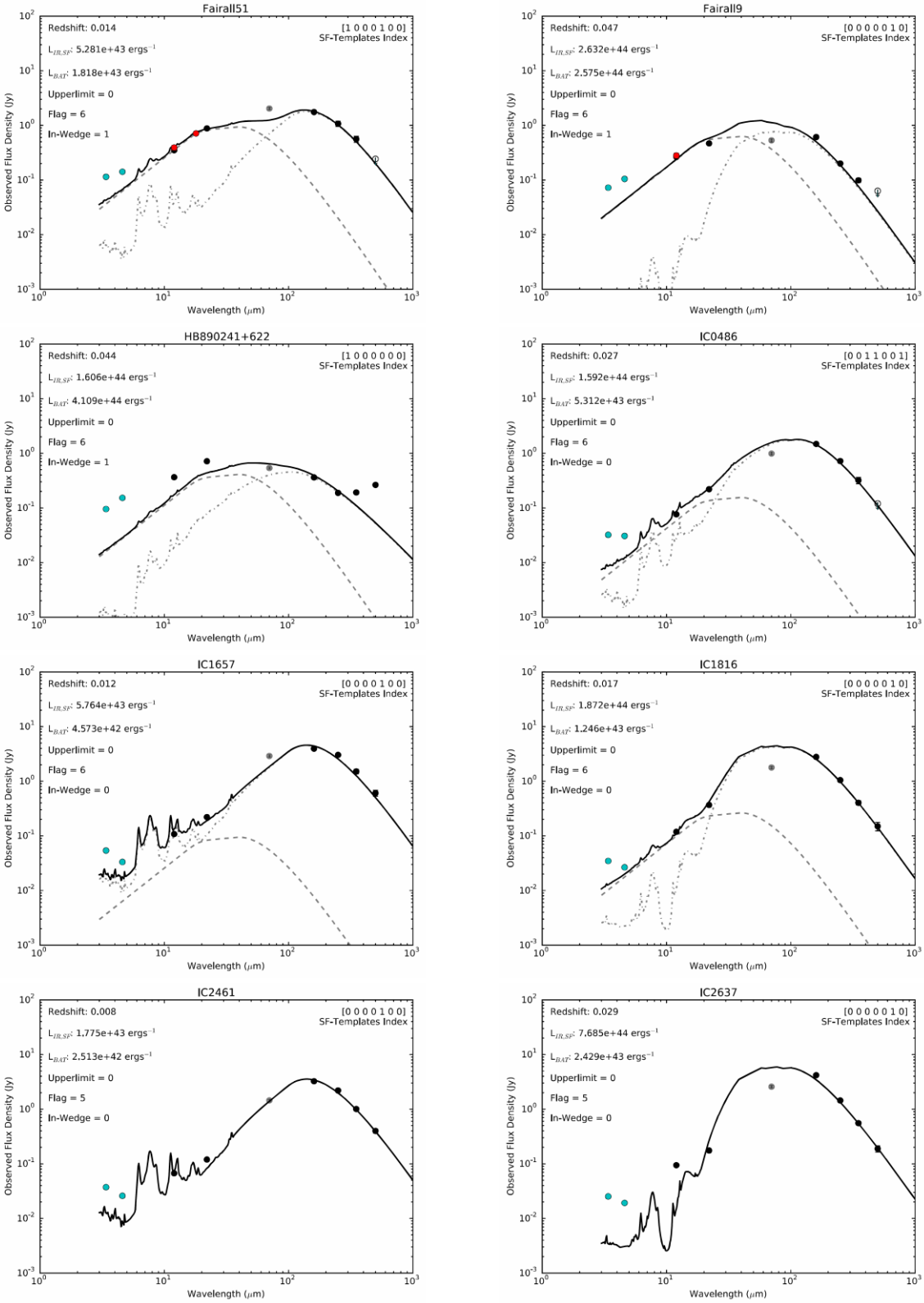

Figure A.27: Continued from Figure A.2, Best-fitted SED solutions for eight Swift-BAT sources (listed alphabetically).

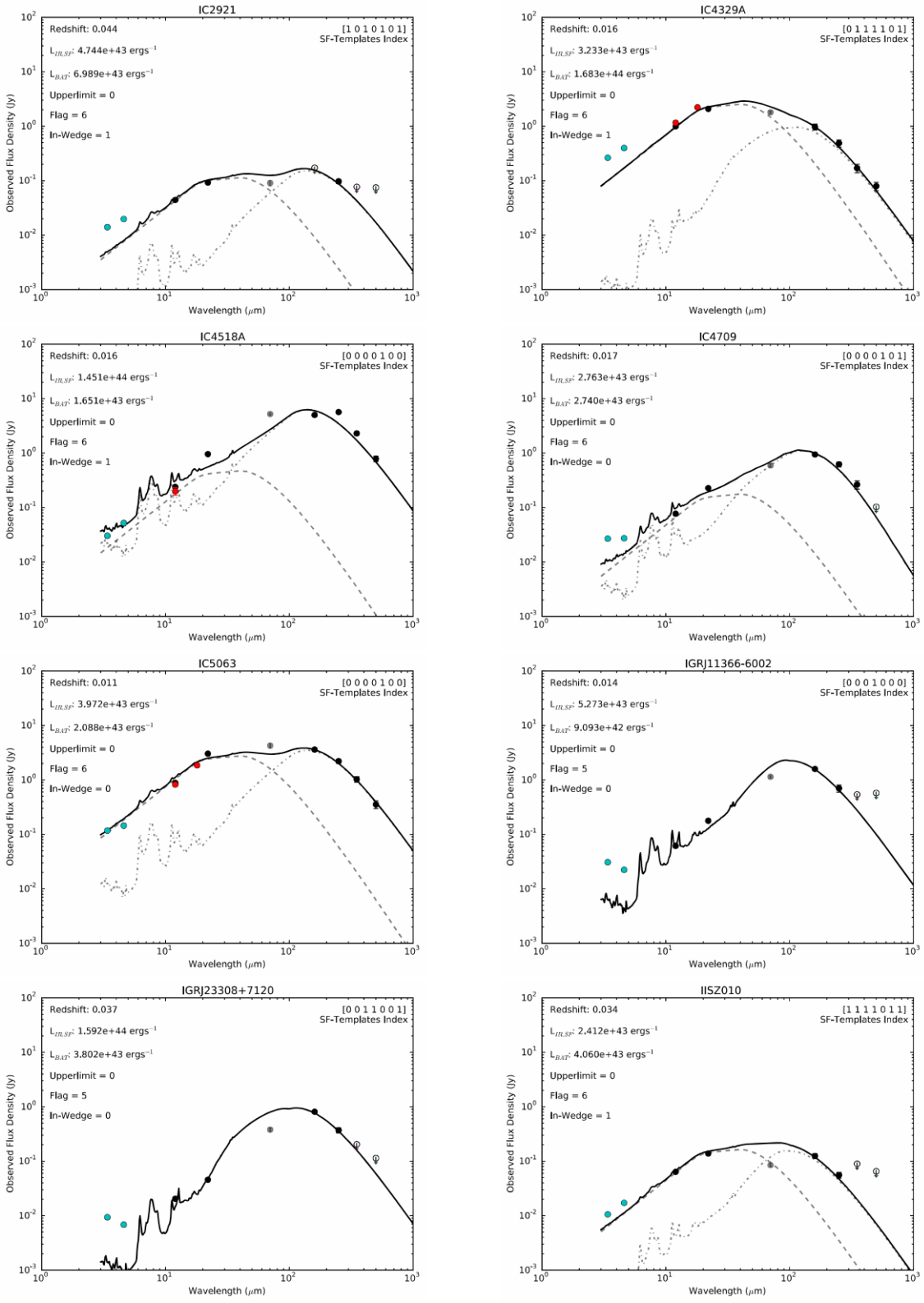

Figure A.28: Continued from Figure A.2, Best-fitted SED solutions for eight Swift-BAT sources (listed alphabetically).

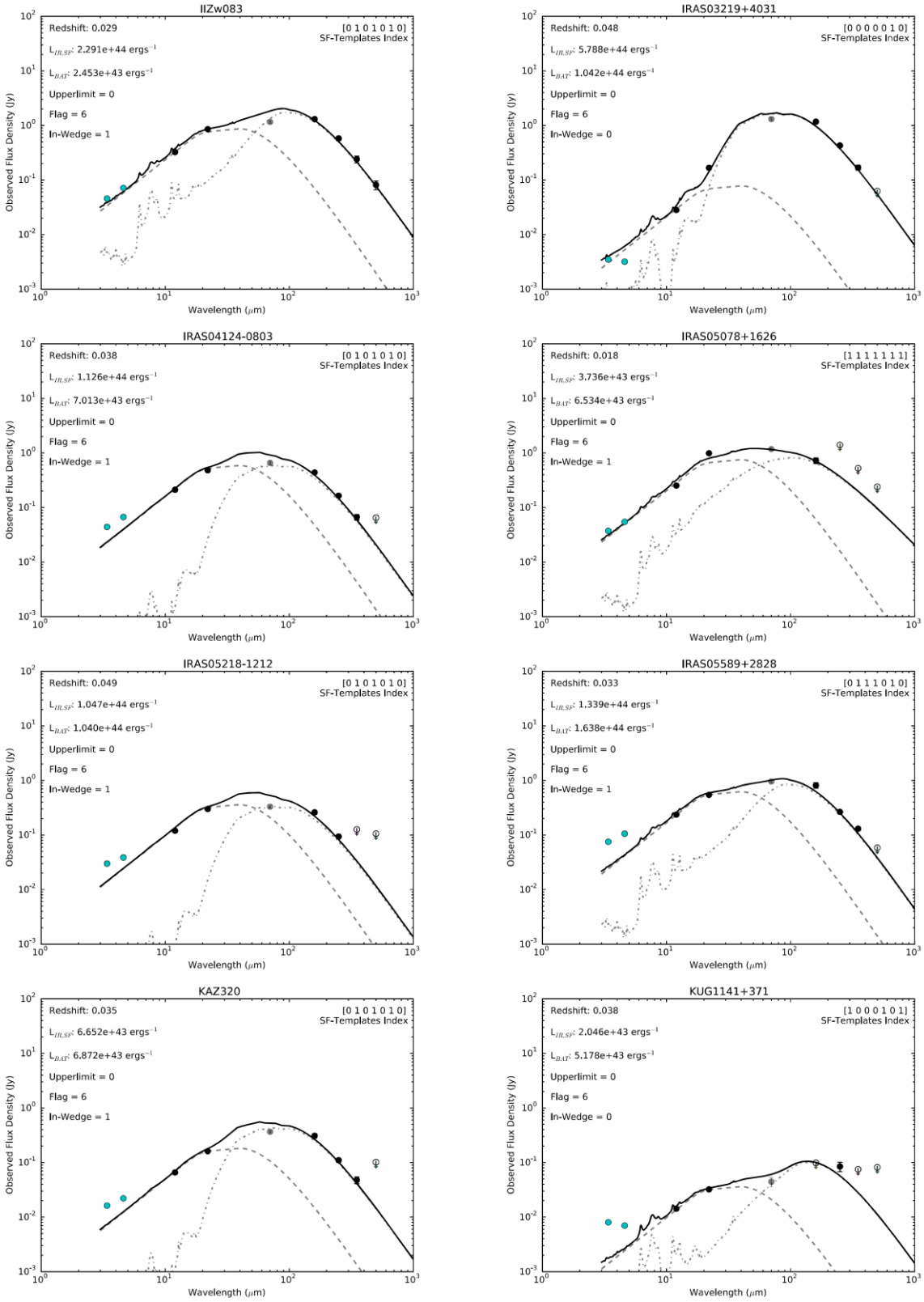

Figure A.29: Continued from Figure A.2, Best-fitted SED solutions for eight Swift-BAT sources (listed alphabetically).

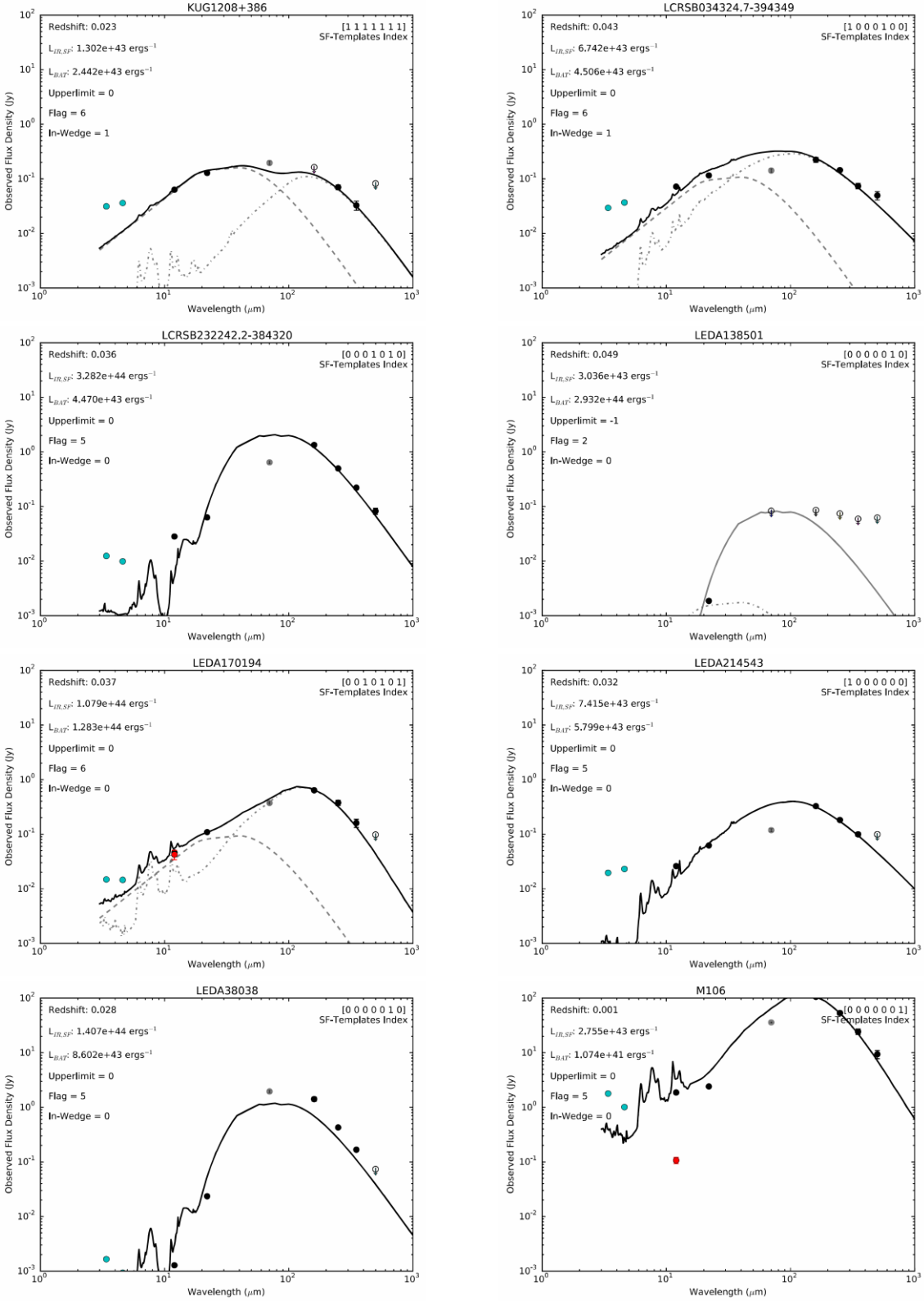

Figure A.20: Continued from Figure A.2, Best-fitted SED solutions for eight Swift-BAT sources (listed alphabetically).

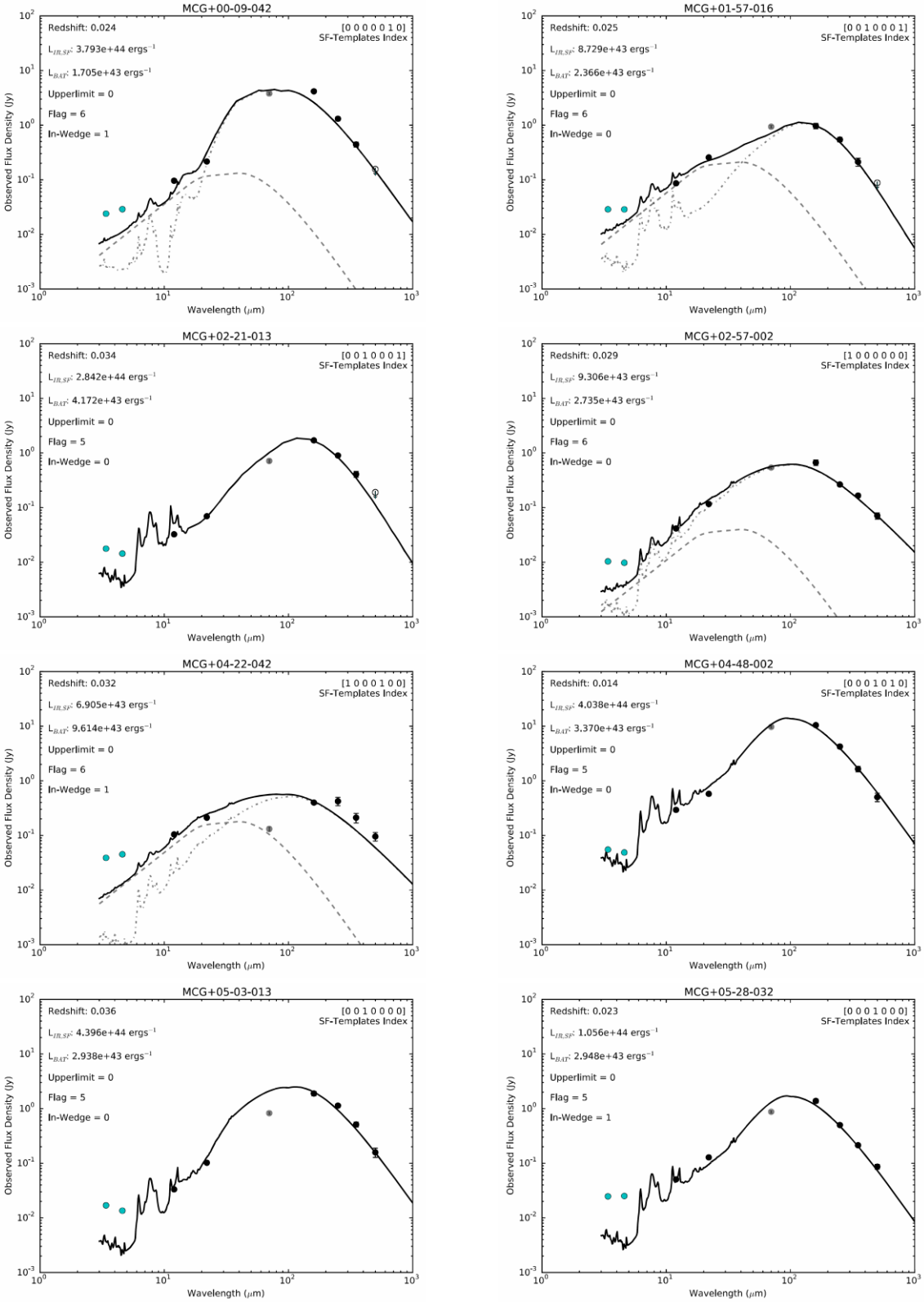

Figure A.21: Continued from Figure A.2, Best-fitted SED solutions for eight Swift-BAT sources (listed alphabetically).

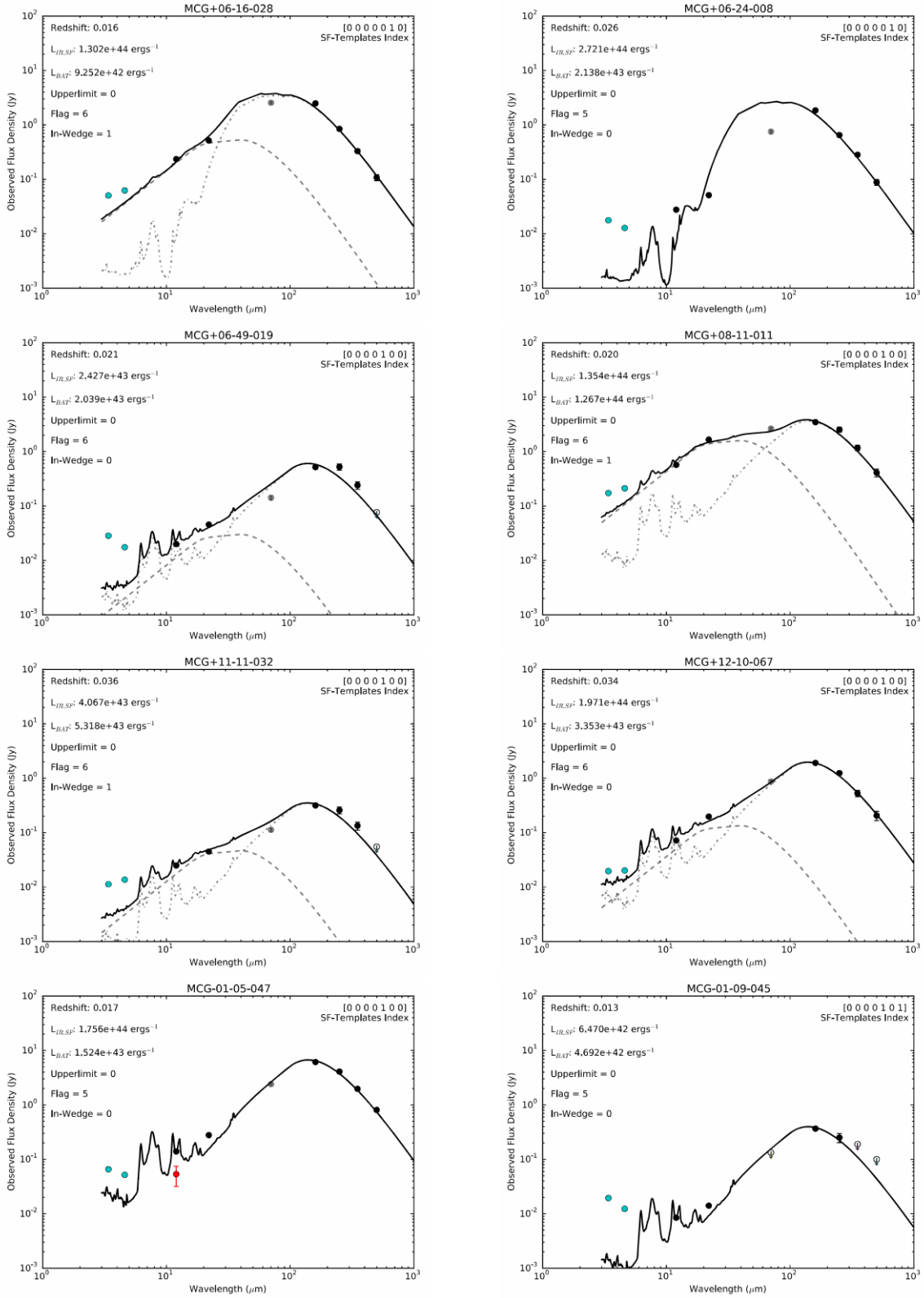

Figure A.22: Continued from Figure A.2, Best-fitted SED solutions for eight Swift-BAT sources (listed alphabetically).

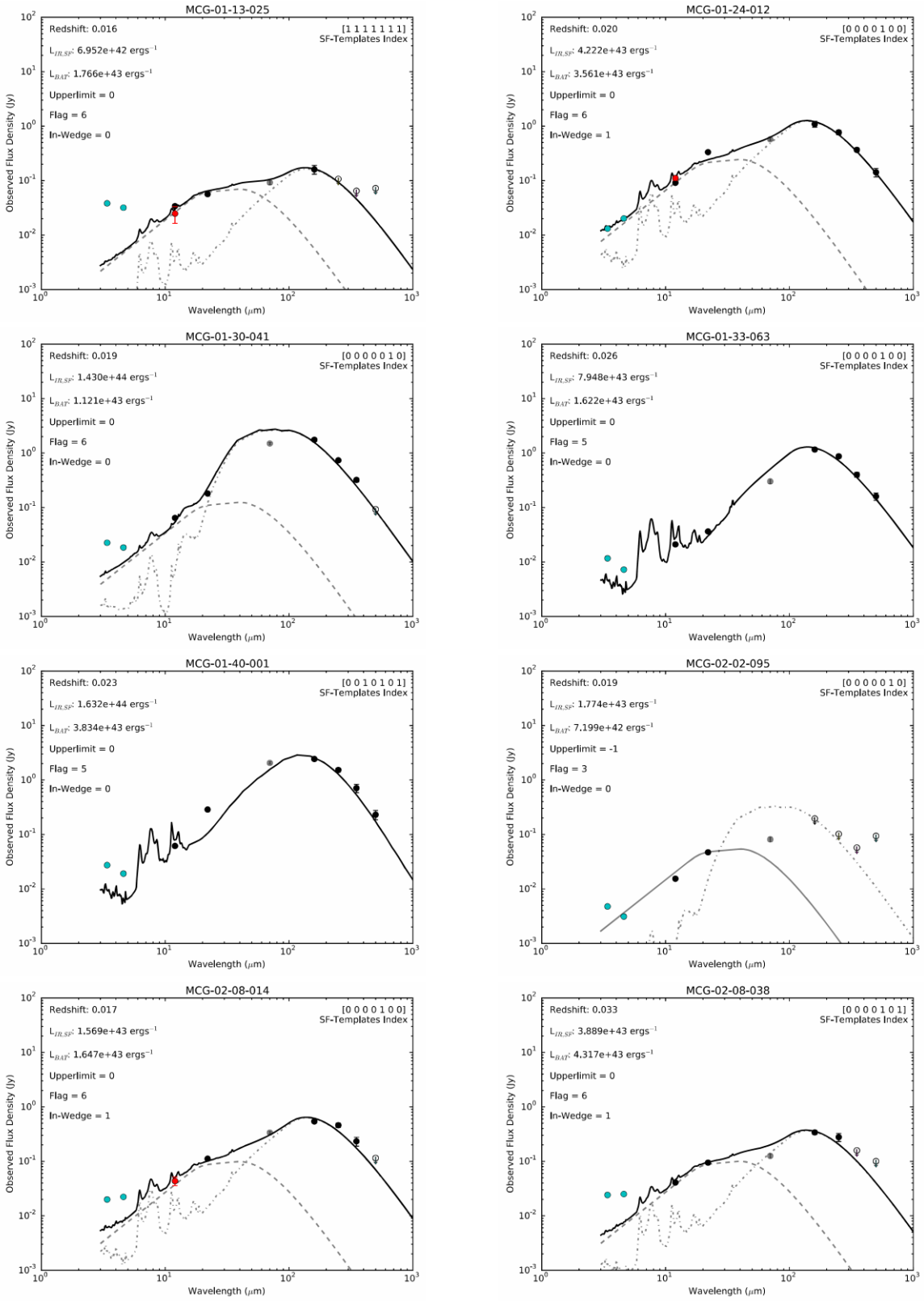

Figure A.23: Continued from Figure A.2, Best-fitted SED solutions for eight Swift-BAT sources (listed alphabetically).

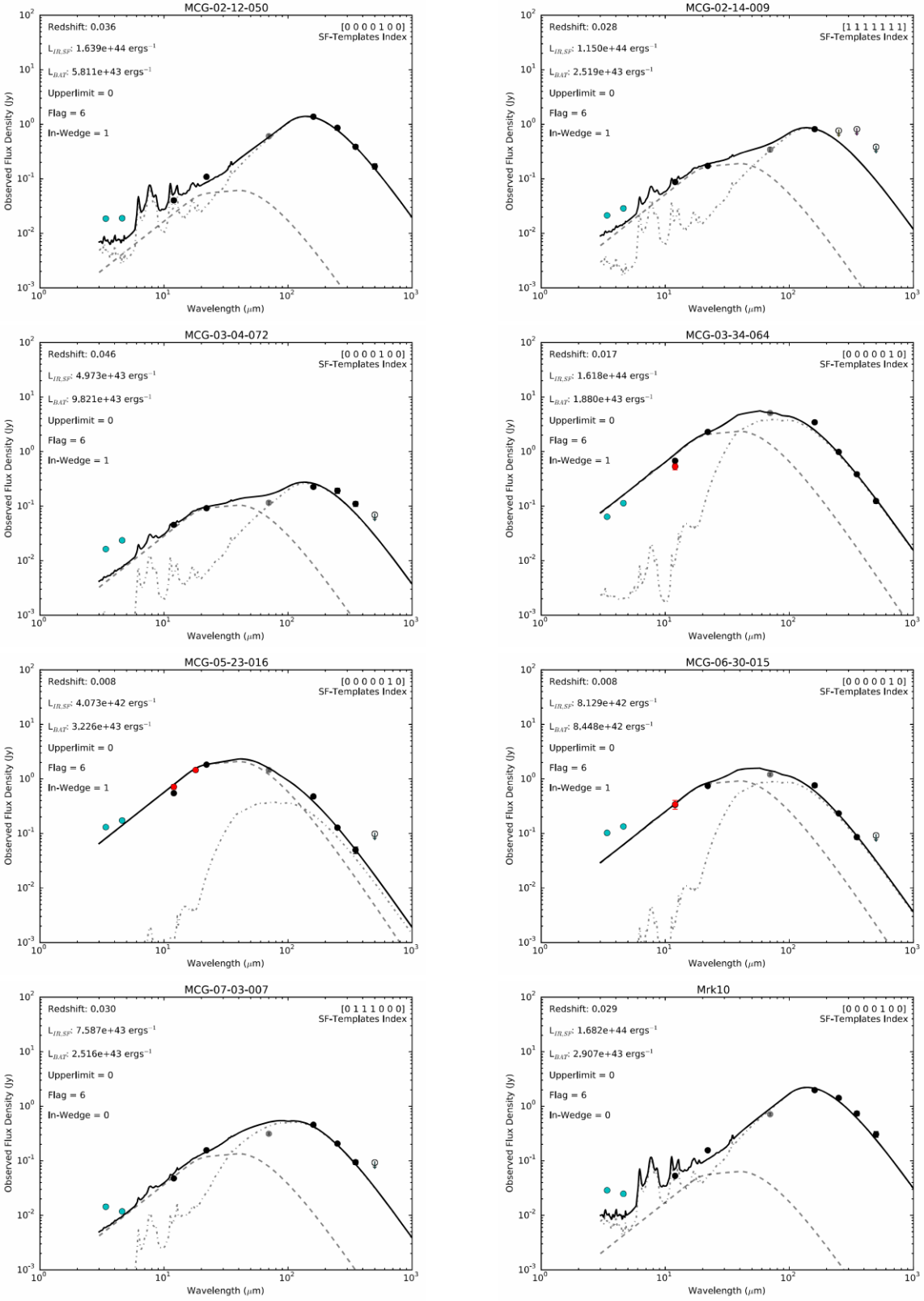

Figure A.24: Continued from Figure A.2, Best-fitted SED solutions for eight Swift-BAT sources (listed alphabetically).

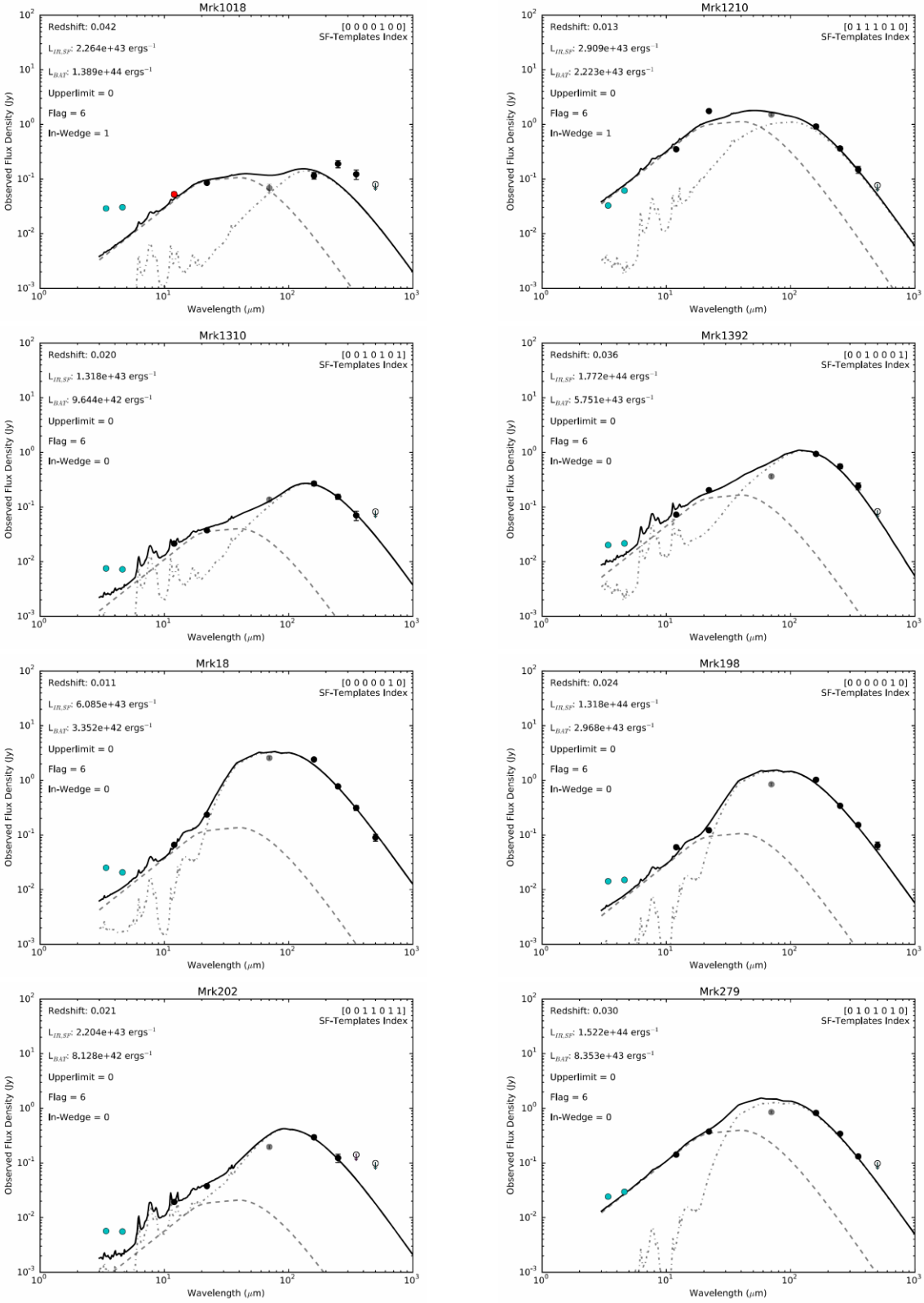

Figure A.25: Continued from Figure A.2, Best-fitted SED solutions for eight Swift-BAT sources (listed alphabetically).

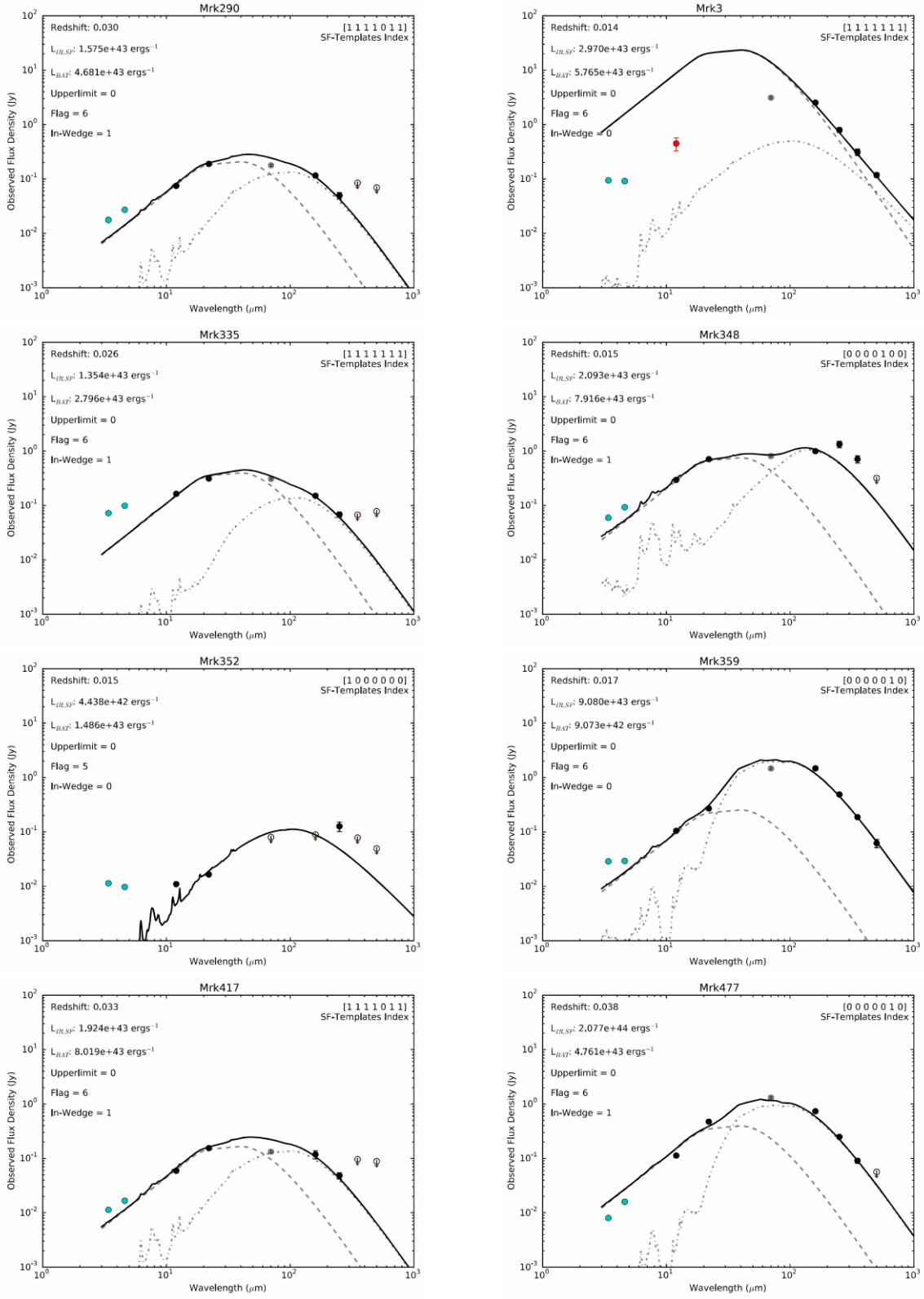

Figure A.26: Continued from Figure A.2, Best-fitted SED solutions for eight Swift-BAT sources (listed alphabetically).

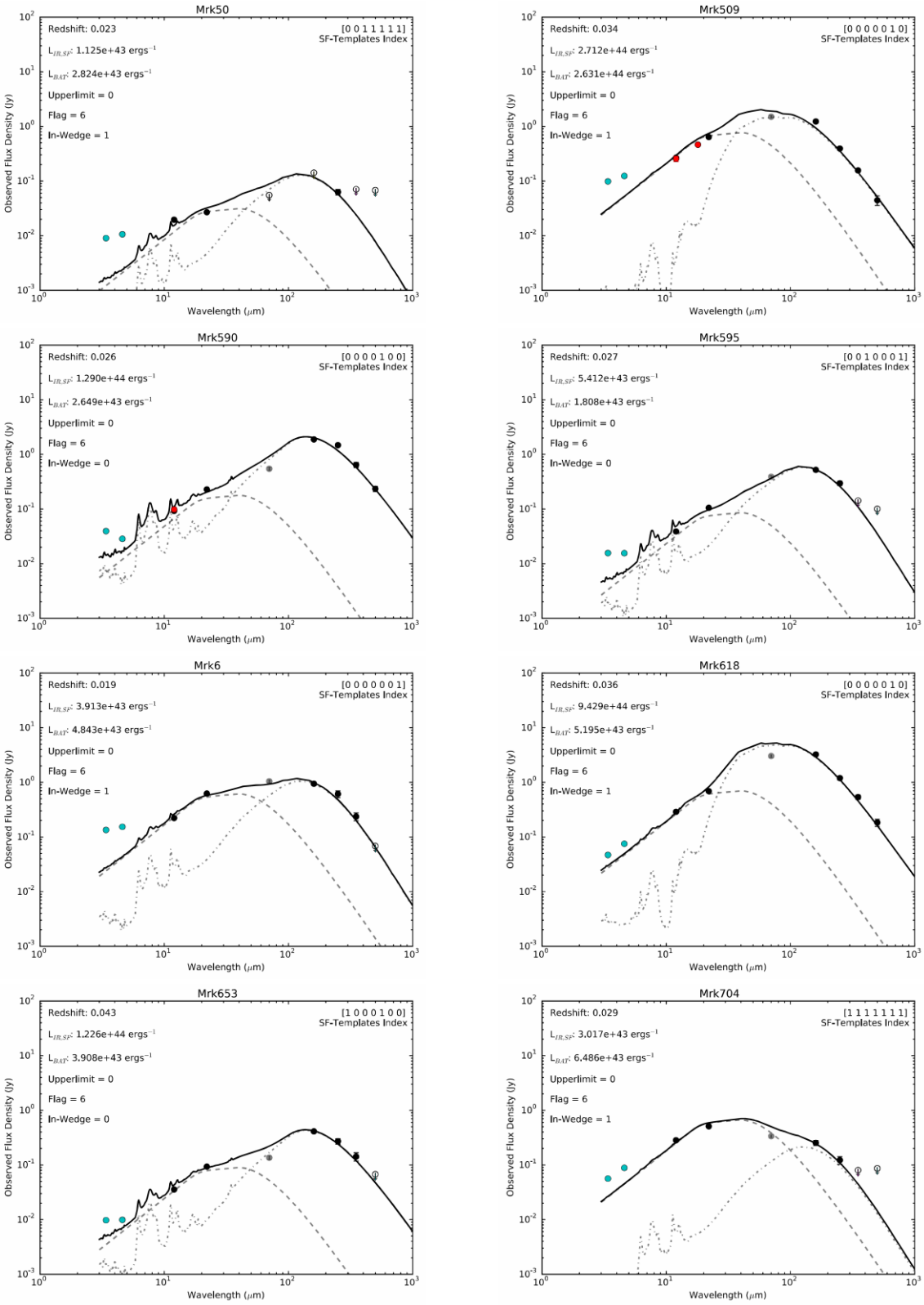

Figure A.27: Continued from Figure A.2, Best-fitted SED solutions for eight Swift-BAT sources (listed alphabetically).

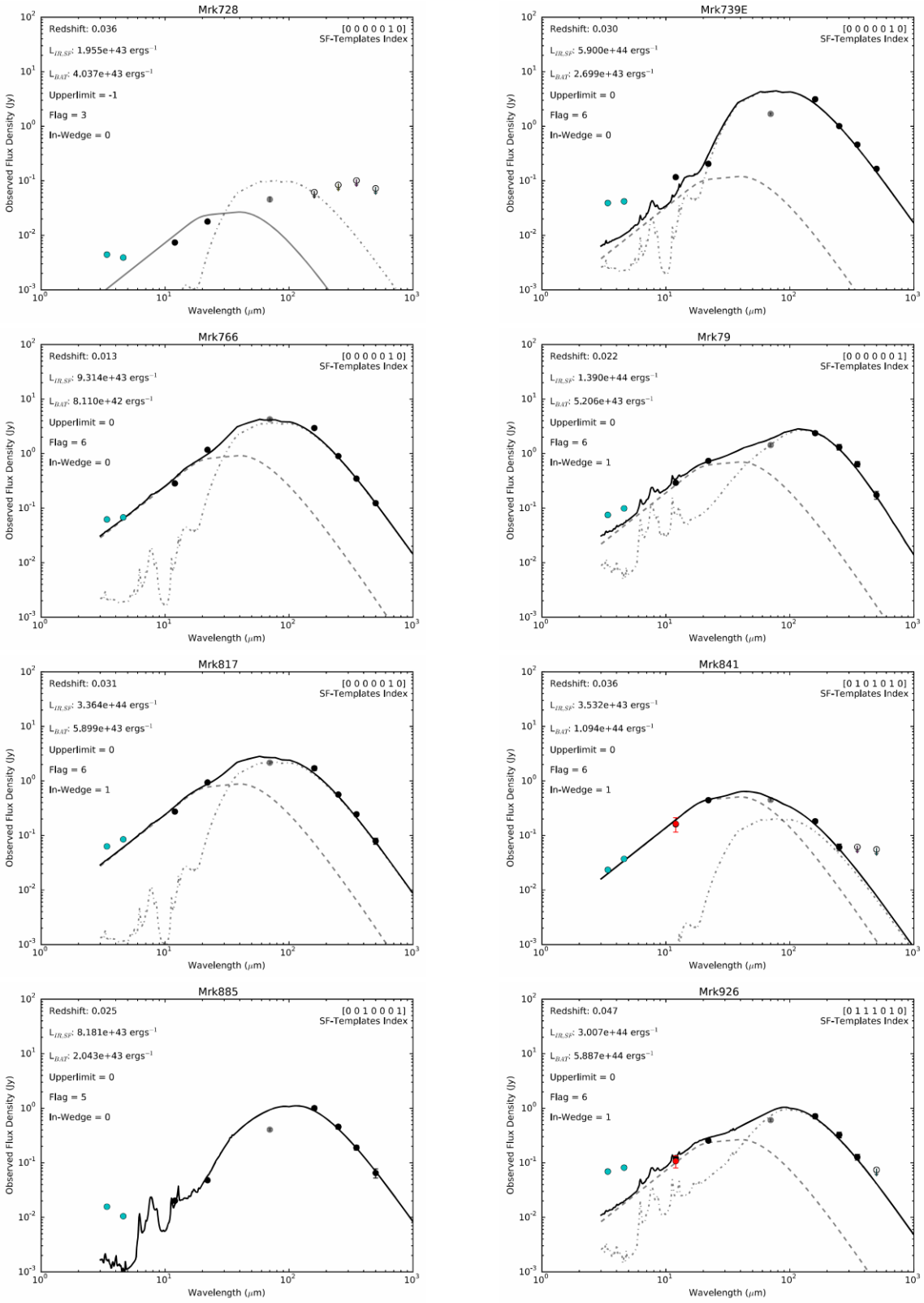

Figure A.28: Continued from Figure A.2, Best-fitted SED solutions for eight Swift-BAT sources (listed alphabetically).

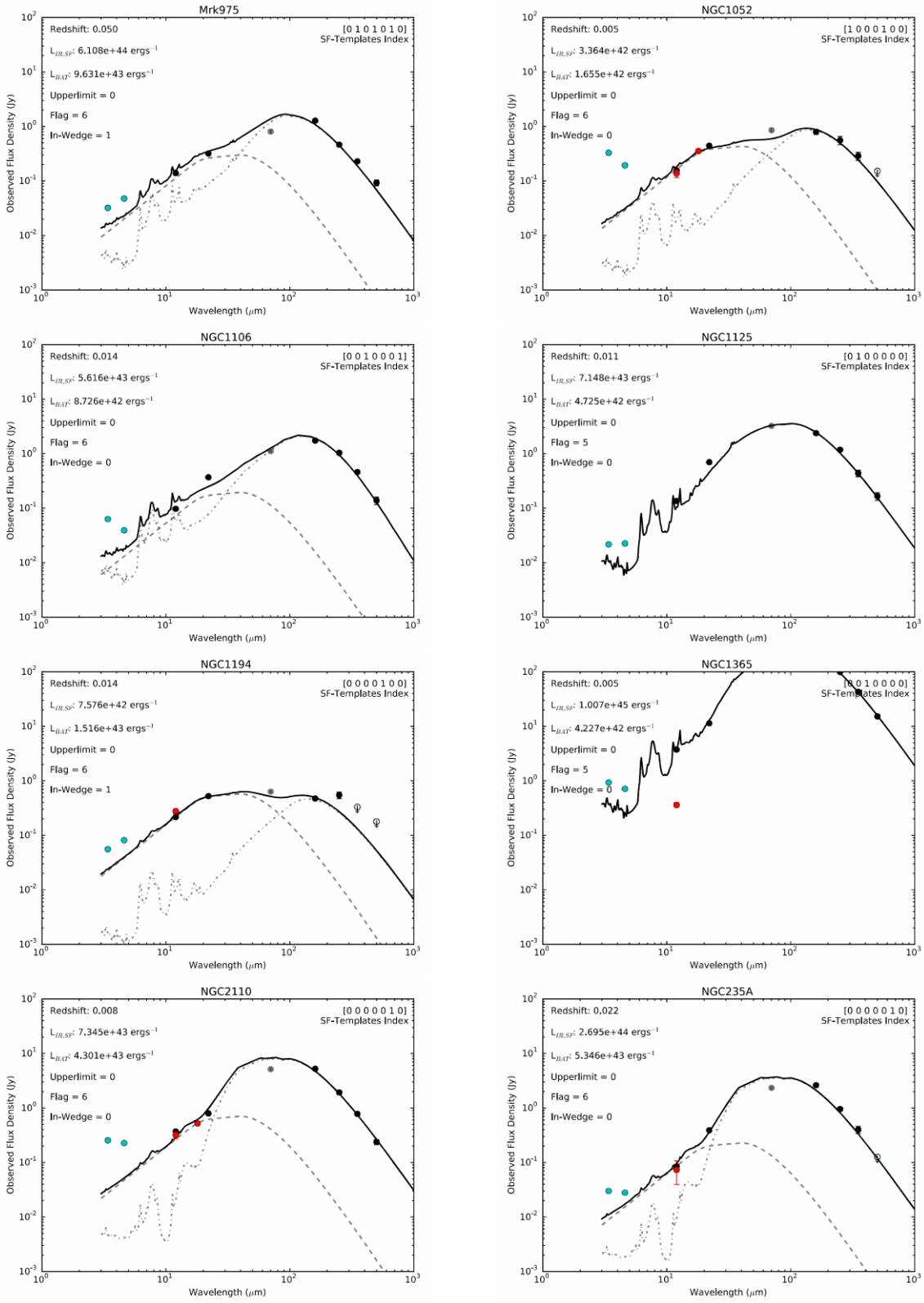

Figure A.29: Continued from Figure A.2, Best-fitted SED solutions for eight Swift-BAT sources (listed alphabetically).

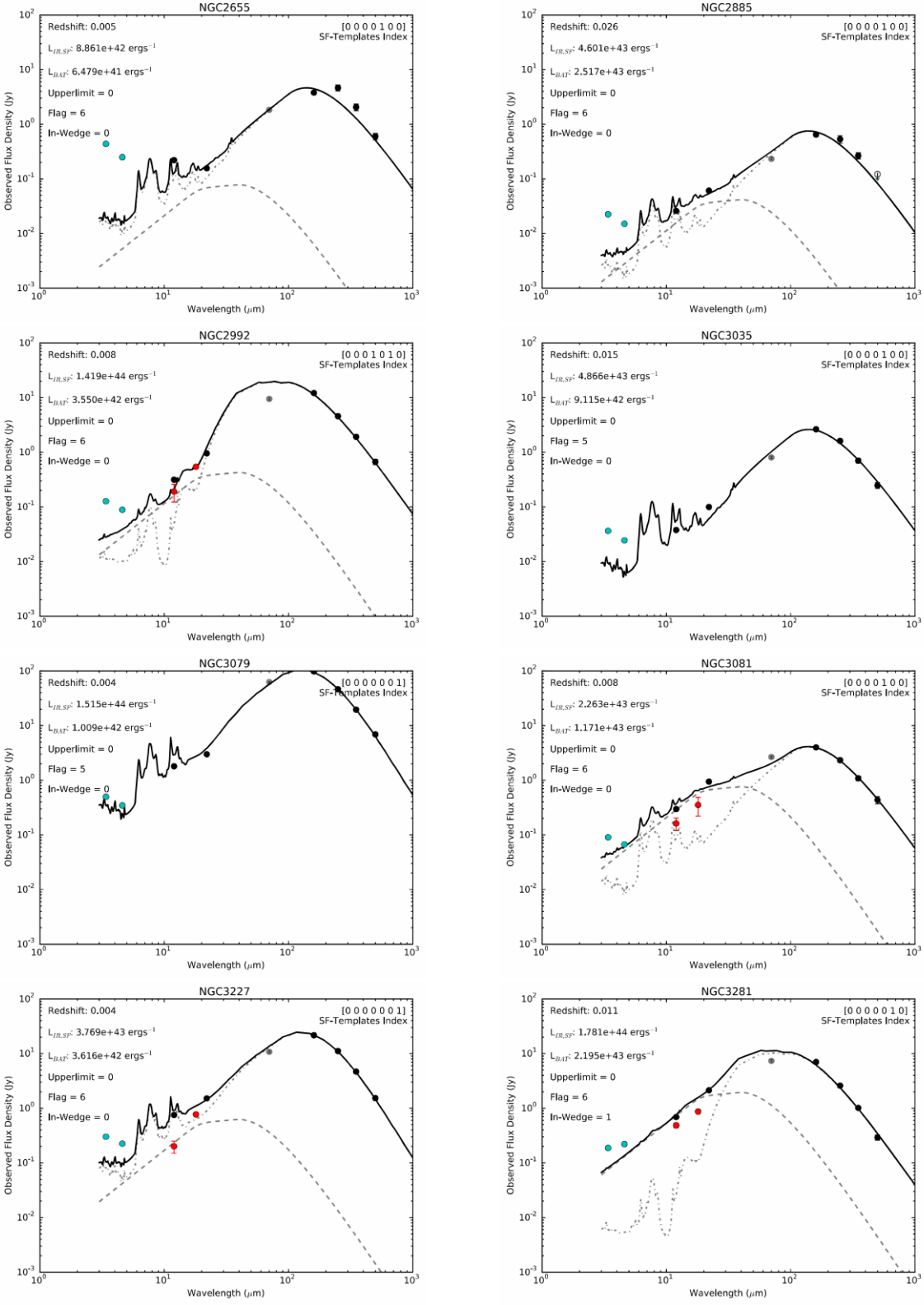

Figure A.30: Continued from Figure A.2, Best-fitted SED solutions for eight Swift-BAT sources (listed alphabetically).

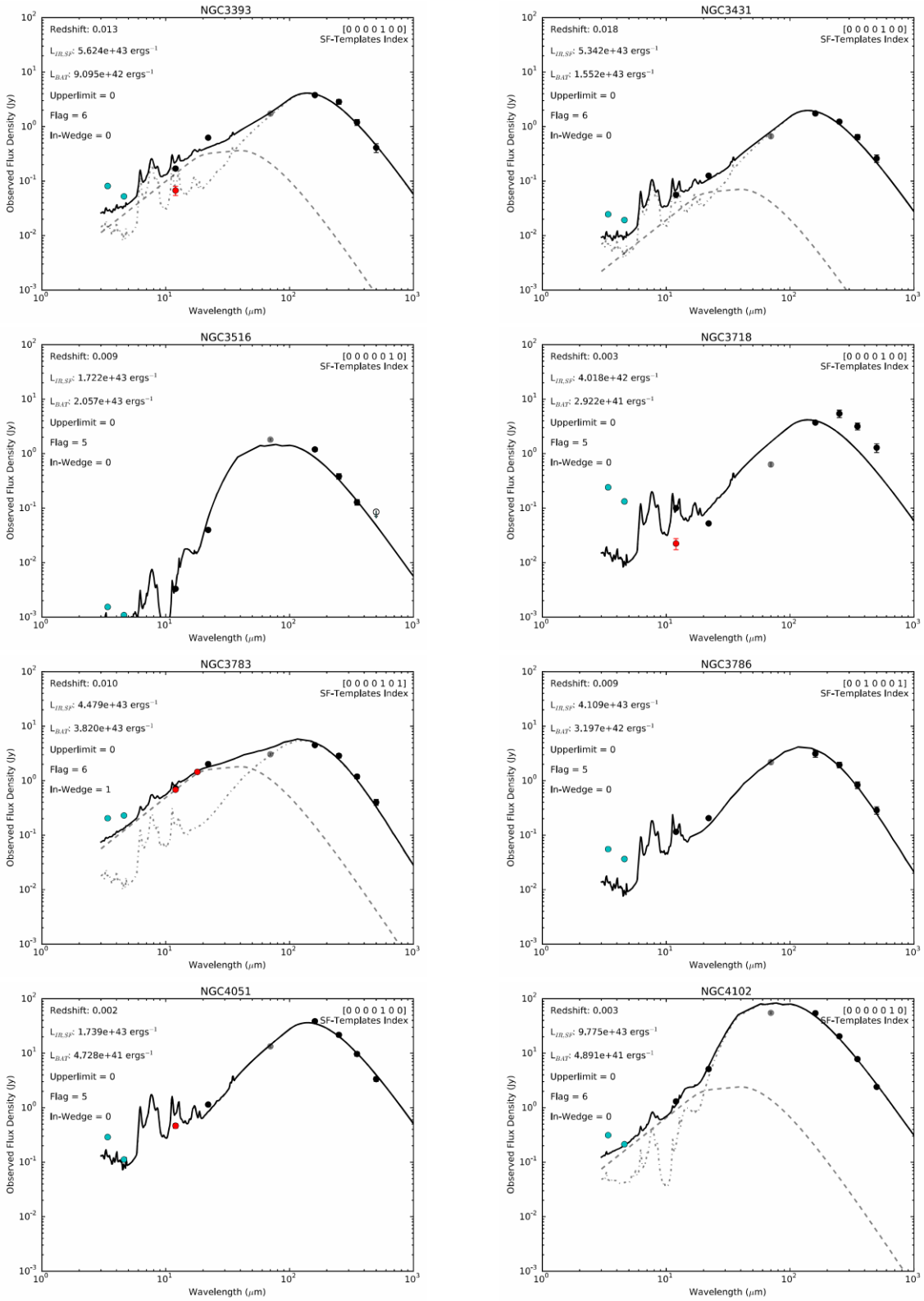

Figure A.31: Continued from Figure A.2, Best-fitted SED solutions for eight Swift-BAT sources (listed alphabetically).

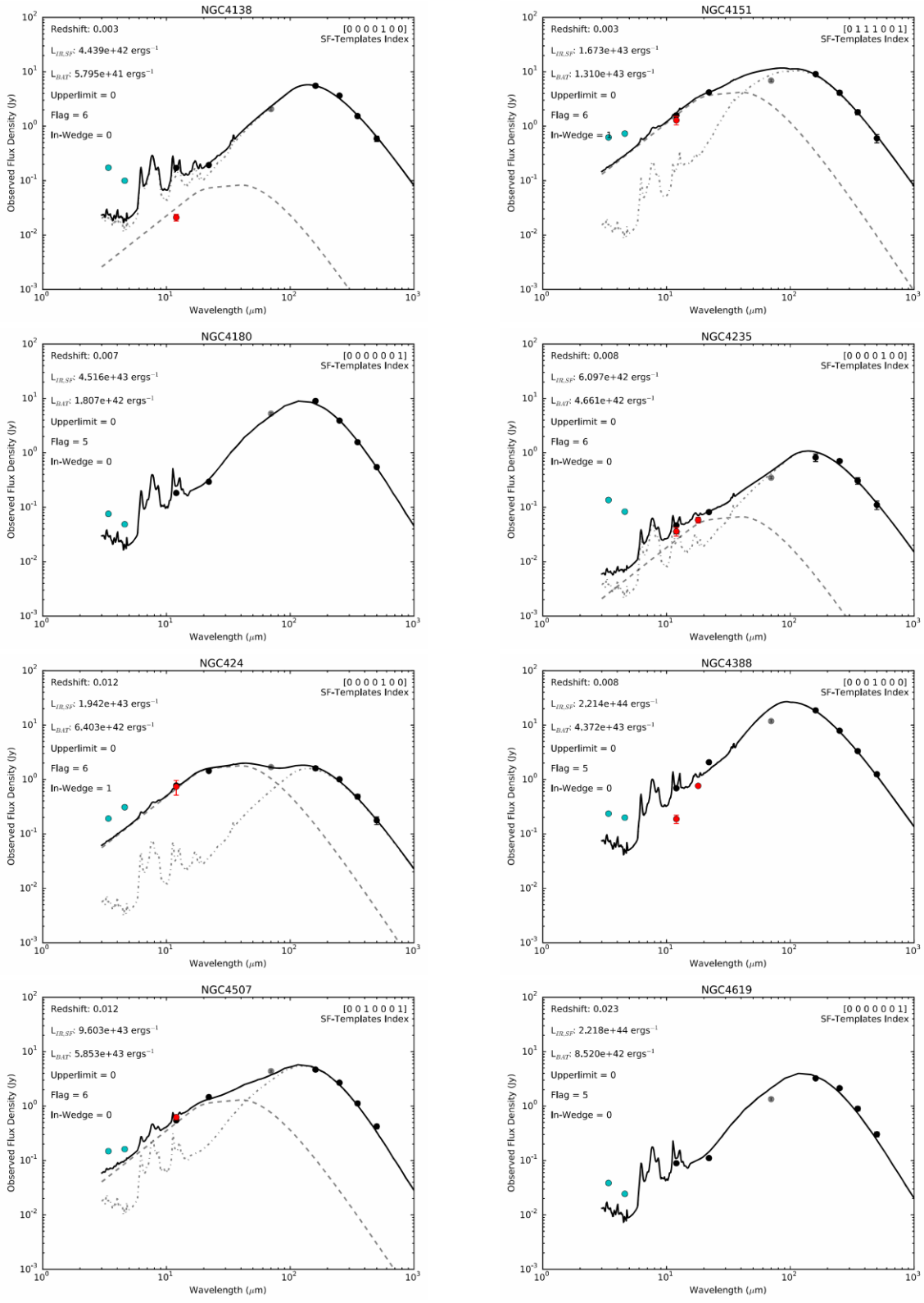

Figure A.32: Continued from Figure A.2, Best-fitted SED solutions for eight Swift-BAT sources (listed alphabetically).

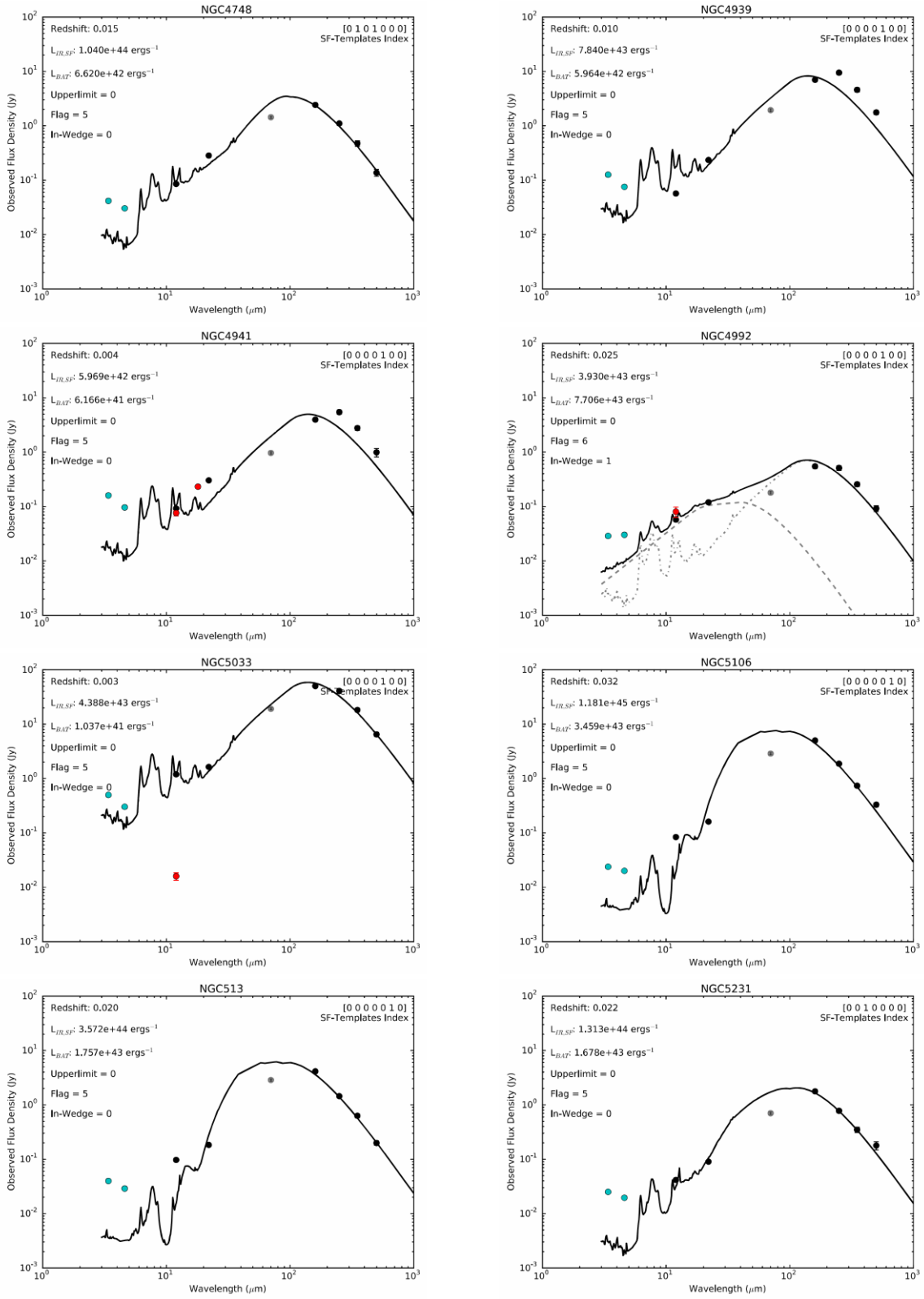

Figure A.33: Continued from Figure A.2, Best-fitted SED solutions for eight Swift-BAT sources (listed alphabetically).

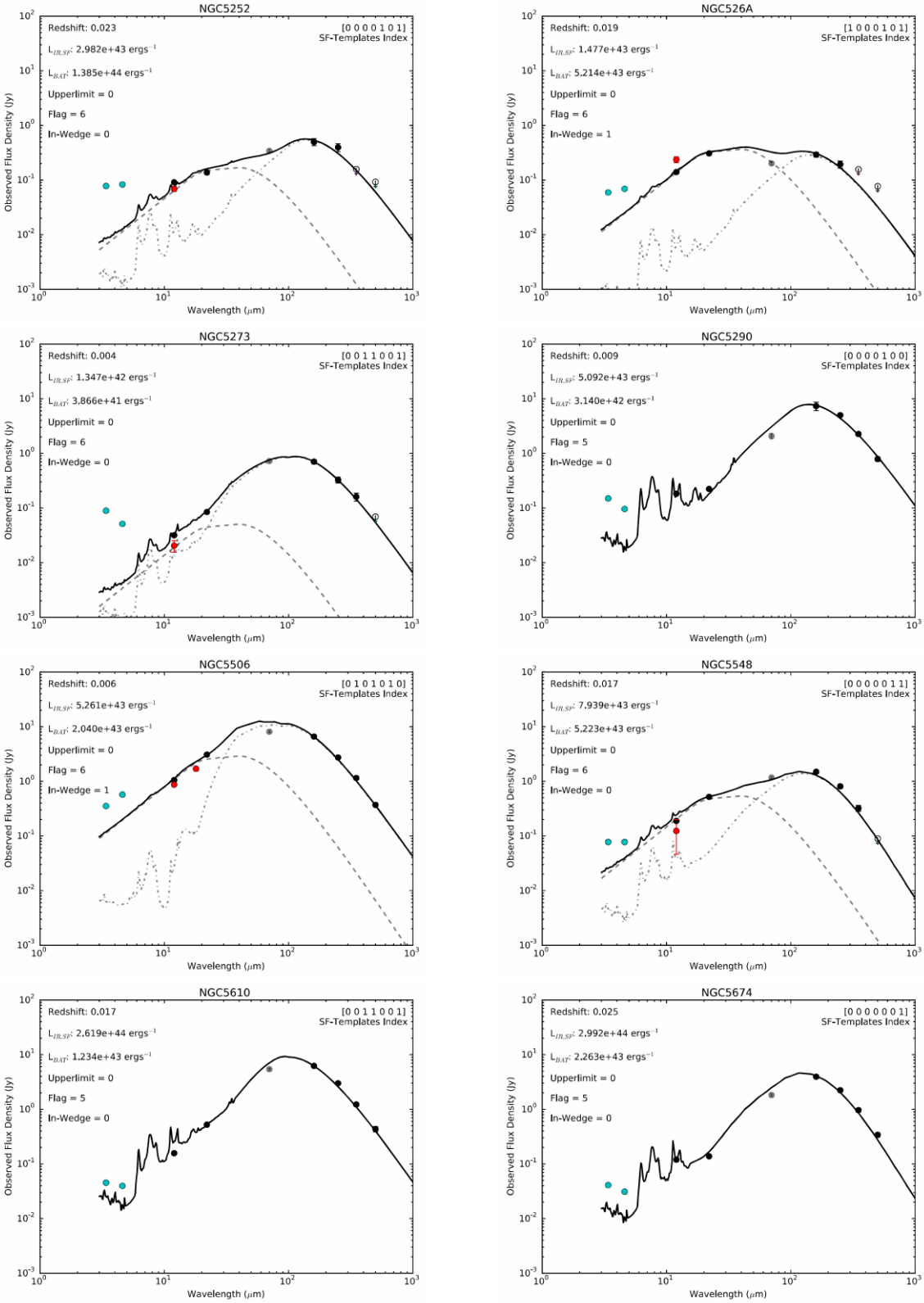

Figure A.34: Continued from Figure A.2, Best-fitted SED solutions for eight Swift-BAT sources (listed alphabetically).

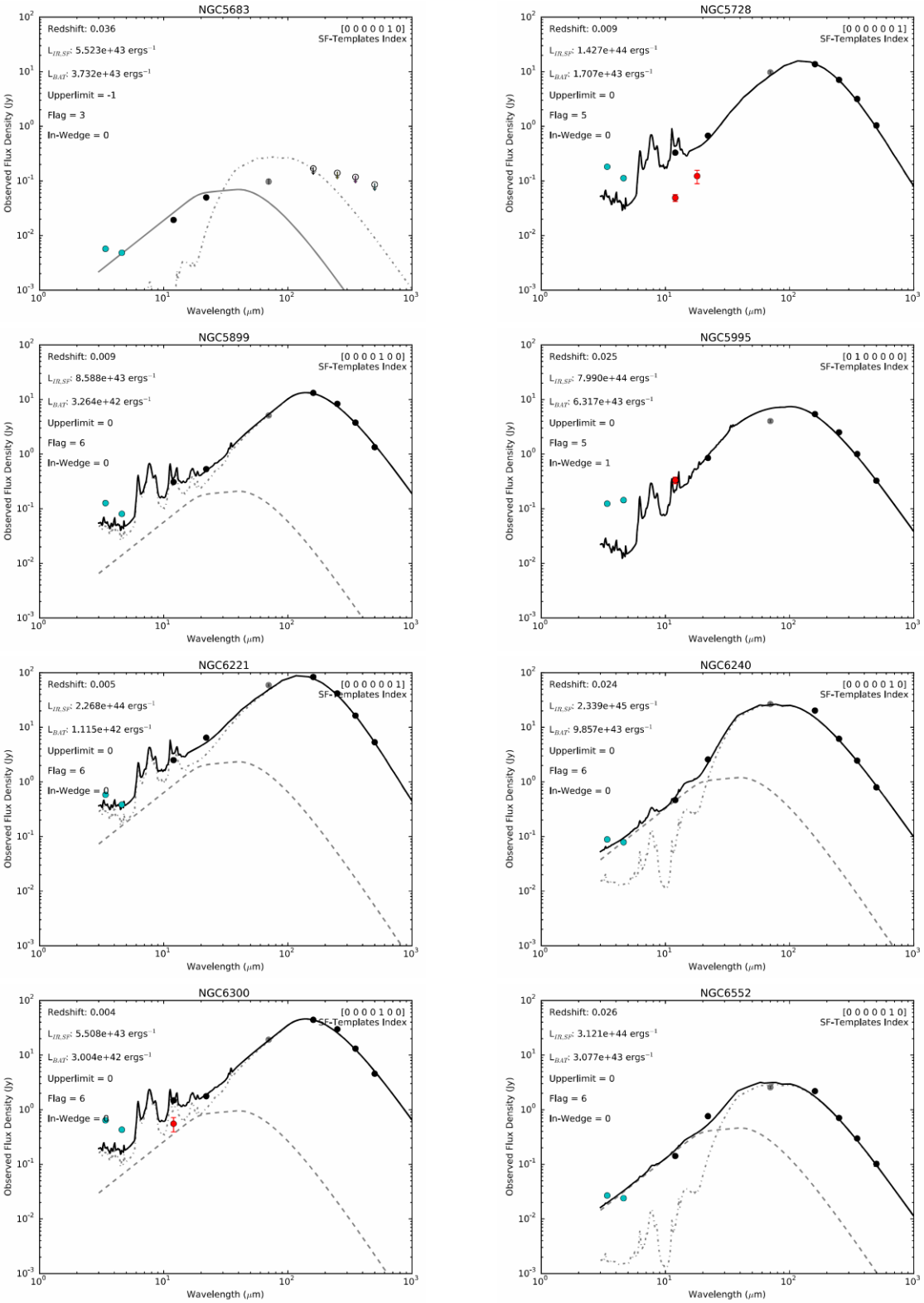

Figure A.35: Continued from Figure A.2, Best-fitted SED solutions for eight Swift-BAT sources (listed alphabetically).

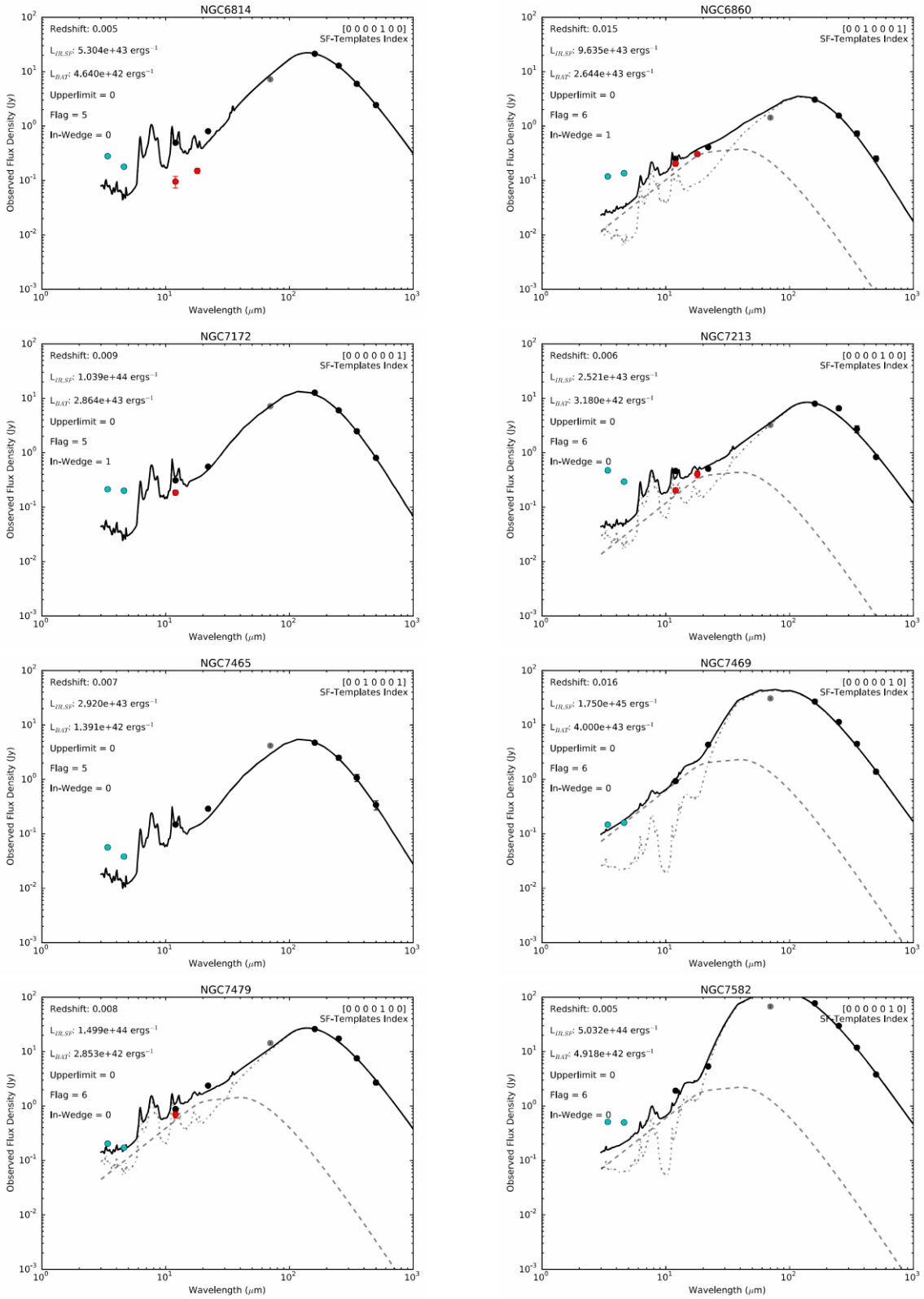

Figure A.36: Continued from Figure A.2, Best-fitted SED solutions for eight Swift-BAT sources (listed alphabetically).

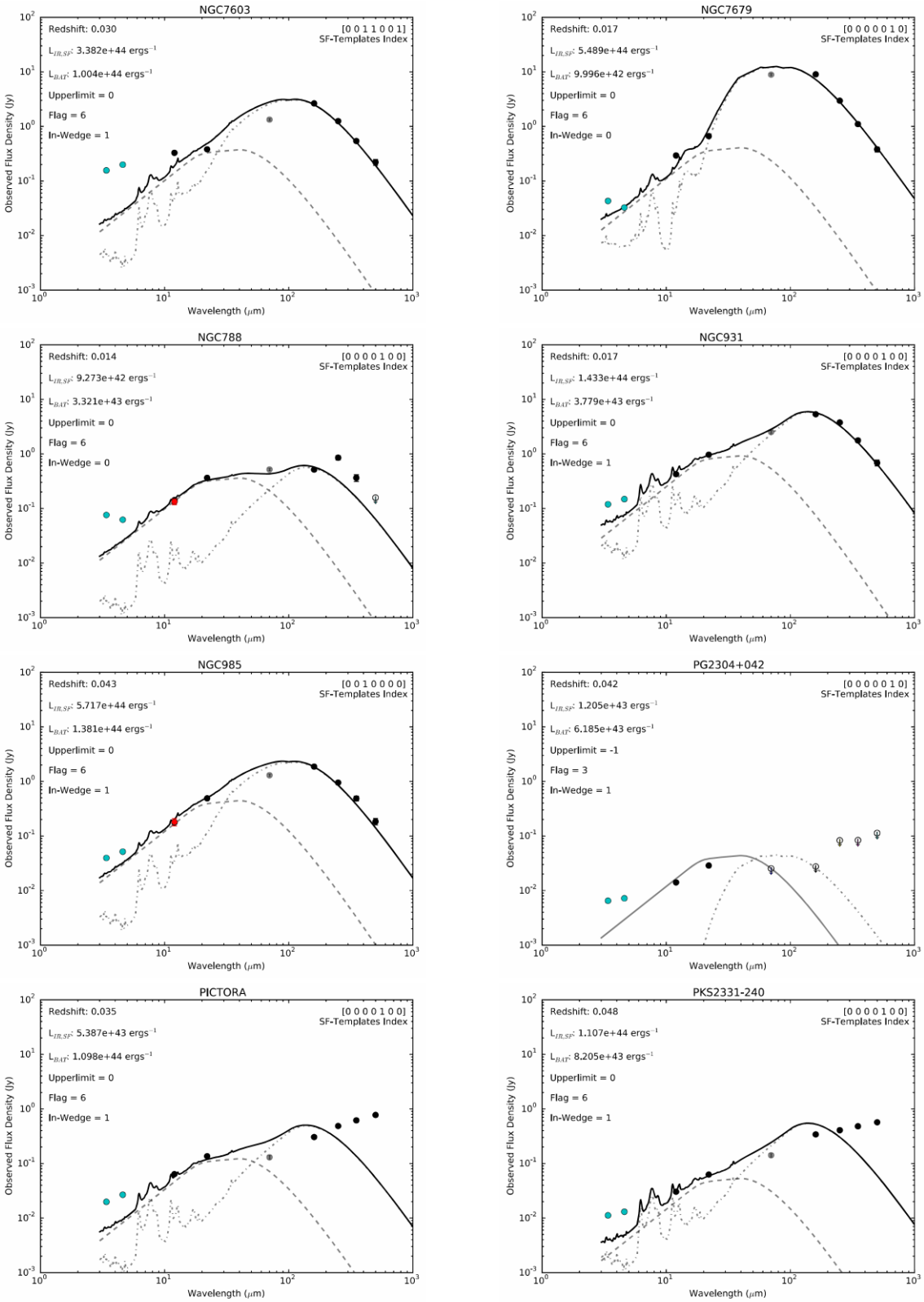

Figure A.37: Continued from Figure A.2, Best-fitted SED solutions for eight Swift-BAT sources (listed alphabetically).

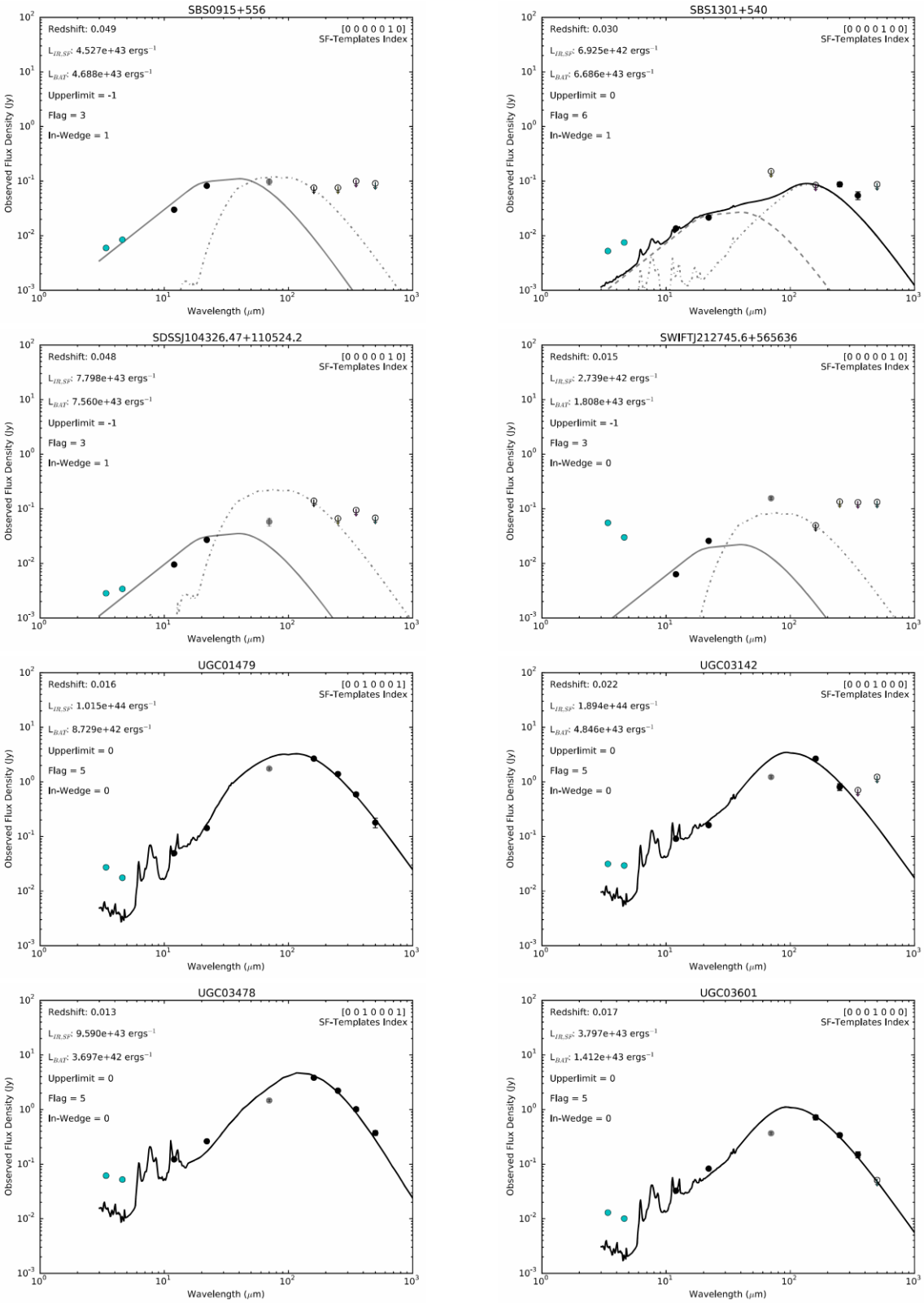

Figure A.38: Continued from Figure A.2, Best-fitted SED solutions for eight Swift-BAT sources (listed alphabetically).

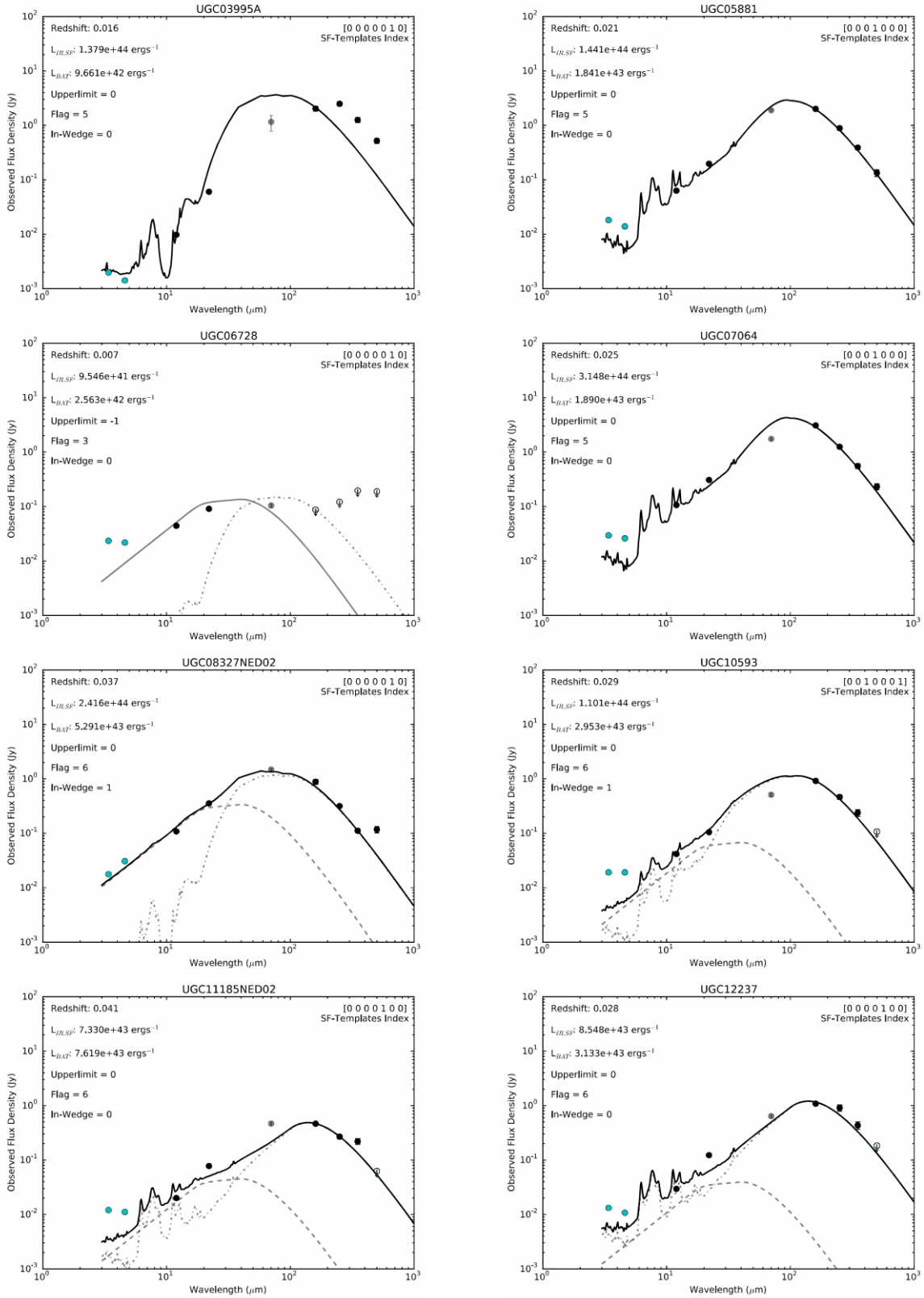

Figure A.39: Continued from Figure A.2, Best-fitted SED solutions for eight Swift-BAT sources (listed alphabetically).

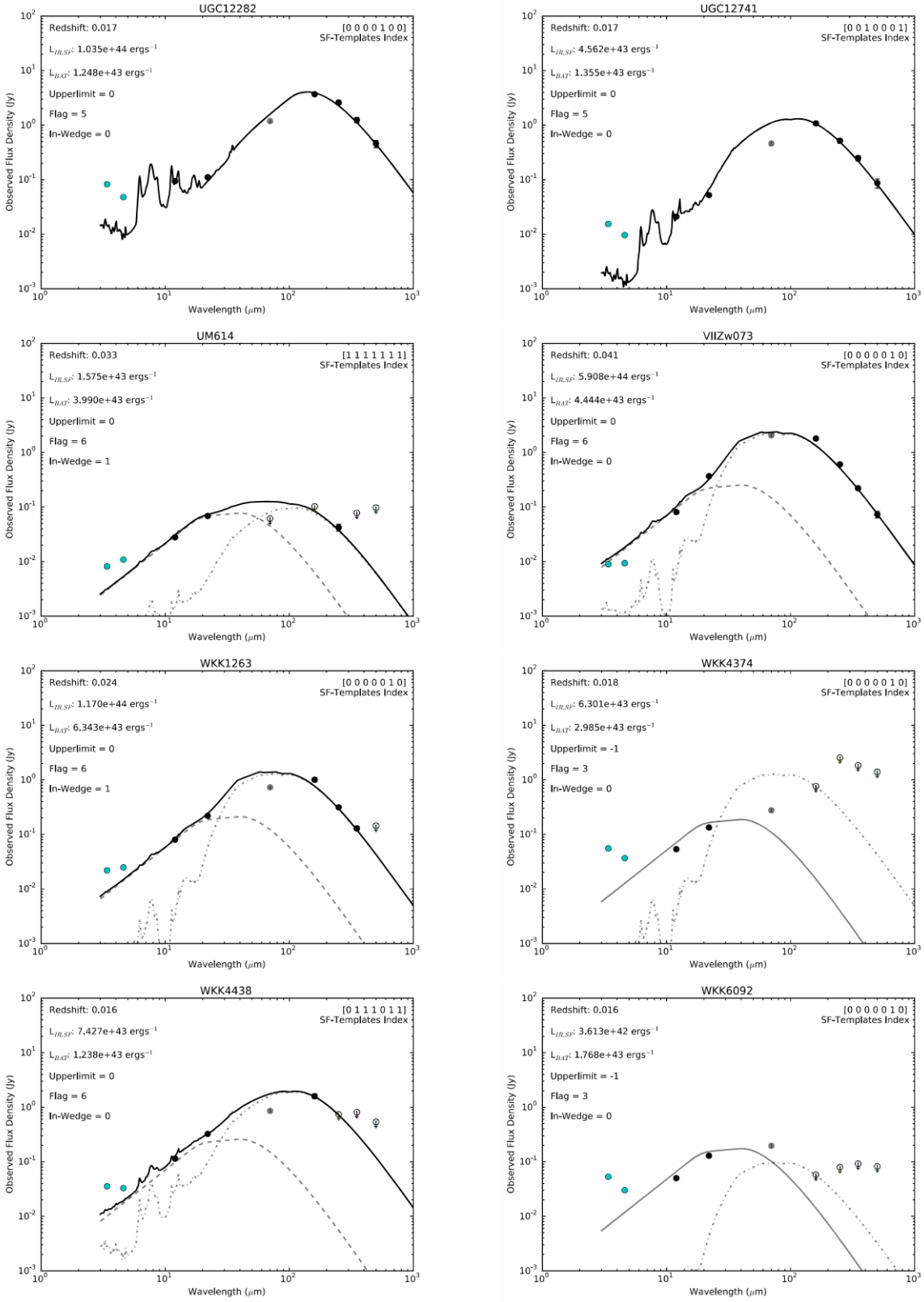

Figure A.40: Continued from Figure A.2, Best-fitted SED solutions for eight Swift-BAT sources (listed alphabetically).

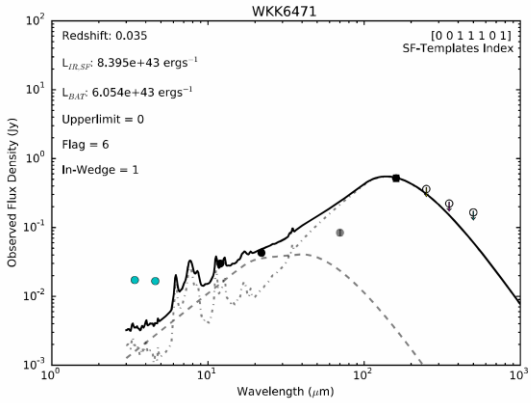

Figure A.41: Continued from Figure A.2, Best-fitted SED solution for one of the *Swift*-BAT sources (listed alphabetically).